Potential Electrocatalysts for Water Splitting Devices - A Journey Through the Opportunities and Challenges of Catalyst Classes

Robin Dürr

THESE DE DOCTORAT

NNT : 2022UPASF054

Potential Electrocatalysts for Water Splitting Devices – A Journey Through the Opportunities and Challenges of Catalyst Classes

Électrocatalyseurs potentiels pour l'électrolyse de l'eau – Challenges et opportunités de différentes familles de catalyseurs

Thèse de doctorat de l'université Paris-Saclay et de l'université d'Uppsala

École doctorale n°571 Sciences chimiques : Molécules, Matériaux, Instrumentation et Biosystèmes (2MIB)
Spécialité de doctorat : Chimie
Graduate School : Chimie. Référent : Faculté des sciences d'Orsay

Thèse préparée dans l'unité de recherche **NIMBE** (Université Paris-Saclay, CEA-Saclay, CNRS) et **Ångström Laboratory** (Uppsala University), sous la direction de **Bruno JOUSSELME**, Directeur de Recherche, et **Leif HAMMARSTRÖM**, Professeur (Uppsala University), le co-encadrement de **Vladimir ATANASOV**, Chercheur (University of Stuttgart), le co-encadrement d'**Antoni LLOBET**, Professeur (ICIQ Tarragona) et le co-encadrement de **Stéphanie NARBEY**, Ingénieur de recherche (Solaronix SA)

Thèse soutenue à Uppsala, le 12 Septembre 2022, par

Robin DÜRR

Composition du Jury

Ally AUKAULOO Professeur, Université Paris-Saclay	Président
Ulrike KRAMM Professeur, Technical University of Darmstadt	Rapporteur & Examinatrice
Christel LABERTY-ROBERT Professeur, Sorbonne-Université	Rapporteur & Examinatrice
Kevin SIVULA Professeur associé, École polytechnique fédérale de Lausanne	Examinateur
Bruno JOUSSELME Directeur de Recherche, CEA-Saclay	Directeur de thèse

université PARIS-SACLAY

ÉCOLE DOCTORALE
Sciences Chimiques : Molécules, Matériaux, Instrumentation et Biosystèmes (2MIB)

Titre : Électrocatalyseurs potentiels pour l'électrolyse de l'eau – Challenges et opportunités de différentes familles de catalyseurs

Mots clés : catalyseur HER, catalyseur OER, Electrolyseur

Résumé : Ce travail porte sur la synthèse et la caractérisation de différentes classes de catalyseurs et de leur intégration comme électrodes de travail pour une cellule d'électrolyse.

Les électrodes à base de complexes moléculaires de ruthénium fabriquées par sérigraphie (Article 2) présentent des activités et des stabilités élevées, à pH neutre, vis-à-vis de l'oxydation de l'eau. Les catalyseurs sous forme d'oligomères montrent des performances supérieures. La conductivité électronique de l'électrode est le facteur limitant de l'activité catalytique d'une telle anode moléculaire. De plus, le faible chargement en catalyseur impose des limitations supplémentaires pour atteindre des densités de courant élevées.

L'étude de matériaux catalytiques, composés d'un Métal de transition, d'Azote et de Carbone (Article 3) montre que celui contenant du cobalt a la plus grande activité pour la production d'hydrogène en milieu acide tout en montrant une certaine stabilité. Cette dernière s'explique par la présence de sites atomiques uniques, au détriment de la formation de nanoparticules, obtenus par une méthode de synthèse sans solvant. Ce procédé présente donc une stratégie intéressante pour la synthèse à grande échelle. Cependant, l'augmentation du nombre de site catalytiques dans le matériau reste une difficulté à surmonter.

Une méthode (Brevet I) de fabrication des assemblages membrane-électrode a aussi été mise en place. Elle permet le remplacement des membranes coûteuses couramment utilisées.

Deux structures de Molybdate de Nickel ont été synthétisées (Article 1) pour fabriquer, après électro-activation, des nanoparticules de γ-NiOOH actif envers la production d'oxygène en pH alcalin. L'élimination du molybdène conduit à une surface électrochimique élevée avec un grand nombre de sites de nickel exposé et explique l'origine de l'activité catalytique élevée. La présence de Molybdène sert donc ici d'agent structurant et porogène. L'étude par spectroscopie Raman montre que le dépôt en forme de bâtonnets (mis en évidence par microscopie électronique) fabriqué sur une mousse de Nickel comporte aussi le signal de la structure en feuille après l'éviction du molybdène. La présence de cette structure s'explique par une couche intermédiaire entre l'électrode en mousse et les bâtonnets visibles par microscopie électronique. Cependant, les résultats semblent indiquer une activité plus élevée pour la structure en bâtonnets. Un résultat essentiel de cette étude est que lors de la synthèse d'une structure en bâtonnets de Molybdate de Nickel sur une électrode, l'absence de la structure en feuille doit être vérifiée. Les différences fondamentales (Article 4) entre les nanostructures ont été caractérisées plus en détail à l'aide de diverses techniques : MEB, DRX et Spectroscopie Raman. Bien que les structures cristallines des deux nanostructures ne soient pas encore totalement résolues, les analyses montrent clairement qu'il s'agit de deux matériaux différents avec leurs propriétés. En effet la structure hydratée en feuille présente une activité supérieure à celle déshydratée pour la production d'hydrogène en milieu alcalin. Il est clair qu'une étape de réduction préliminaire est nécessaire pour accéder à l'activité catalytique exceptionnelle rapportée.

Parmi les différentes classes de catalyseurs étudiés, les catalyseurs à nanoparticules semblent être les plus prometteurs pour une intégration réussie dans une cellule d'électrolyse à grande échelle. L'utilisation généralisée de ce type de matériau pourra être envisagée une fois que la stabilité des catalyseurs et de la membrane échangeuse d'anions sera résolue.

université PARIS-SACLAY

ÉCOLE DOCTORALE
Sciences Chimiques : Molécules, Matériaux, Instrumentation et Biosystèmes (2MIB)

Title : Potential Electrocatalysts for Water Splitting Devices - A Journey Through the Opportunities and Challenges of Catalyst Classes

Keywords : HER Catalyst, OER catalyst, Electrolyzer

Abstract : In this thesis work, different classes of catalysts and their suitability for integration into an electrolyzer cell has been investigated.

Ruthenium-based molecular catalysts in Paper II have shown high activities and stabilities towards water oxidation in neutral pH. Especially the oligomeric catalysts exhibited a superior performance. The electrical conductivity of the electrode was discovered as limiting factor on the catalytic activity of such a molecular anode. In addition, the low loading of catalyst might impose limitations on reaching high current densities at reasonable potentials. Among the tested transition metal single atom catalysts synthesized by pyrolyzing transition metal doped ZIF-8 structures in Paper III, cobalt has shown the highest activity towards hydrogen evolution and a stable behaviour in acidic pH. The enhanced stability of single atomic sites compared to the corresponding nanoparticles was proposed. Only a low number of nanoparticles was suggested to have been formed during the solvent free synthesis. Hence, this process might present an interesting strategy for the large-scale synthesis of single atom hydrogen evolution catalysts. However, also for this class of catalyst, the low number of active sites seems to present a difficulty, which has to be overcome. With the novel method presented in Patent I to fabricate a membrane electrode assembly, the usage of commonly used expensive membranes could possibly be avoided. Both as-prepared nickel molybdate hydrate nanoparticle shapes – sheets and rods – have been proposed in Paper I to transform in an electrochemical activation step into γ-NiOOH as active phase for the oxygen evolution reaction in alkaline pH. With the removal of molybdenum a large electrochemical surface area with an increased number of exposed nickel sites was indicated to be the origin behind the high catalytic activity of the nanoparticles. Molybdenum was suggested to only act as structure and pore forming agent. Even for the sample on nickel foam with only rods initially visible by electron microscopy, Raman bands of the sheet structure was observed after selective molybdenum leaching and could be traced back to the intermediate layer between the foam electrode and the nanorods. However, preliminary results indicate a higher activity for the rod structure. The nanosheet layer between the rods and the foam might be an interesting observation for further works concerning nanorods on the electrode and the attribution of the catalytic activity. An essential outcome and proposal of Paper I is that when synthesizing especially a nickel molybdate rod structure on an electrode, the absence of the sheet structure should be verified, which could be done by either selective molybdenum leaching combined with Raman spectroscopy or XRD, or by investigating the volume between rods and the electrode with SEM. With Paper IV the fundamental differences between the nanostructures were characterized with various techniques, indicating strongly that those are two different materials. For the hydrogen evolution reaction in alkaline media, the hydrate sheet structure exhibited a higher activity compared to the anhydrate, but clearly a reduction step is necessary to access the outstanding catalytic activity reported. Among all the investigated catalysts of different classes, the nanoparticle catalysts seem to be the most promising for a successful integration in a large scale electrolyzer cell for widespread use, especially, once the stability of the catalysts and the anion exchange membrane is resolved.

This thesis is part of a cotutelle PhD, associated with a second version at Uppsala University, published with the ISBN 978-91-513-1547-8.

The differences between the two version are besides minor changes in wordings that the one presented here includes the abstracts of this thesis in French and English as well as a summary in French and a cover page following the requirements of the University Paris-Saclay, whereas the version at Uppsala University includes a popular science chapter in Swedish and German instead to fulfill the requirements of Uppsala University.

ACKNOWLEDGMENTS

First of all many thanks to **Prof. Kramm**, **Prof. Laberty-Robert**, **Prof. Aukauloo** and **Prof. Sivula** for being in the committee of my PhD Defense.

Now it is time to thank all the people who supported and shaped me during this journey. Apologies already here for some I might have forgotten to mention.

At first, I would like to thank **Leif Hammarström** from Uppsala University **Bruno Jousselme** from CEA Paris Saclay for supervising the entire work from the very beginning. Thank you for all your support, feedback and help during the last nearly four years.

Directly following that I want to thank the whole eSCALED Project, the managers **Laia Francesch**, **Laurent Billon** and **Antoine Bousquet** for organizing this whole project and always be supportive and caring. This whole PhD was amazing and you made all this possible! I would like to thank all eSCALED students, with whom I shared some time in the lab and the workshops namely **Ludo**, **Domenico**, **Silvia**, **Diogo**, **Saeed**, **Afridi**, **Karell**, **Andrew B.**, **Andrew H.**, **Van**, **Olivera**, **Bruno** and **Ignazi**. It was a wild ride and even the time was always too limited, it was always fun!

Chronologically, I would like to thank all the people of the LICSEN group at CEA Paris-Saclay, especially **Frédéric Oswald**, **Renaud Cornut** for co-supervising and **Sarah**, **Thomas**, **Florian**, **Julie** and **Fatima** for welcoming me to this new journey, being always there and most of all helping me with all the French administration (special thanks to **Sarah**!). In addition, thank you **Ndrina**, **Lina** and **Yuemin**. Without you my short return to in Paris would not have been as beautiful as it was! For the amazing time outside of the lab also a gigantic thank you to **Andreas**, **Bassem** and **Marta**! The evenings together are and will be missed!

I also would like to say thank you to **Vladimir Atanasov**, **Johannes Bender** and **Jens Brombacher** for your support during my

secondment at the University of Stuttgart. In addition, **Verena**, **Eric**, **Lukas**, **Jonas** for the wonderful time in Stuttgart Süd, **Manu**, **Philipp** and **Alina** and of course **Miri**, **Fabi**, **Payer**, **Anne** and the whole **Stuttgarter Turner Crew**, which is too large to be mentioned here, for everything since the very beginning.

Furthermore, a very big thank you to **Toni Llobet** and his group at ICIQ Tarragona, who made me feel very welcome. Thank you, **Marcos**, also for the supervision, **Marta**, **Nataliia**, **Primavera**, **Jan** and **Florian**. I am so happy to get to know you and really hope we will see each other at one or the other conference or at least at a reunion at Quattros (or Cau)! The thank you clearly also applies to **Ester** and **Alexandrina**! The time in Tarragona has a special spot in my memories and I cannot thank you enough for everything!

The next very big thank you is directed to **Tomas Edvinsson** and **Haining Tian** from Uppsala University, who joined the supervision during my PhD. Thank you, Tomas and Haining, for all the feedback, input and motivation! Additional thank you Tomas for having me in your group and all the help! I am so grateful for your mentoring and trust. Also thank you **Ilknur**, **Jakob** and **Pierfrancesco** for your help and advices. The next big thank you is to **Kerstin Ekelöf** and **Nhils Forslund** at UU Innovation, for supporting me so much with the patent! Without you this would not have been possible! Further, also a big thank you to you, **Nicole**, who made even the dark Swedish winter more bearable. This also accounts to **Sara**, **Brian**, and the all **climbing people**, who really made me have a good start in Uppsala. In addition, thank you, **Starla**, for all your advices and comments, especially in the last year of my PhD!

Also, a huge thank you to **Stephanie Narbey** and **David Martineau**, as well as **Toby Meyer** and **Andreas Meyer**, who supported and guided me during my project at SOLARONIX. Thank you, **Sarah**, for this amazing time around Lac Léman and in whole Switzerland.

I really had an awesome last year in Uppsala and it is a pity it took us so long to get to know each other in person! Thank you, **Martin**, **Luca**, **Belinda**, **Astrid**, **Fiona**, **Rima**, **Sigrid**, **Mariia** and **Andrea**! I am really glad to have had you around. Thank you for all the help, the

explanations of *basic* stuff necessary to follow the subgroup meetings as Marcus theory, Marcus Parabolas and Ultrafast Transient Absorption Spectroscopy. In addition, thank you for listening to and acknowledging my good ideas as well as aaaaaaaall my complains! Especially to **Martin** a special thanks for all the discussions and your help with the Popular Science part of this thesis. Needless to say, a big thank you also applies to you, **Nina**, **Daniel**, **Kate, Holly**, **Sina**, **Wanja**, **Alenka**, **Kelly**, **Moritz**, **Claudia**, **Anđela**, **Nora**, and **Salauat**. Even though the overlapping time was unfortunately too short, thank you **Ashleigh, Victor, Minli** and **Dylan** and all members of **Fyskem**, **SMC**, **MolBio** and **CAP** for this amazing time inside and outside of Ångström! In addition, thank you **Martina**, **Lina**, **Eva**, **Maria** and all others in HR and the administration for all the support and help during my PhD!

Of course, I also want to thank my whole family! **Mama** und **Papa**, Ich danke euch für all eure Unterstrützung, und dass ihr an mich geglaubt habt. Ohne euch wäre ich heute nicht hier. Vielen Dank, dass ihr mir immer zugehört habt, auch wenn ihr wahrscheinlich nicht ganz nachvollziehen konntet, um was es eigentlich ging. Dafür danke ich dir, **Fabio**, dass du das kompensieren konntest und für die schöne Zeit bei jeder Rückkehr. Natürlich gilt das auch für euch, **Benny** und **Lena** mit **Ella** und **Fine**! Vielen Dank für eure Unterstützung und dass ihr mich zum stolzesten Onkel/Patenonkel/Dronkel gemacht habt! Vielen Dank für all die Freude, die ihr in mein Leben bringt und dass ihr mein Stresspegel mit jedem Treffen und Anruf zurücksetzt! Ein weiteres riesiges Dankeschön geht natürlich auch an meine **restliche Familie**!

Last but not least I would like to thank **Alizée** for her music, being one of the rare constants during my PhD.

LIST OF PUBLICATIONS

This thesis is based on the following papers, which are referred to in the text by their Roman numerals.

I. Dürr, R. N., Maltoni, P., Tian, H., Jousselme, B., Hammarström, L., Edvinsson, T. (2021) From NiMoO4 to γ-NiOOH: Detecting the Active Catalyst Phase by Time Resolved *in Situ* and *Operando* Raman Spectroscopy. *ACS Nano*, 15(8):13504–13515
Correction: Same authors (2021), *ACS Nano*, 15(12):20693

II. Dürr, R. N.,[‡] Chasvised, S.,[‡] Gil-Sepulcre, M., Howe, A., Hoque, M. A., N'Guyen, V., Sadeghi, S., Reynaud, S., Cugnet, C., Authier, L., Gimbert-Suriñach, C., Bousquet, A., Llobet, A., Billon, L. (2021) Robust and Efficient Screen-Printed Molecular Anodes with Anchored Water Oxidation Catalysts. *ACS Applied Energy Materials*, 4(10):10534–10541

III. Dürr, R. N., Leroy, J., Oswald, F., Verhaeghe, B., Jousselme, B. Efficient, stable and solvent free synthesized single atom catalysts: Carbonized transition metal doped ZIF-8 for the hydrogen evolution reaction. *Submitted*.

IV. Dürr, R. N., Maltoni, P., Feng, S., Ghorai, S., Ström, P., Tai, C.-W., Edvinsson, T. Clearing Up Discrepancies in 2D and 3D Nickel Molybdate Hydrate Structures. *In manuscript*.

Reprints were made with permission from the respective publisher. Paper I and its correction are licensed under CC BY 4.0.

[‡] These authors contributed equally to this work.

Further, this thesis also includes a patent, which is referred to in the text by its Roman numeral.

I. Dürr, R. N. (2022) PROCESS FOR PREPARING A MEMBRANE ELECTRODE ASSEMBLY. WO/2022/129367

CONTRIBUTION TO PAPERS AND PATENT

Papers:

I. Synthesis of the material, designing, conducting and analysing all experiments, writing the manuscript in collaboration with the co-authors.

II. Anchoring immobilized catalyst on printed electrodes and electrochemically characterized the molecular anodes. Writing the manuscript in close collaboration with Dr. Marcos Gil-Sepulcre. Contributing to the review process.

III. Designing the study. Synthesis of the materials, electrochemical, SEM and EDX investigation. Analysis of all data and writing of the manuscript.

IV. Designing and leading the study. Synthesis of the materials, conducting all spectroscopic measurements (XPS, Raman Spectroscopy, ATR-FTIR), SEM, EDX, analysed TGA, contributed to the ToF-ERDA, RBS, TEM and XRD measurement and analysis, writing of the manuscript.

Patent:

I. Invented the process and filed with the support of UU Innovation and patent attorneys the Swedish and European PCT application.

ABBREVIATIONS

^{1}H-NMR	Proton Nuclear Magnetic Resonance
AEC	Alkaline Electrolyzer Cell
AEM	Anion Exchange Membrane
AEMEC	Anion Exchange Membrane Electrolyzer Cell
bda	[2,2′-bipyridine]-6,6′-dicarboxylate
BE	Binding Energy
bpy	4,4′-bipyridine
c_0	Speed of Light (299 792 458 m s^{-1})
CA	Chronoamperometry
CCM	Catalyst Coated Membrane
CCS	Catalyst Coated Substrate
C_{dl}	Double Layer Capacitance
CNT	See MWCNT
CP	Chronopotentiometry
CV	Cyclic Voltammetry / Cyclic Voltammogram
DFT	Density-Functional Theory
EC	Electrolyzer Cell
ECSA	Electrochemical Surface Area
EDX	Energy Dispersive X-ray Spectroscopy
EIS	Electrochemical Impedance Spectroscopy

ESCA	Electron Spectroscopy for Chemical Analysis
F	Faraday Constant (96 485 C mol^{-1})
FEG	Field Emission Gun
FOWA	Foot of the Wave Analysis
GDL	Gas Diffusion Layer (carbon-based)
h	Planck Constant (6.626 10^{-34} J s)
HEC	Hydrogen Evolution Catalyst
HER	Hydrogen Evolution Reaction
I2M	Interaction of Two Metal-Oxo Units
IBA	Ion Beam Analysis
ICP-OES	Inductively Coupled Plasma – Optical Emission Spectrometry
IEMEC	Ion Exchange Membrane Electrolyzer Cell
*i*R	Solution Resistance
KE	Kinetic Energy
LDH	Layered Double Hydroxides
MEA	Membrane Electrode Assembly
MOF	Metal-Organic Framework
MWCNT	Multi-Walled Carbon Nanotube
OEC	Oxygen Evolution Catalyst
OER	Oxygen Evolution Reaction
PCET	Proton-Coupled Electron Transfer

PE	Primary Electrons or Printed Electrode
PEC	Photoelectrochemical Cell
PEM	Proton Exchange Membrane
PEMEC	Proton Exchange Membrane Electrolyzer Cell
pic	4-picoline
PV	Photovoltaic Cell
py	Pyridine
pyp	4-(pyrene-1-yl)pyridine
R	Gas Constant (8.314 J K^{-1} mol^{-1})
RBS	Rutherford Backscattering Spectrometry
RHE	Reversible Hydrogen Electrode
Ru-MWOC	Ruthenium-based Molecular Water Oxidation Catalyst
SAC	Single Atom Catalyst
SE	Secondary Electrons
SEM	Scanning Electron Microscopy
SHE	Standard Hydrogen Electrode
tda	[2,2′:6′,2′′-terpyridine]-6,6′′dicarboxylate
TEM	Transmission Electron Microscopy
TGA	Thermogravimetric Analysis
ToF-ERDA	Time of Flight Elastic Recoil Detection Analysis
TOF_{max}	Maximum Turnover Frequency

WNA	Water Nucleophilic Attack
XPS	X-ray Photoelectron Spectroscopy
XRD	X-ray Diffraction
ZFC-FC	Zero Field Cooled and Field Cooled Measurements
ZIF	Zeolitic-Imidazolate Framework

CONTENTS

1 INTRODUCTION

With a rising global surface temperature and increasing number of weather-, climate- and water-related disasters in the past decades, the consequences of climate change are clearly perceivable.[1,2] In order to counteract global warming – or at least try to minimize the detrimental effects as best as possible – net additions of greenhouse gases to the atmosphere have to be reduced urgently. One of these contributions is the usage of fossil fuels, which generates the greenhouse gas carbon dioxide. In the Paris Agreement from 2015, 196 parties agreed on establishing strategies to limit the global warming by the end of this century to 1.5 °C compared to the pre-industrial average surface temperature. To realize this, the European Union (EU) aims to reduce greenhouse gas emissions and to be climate neutral by 2050. Among others, implementing renewable energies on a large scale, which should produce more than 80 % of generated electricity in 2050, is intended.[3] Furthermore, energy intensive sectors, as transport and industry, are planned to transit to alternative energy carriers like sustainable produced hydrogen, which in use is carbon neutral.

Sadly, as projected by the Intergovernmental Panel on Climate Change (IPCC) report in 2022, it is highly probable that we are globally not on track and are heading towards more extreme and more frequent weather phenomena as droughts, floods, storms, and rising sea levels.[4] As a result, not only direct tangible consequences on humankind such as hunger, poverty and mass migration could be expected, but also the loss of biodiversity and destruction of ecosystems, which exact long lasting effects are unpredictable but unambiguously catastrophic.[4,5] Thus, it is more than urgent to rapidly establish the widespread use of new, environmentally friendly technologies, to transit from a fossil fuel-based to a circular and sustainable energy economy.

1.1 ARTIFICIAL PHOTOSYNTHESIS AND ELECTROLYZER CELLS

A sustainable energy cycle is already common in nature. With photosynthesis, trees and green plants convert water and carbon dioxide with energy provided by solar light into a sugar and oxygen as by-product. When required, in a simplified description, the stored

energy can be accessed in the cellular respiration process by converting the sugar and oxygen back into water, carbon dioxide with release of the stored energy.

With an incident power of 1000 W m−2 for AM 1.5, the sun already provides a huge amount of energy. To put this number in perspective: The incident solar power equals 120 000 TW to the earth's surface.[6] In less than 1 hour and 20 minutes the sun irradiates the earth with more energy than what was globally consumed in primary energy in the year 2020.[7] Besides capturing all this energy, a clear problem of solar as renewable energy source is its intermittency. Hence, taking the approach of photosynthesis as inspiration, the energy harvested by renewable energy sources such as solar, could be ideally stored in chemical fuels, in this case termed *solar fuels*. Those solar fuels could be used to overcome the intermittency and satisfy the energy demand in times in which the renewable energies do not provide enough. The generation and use of solar fuels would thus enable a circular energy economy. Following this guideline, the most straight forward reaction for storing energy would be to split water in molecular hydrogen and oxygen. This process is an uphill reaction, which requires from thermodynamics 1.23 eV, illustrated in Figure 1.1. Or expressed in a different way: 1.23 eV of renewable energy could be stored in each

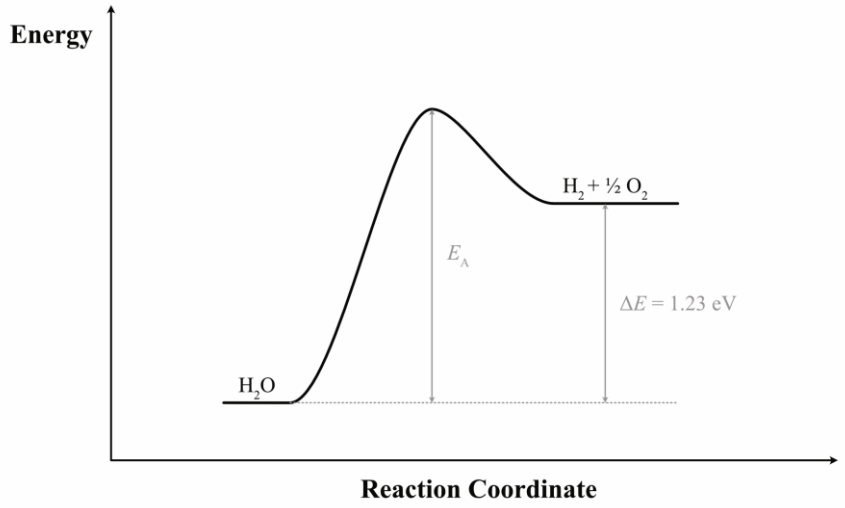

Figure 1.1: Energy diagram for the conversion of water into hydrogen and oxygen.

water molecule, with one electron reducing each hydrogen. In terms of Gibbs free energy this amount of energy can be calculated as

$$\Delta G^0 = -nF\Delta E^0 = 237 \text{ kJ mol}^{-1} \quad (1.1)$$

Where n equals the number of transferred electrons (here 2), F is Faraday's constant (96485.33 C mol^{-1}) and ΔE^0 is the potential difference between the reduction and the oxidation reaction (here −1.23 V).

Due to kinetic barriers, shown in Figure 1.1 above as activation energy EA, the energy required to drive this reaction at a rate of practical interest is >1.23 eV. The purpose of catalysts is to minimize this activation energy and will be discussed later. In the presented reaction, oxygen evolves at the anode and hydrogen at the cathode. Those two half reactions will be described in more depth in the following chapters. However, the setup of those electrodes and the photovoltaic cell can be quite different. In one embodiment, the photoelectrochemical cell (PEC), the catalyst at which one reaction takes place, is the photoabsorber itself or is in direct contact with the photoabsorber. Those systems can be constructed as particle-based or panel-based PECs. A possible architecture of the latter is illustrated in Figure 1.2 **(A)**, similar to the one reported by Khaselev and Turner already in 1998.[8] Despite the high efficiencies reported for panel-based PECs,[8,9] particle-based PECs have potential to produce hydrogen at a lower cost.[10] The latter system has already been demonstrated by the Domen group in a safe and large scale implementation in Tokyo with a 100 m^2 particle-based PEC system.[10,11] A major drawback of PECs in general is besides the lower conversion efficiency compared to the fully decoupled system discussed in the following, the limited stability of the photoabsorber in solution.[8,10] Since for panel-based PECs the charge separation already happens at the pn-junctions, there is no obvious need to place those into the electrolyte in the first place.[12] To overcome this instability issue, photoabsorption and electrolysis can be fully decoupled by connecting a photovoltaic cell (PV) to a separate electrolyzer cell (EC). This leads to an increased solar-to-hydrogen conversion efficiency as well as a larger variety of PV cells applicable in this configuration.[10] The EC powered by an external PV cell can exhibit different architectures, presented in the following.

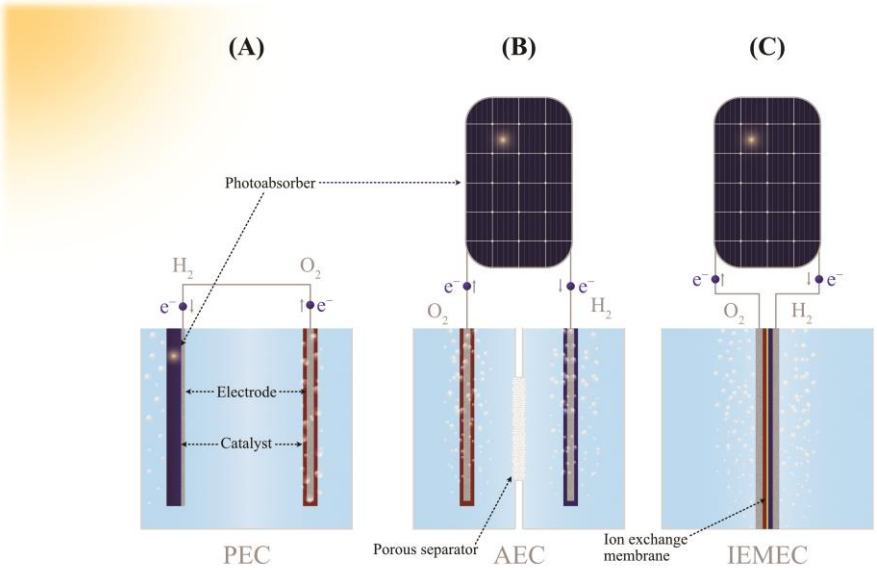

*Figure 1.2: Schematic illustration of three different setups of electrolyzer cells with **(A)** a photoelectrochemical cell (PEC), **(B)** alkaline electrolyzer cell (AEC), and **(C)** ion exchange membrane electrolyzer cell (IEMEC), which represents the setup of a proton exchange membrane electrolyzer cell (PEMEC) and an anion exchange membrane electrolyzer cell (AEMEC). Photoabsorber are illustrated in dark blue/violet, electrodes as grey, catalyst on the anode in red and catalyst on the cathode in blue, the porous separator as porous white structure in (B) and the ion exchange membrane in yellow in (C). The illustration of AEC and IEMEC represents a decoupled PV cell.*

The alkaline electrolyzer cell (AEC) in Figure 1.2 **(B)** is displayed as two electrodes in alkaline media, divided by a porous separator. The alkaline environment allows the employment of earth abundant non-noble metals as for example nickel, cobalt, molybdenum and iron as electrodes and catalysts. This technology is already mature, however, due to the porous separator, highly basic conditions are needed to increase the ion conductivity and thus reduce the solution resistance between anode (electrode at which the oxidation and hence formation of oxygen takes place) and cathode (electrode at which the reduction and hence formation of hydrogen takes place). Due to the porous separator gas crossover cannot be fully avoided, leading to a decreased gas purity. Additionally, the current density under operation is only in the range up to 0.5 A cm^{-2}.[13–16]

In contrast, the proton exchange membrane electrolyzer cell (PEMEC) operates at higher current densities up to 2 A cm^{-2}.[16] In this setup the anode and cathode are in direct contact with a polymer membrane as illustrated in Figure 1.2 **(C)**. Usually a Nafion® membrane is employed for this purpose, a sulfonated fluoropolymer, which shuttles protons from the anodic to the cathodic site of the cell. Since both electrodes are in direct contact with the membrane in between, this configuration is commonly referred to as *zero-gap* configuration. Such a configuration reduces the resistance between the anode and cathode substantially and is one of the reasons the PEMEC is operated at such high current density.[17] The solid polymer membrane also prevents gas crossover and thus provides a high gas purity. Unfortunately, due to the acidity of this electrolyzer cell setup, the materials applicable are limited. The catalysts used are commonly noble metal-based with Pt for the hydrogen evolution reaction (HER) and IrO_x and RuO_x for the oxygen evolution reaction (OER). A rising effort is made to substitute those catalysts, but up to now, especially for OER in acidic media, no active and stable materials are known.[18] Actually, neither RuO_x nor IrO_x are stable in these conditions, but this will be not further discussed here.[19,20] Furthermore, since carbon-based electrodes are prone to oxidize under high applied potentials, porous titanium is used as electrode for the anode. The scarcity of noble metals, the high-costs of the membrane as well as of the titanium electrode materials and the corresponding higher-cost of produced hydrogen are reasons hampering the widespread use of this technology.[15–17,20,21]

An emerging setup is the anion exchange membrane electrolyzer cell (AEMEC), which combines the benefits of low cost and abundant raw materials of the AEC with the decreased resistance and higher gas purity of PEMEC by substituting the proton exchange membrane with an anion exchange membrane (AEM). Such membranes are responsible for shuttling hydroxide ions from the cathode to the anode during operation. Unfortunately, the stability of polymeric membranes in basic conditions as well as the reduced hydroxide ion mobility compared the proton mobility are still challenges which have to be overcome. However, promising results are reported.[17,22]

Beside the listed variations of electrolyzer cells, there are several other examples as solid oxide electrolyzer cell or membraneless electrolyzer

cells,[15,16,21,23] which are not further discussed here. However, recently Hodges and Hoang of the group of Swiegers reported a capillary-fed electrolysis cell, which exhibited due to an improved cell structure and decreased resistances an impressive energy efficiency of 98 % at 0.5 A cm^{-2}, which I believe will shape the development of new prototypes of electrochemical cells in the next years.[24]

1.2 WATER SPLITTING

The above described chemical conversion of water into hydrogen and oxygen is called *water splitting*. The overall redox reaction is divided into two half-cell reactions. The oxygen evolution reaction (OER) under acidic conditions can be described by

$$2\ H_2O \rightleftharpoons 4\ H^+ + 4\ e^- + O_2 \tag{1.2}$$

and the hydrogen evolution reaction (HER)

$$2\ H^+ + 2\ e^- \rightleftharpoons H_2 \tag{1.3}$$

As obvious from the two equations, both reactions (1.2) and (1.3) are influenced by the concentration of protons. This influence on the thermodynamic redox potential, E_{redox}, can be quantified following Nernst equation (1.4), as an example for the HER (1.3) at two different values pH_1 and pH_2, assuming the same hydrogen partial pressure at both pH values:

From

$$E_{\mathrm{redox}} = E^{0\prime} + \frac{RT}{z_e F}\ln\left(\frac{[\mathrm{Ox}]}{[\mathrm{Red}]}\right) \tag{1.4}$$

$$= 0\ \mathrm{V} + \frac{RT}{2F}\ln\left(\frac{[\mathrm{H}^+]^2}{P_{\mathrm{H_2}}}\right)$$

Follows

$$\Delta E = E_{\mathrm{redox}}^{\mathrm{pH_1}} - E_{\mathrm{redox}}^{\mathrm{pH_2}} = \frac{RT}{2F} \times 2.303 \times 2(-\mathrm{pH_1} + \mathrm{pH_2})$$

$$= -0.059\ \mathrm{V} \times \Delta\mathrm{pH} \qquad (1.5)$$

With $E^{0\prime}$ being the formal standard potential of the redox reaction, R the gas constant (8.314 J K^{-1} mol^{-1}), T the temperature (here 298.15 K), z_e the number of transferred electrons in the reaction (here 2), F again Faraday constant (96 485 C mol^{-1}), and $[\mathrm{Ox}]$ and $[\mathrm{Red}]$ the concentration of the oxidized and reduced species, respectively. As derived, at room temperature the thermodynamic potential shifts with −59 mV per increasing pH unit. This shift can similarly be derived for the OER and is graphically illustrated in the Pourbaix diagram for water in Figure 1.3, which presents the thermodynamically stable phases for an applied potential at a certain pH. The potentials are reported *versus* the standard hydrogen electrode (SHE), which represents the redox potential of a platinum electrode in an ideal solution with 1 M H^+ and hydrogen gas at 1 atm pressure.

As derived and graphically illustrated in the Pourbaix diagram in Figure 1.3, the thermodynamic potential for HER *versus* SHE shifts for a change in pH. Hence, for a better comparison of electrochemical data acquired at different pH values, the applied potentials are often not

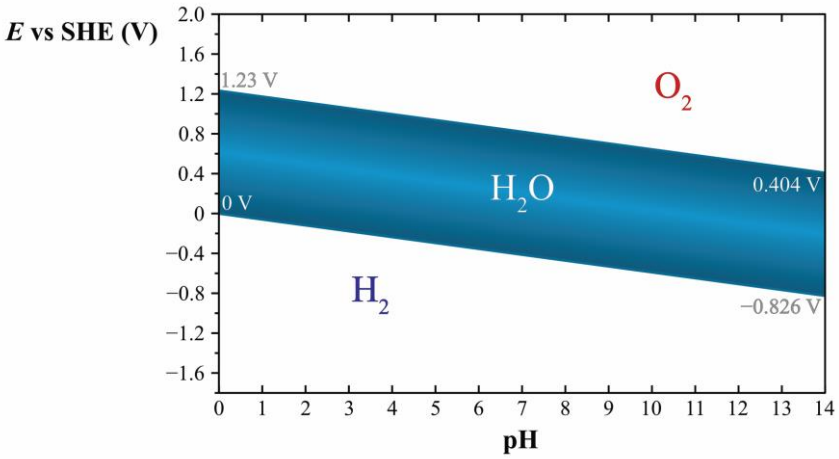

Figure 1.3: Pourbaix diagram of water. In the blue band water is thermodynamically stable. In the white region above the blue band oxygen is more stable, in the white region below hydrogen. Hence, for applied potentials in those regions, oxygen evolution or hydrogen evolution can happen thermodynamically.

reported *versus* SHE, but *versus* the reversible hydrogen electrode (RHE). This electrode represents the redox potential for HER at the pH value used. The value of RHE at a given pH can therefore be seen as the potential at the lower border of the blue band in Figure 1.3. With a change in pH, not only the thermodynamic potential of the two half-cell reactions changes, but also their reagents, as described in the next two chapters.

1.2.1 Oxygen Evolution

The oxygen evolution reaction is a crucial reaction in many electrochemical processes including water splitting. Not only does this reaction provide electrons to the cathode, but also protons, which can participate in several different highly desirable electrochemical reduction processes. Besides being reduced to molecular hydrogen, as shown in the next chapter, protons can also be included in the reduction of carbon dioxide into carbon monoxide or a variety of small organic molecules, or in the reduction of molecular nitrogen to ammonia.[25] All mentioned reduction processes are anticipated to play a game changing role in the coming decades four our society.[25]

Focussing on water splitting, the oxygen evolution reaction at the anode is commonly displayed as the bottleneck.[26] The oxidation of water requires the removal of four protons, four electrons and the formation of an O−O bond, which is overall an energetic unfavourable and mechanistic challenging process.[27,28] As indicated in Chapter **Error! Reference source not found.** above, depending on the pH v alue, the reaction equation can be expressed differently. In acidic conditions as:

$$2\ H_2O \rightleftharpoons 4\ H^+ + 4\ e^- + O_2 \qquad (1.2)$$

Whereas in alkaline conditions as :

$$4\ OH^- \rightleftharpoons 2\ H_2O + 4\ e^- + O_2 \qquad (1.6)$$

With the principle of Le Chatelier it can be understood that the oxygen evolution reaction is more favourable in alkaline media than in acidic media, which in combination with the reported instability of catalysts

for the OER in acidic conditions highlights the benefits of alkaline conditions for this step. In addition, in alkaline media the hydroxide ion is suggested to participate in the adsorption and O–O bond formation, shown below in Figure 1.4 **(A)** and **(C)**, whereas in acidic media water molecules are used, requiring additional energy demanding water dissociation steps.[29]

The overall reaction is generally divided in four subsequent steps. For the sake of simplicity, in the following one possible reaction mechanism for OER is displayed with water as the reagent.[30,31] In this mechanism, each step involves a proton-coupled electron transfer (PCET). In short, in Figure 1.4 **(A)** a water molecule is adsorbed on the surface. In the water activation step in **(B)** an oxide is formed, which participates in an O–O bond formation step with a nearby water molecule in **(C)**, creating a superoxide intermediate. This O–O bond

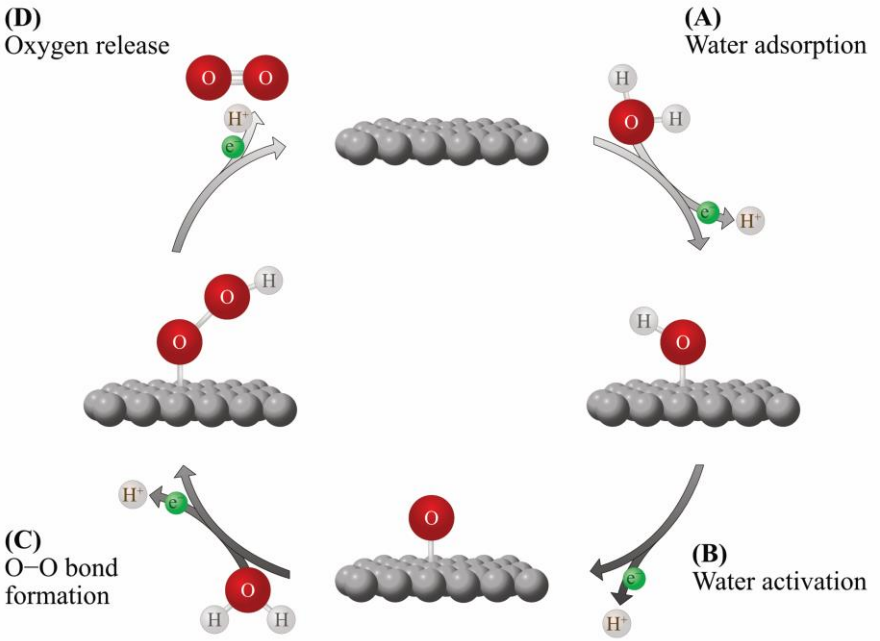

*Figure 1.4: Schematic illustration of one OER mechanism with **(A)** water adsorption, **(B)** water activation, **(C)** O–O bond formation and **(D)** oxygen release. Grey balls represent the surface, red balls oxygen, white balls hydrogen, green balls electrons and white balls with slight shade of orange protons. In all those steps, protons remain in solution whereas electrons are removed* via *the solid electrode.*

formation is often considered to be the rate determining step.[32,33] Finally, in **(D)** the superoxide is activated, generating molecular oxygen, which desorbs from the surface. Besides the presented mechanism there are also other proposed.[29,34,35]

According to the Sabatier principle the most reactive surface neither adsorbs the intermediates too strongly, nor too weakly. With density-functional theory (DFT) calculations, the adsorption free energies for the intermediates of this reaction on metal and metal alloy surfaces were calculated, revealing a linear scaling relationship of ΔG_{OH^*}, ΔG_{O^*} and ΔG_{OOH^*} with [10,25,30,31,36,37]

$$\Delta G_{OOH^*} = \Delta G_{OH^*} + 3.2\ \text{eV} \tag{1.7}$$

Here, ΔG_{OOH^*}, ΔG_{OH^*} and ΔG_{O^*} are the adsorption free energies for the superoxide, the hydroxide and the oxide on the surface, respectively. Since ΔG_{O^*} lays in between ΔG_{OOH^*} and ΔG_{OH^*}, the activity of a given surface for the OER can be estimated based on the adsorption energy descriptor $\Delta G_{O^*} - \Delta G_{OH^*}$. The activity of different alloys can be plotted *versus* the calculated adsorption energy descriptor of their surface. Those plots are called volcano plots, based on their shapes, and verify the above introduced estimation. An example of the volcano plot for the OER is shown in Figure 1.5. The surfaces on the left leg of the plot bind the intermediate too strongly, whereas the surfaces on the right leg bind them too weakly. The surfaces with the highest activity are located at the tip of the plot. Hence, volcano plots are used to screen surfaces and propose novel materials as promising catalysts with the right binding energy of the adsorbates on the surface. A common strategy therefore is to combine materials from the left and the right leg to achieve just the right binding energy. In addition, there are also other approaches to increase the catalytic activity, which will be introduced below in Chapter 1.3.

1.2.2 Hydrogen Evolution

As noted in the introduction, hydrogen as energy carrier ideally produces no harmful products when used in a fuel cell and offers the possibility to transit to a carbon neutral energy society. Unfortunately, nowadays the majority of hydrogen is produced by steam gas

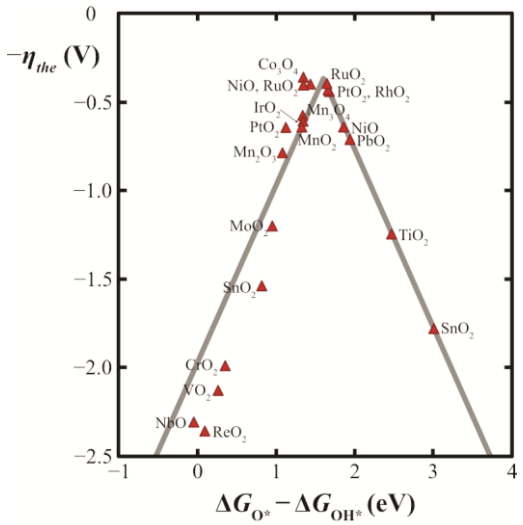

Figure 1.5: Volcano plot of the intermediate binding energy descriptor $\Delta G_{O^*} - \Delta G_{OH^*}$ and the corresponding theoretical negative overpotential for OER. Adapted from Ref (38) licensed under CC BY 4.0 with the original data and plot provided by Ref (39) and Ref (31), respectively.

reforming and water-gas shift reaction, which takes natural gas as reagent and emits carbon dioxide in the process as by-product. A promising carbon neutral way to produce hydrogen is by water splitting, powered by renewable energy sources such as wind or solar. As for the OER, also the HER reaction equation can be expressed differently, depending on the medium used. In acidic conditions it can be expressed as:

$$2\ H^+ + 2\ e^- \rightleftharpoons H_2 \qquad (1.3)$$

And in alkaline conditions as:

$$2\ H_2O + 2\ e^- \rightleftharpoons H_2 + 2\ OH^- \qquad (1.8)$$

Analogous to the OER, also here Le Chatelier's principle illustrates a favourable condition for the HER. However, in direct contrast to OER, the HER is benefited in acidic conditions, whereas it is hampered in alkaline media. The reason behind this is that in alkaline media water is used as proton donor. Hence the adsorption and electrochemical desorption step, shown below in Figure 1.6, require an additional

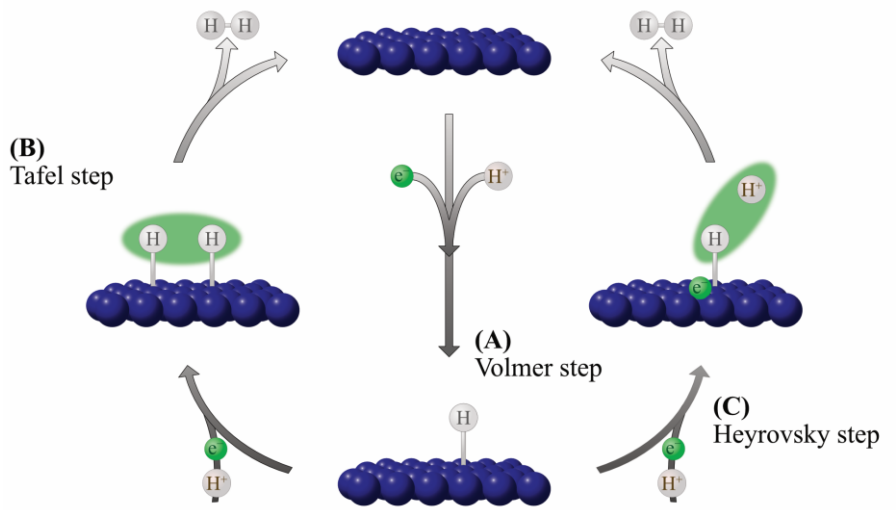

*Figure 1.6: Schematic illustration of the HER mechanism in acidic conditions with **(A)** Volmer, **(B)** Tafel and **(C)** Heyrovsky step. The blue balls represent the surface, white balls hydrogen atoms, white balls with slight shade of orange protons, green balls electrons and the green ellipses in **(B)** and **(C)** the electron density. In all steps, protons are present in the electrolyte and electrons are provided* via *an external circuit to the electrode surface.*

energy demanding water dissociation step.[29] A generally accepted reaction mechanism for the HER on surfaces can be illustrated with three different steps, here just shown for the reaction in acidic media.[25,40]

The Volmer step in Figure 1.6 **(A)** can be seen as a simple adsorption of a proton, forming a hydrogen atom bond to the surface. The Tafel step in **(B)** describes the recombination of two adsorbed hydrogen atoms on the surface in close distance. The Heyrovsky step in **(C)** describes an electrochemical desorption process in which the adsorbed hydrogen recombines with an approaching proton in solution with a simultaneous electron transfer from the surface of the substrate to the desorbing molecule.

In so-called Tafel plots the rate determining step for the reaction can be detected based on the required overpotential for achieving the next decade in current density. The derivation of the Tafel plot will be

discussed in Chapter2.3.1. With 30 mV dec^{-1} the Tafel step has the lowest Tafel slope of all three steps. Surfaces with this rate determining step indicate a high activity towards HER. The Heyrovsky step exhibits a Tafel slope of 40 mV dec^{-1}, indicating slightly slower reaction kinetics than the Tafel step. In contrast the Volmer step yields a Tafel slope of 120 mV dec^{-1} and indicates a less active surface for HER. Due to the necessary water dissociation step, this Volmer step is often rate determining for HER in alkaline media, and a reason for the poorer performance of many surfaces compared to in acidic conditions.[41]

As elaborated above, the bond strength of the adsorbate (here hydrogen) to the surface is important for the overall reaction activity. As for the OER, also for the HER this instance can be illustrated with a volcano plot (Figure 1.7). Following again the Sabatier principle – the intermediate should not be bond too strongly and neither too weakly to the surface – the optimal binding energy for the HER is found at approximately $\Delta G_{H^*} = 0$ eV. As illustrated in the volcano plot in Figure 1.7, platinum possesses hydrogen adsorption energies close to 0. This is one reason why platinum is the benchmarking catalyst for the HER. Rising effort is made to find new materials with similar binding energies to drive the reaction as efficient as possible, but in contrast

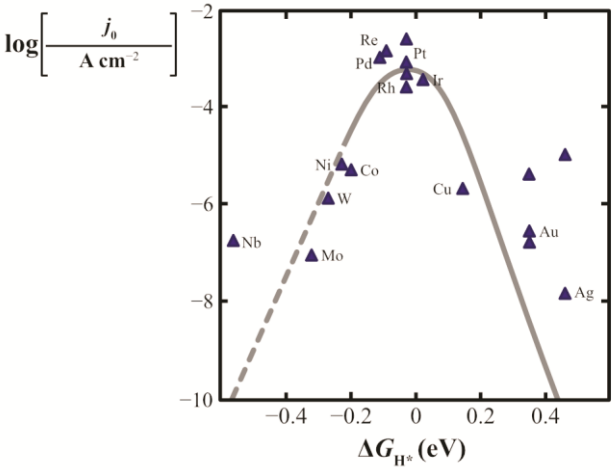

Figure 1.7: Volcano plot of H adsorption energy to the surface (ΔG_{H^*}) and the detected exchange current density j_0 as descriptor for activity towards the HER. Adapted with permission from Ref (44). Copyright 2022 American Chemical Society.*

to platinum being abundant and inexpensive. Besides the hydrogen binding energy, also other parameters have been revealed to influence the activity of a surface towards HER.[42,43]

Driving the desired reaction as efficient as possible can be seen as the job description for a catalyst, which will be discussed in the next chapter.

1.3 CATALYSTS

In order to drive the desired reaction as efficient as possible, highly active, selective and stable catalysts are vital. As explained above, the adsorption energy of the intermediates to the catalytic surface is an influencing factor for the overall activity, however, several more parameters have to be considered. In general, there are two strategies to improve the performance of catalysts. In one strategy, the intrinsic activity of the catalytic active site is enhanced, in the other strategy the number of active sites is increased.[25] Improving the intrinsic activity can be implemented among others by facilitating the rate determining step of the reaction, increasing the electron conductivity to the active site, or utilizing synergetic effects of different elements. For increasing the number of active sites there is a variety of techniques available. Some strategies discussed in this thesis are forming oligomeric complexes in Paper II, atomic dispersion of the active sites in Paper III and nanostructuring of the catalyst in Paper I and Paper IV. Clearly, the most promising catalysts are the ones combining both, enhanced intrinsic activity and increased number of active sites.

There are different families of catalysts and thus their strategies might differ. In this chapter the different classes of catalysts investigated in this thesis, their advantages and limitations are presented.

1.3.1 Molecular Catalyst

The legend of Sir Isaac Newton developing the idea of gravity by observing the falling apple might represent one of the most well-known scientific breakthroughs based on the observation of processes appearing in nature. As time has passed since Newton's discovery, the analytical tools in the scientific community have been significantly

improved, allowing now the detailed investigation of a manifold of natural processes, even the one of desired chemical conversions. With hydrogenases and nitrogenases, two families of enzymes have been detected producing hydrogen. With the investigation of these enzymes, not only the catalytic active centre was detected but also the beneficial influence of its environment with for example side groups stabilizing the catalyst and lowering thermodynamic and kinetic barriers during the reaction. Unfortunately, enzymes are challenging to synthesize in sufficient amounts and are unstable outside of their biological habitat.[45]

Taking the inspiration from nature of tuning the active sites by its surrounding without the drawbacks of a biological system is the motivation behind molecular catalysts. Molecular catalysts are transition metal complexes with the central metal ion coordinated by small (mostly) organic molecules as illustrated in Figure 1.8. The metal acts as active site at which the desired reaction takes place, whereas the organic molecules tune the activity of the active site by among others electron donating or withdrawing properties or stabilization of reaction intermediates. The superior nature of molecular catalysts is clearly visible for example for a DuBois type catalyst, a nickel complex directly inspired by Fe−Fe hydrogenase, which catalyses the hydrogen evolution reaction up to 106 000 times per second, thus outcompeting the Fe−Fe hydrogenase with 9 000 times per second.[45] However, the overpotential for the DuBois type catalyst was quite large for this turnover frequency, indicating that the electrochemical activity descriptors should be seen with more context (see more in Chapter 2.3).

Since this thesis includes work on ruthenium-based molecular catalysts for the oxygen evolution reaction (Paper II), the influence of the organic molecules – so-called ligands – bond to the metal centre is demonstrated for such a catalyst. As previously mentioned, the effect of the ligands can be of electron donating or withdrawing nature. In an electrocatalytic water oxidation process the redox potential of the catalyst is risen to a level, at which it withdraws electrons from the reagent. The potential necessary to drive this reaction is heavily influenced by the ligands. Electron density donating ligands around the ruthenium centre lower the potential required to oxidize the

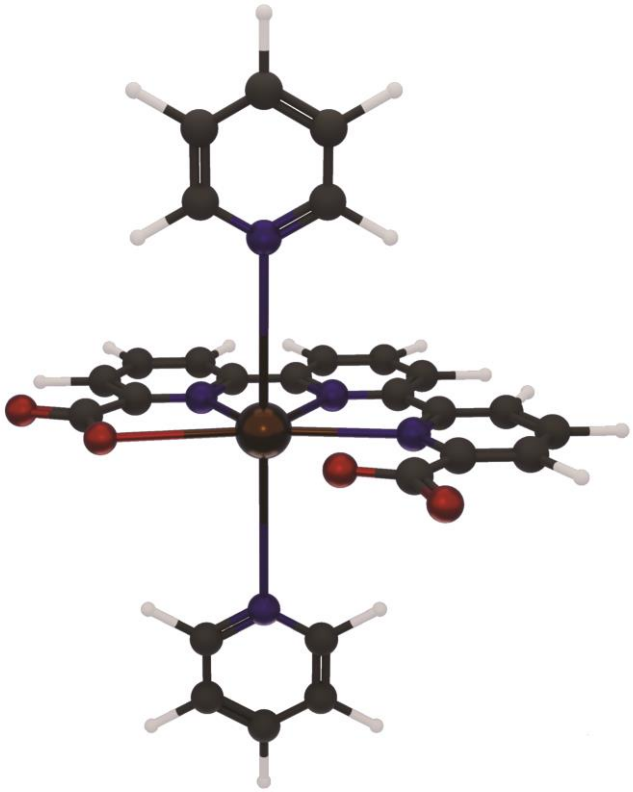

Figure 1.8: Schematic drawing of a molecular catalyst represented by Ru(tda)(py)$_2$ with tda being [2,2′:6′,2′′-terpyridine]-6,6′′dicarboxylate and py pyridine. Atoms are illustrated as balls. Ruthenium in brown, nitrogen in blue, oxygen in red, carbon in dark grey and hydrogen in white.

complex and thus to obtain the active species.[46] Furthermore, proton-coupled electron transfer (PCET) balances the coulombic charge as a consequence of the removal of one electron by the removal of a proton, which lowers the energetic barrier for the oxidation.[47,48] As an additional effect, deprotonated acidic groups surrounding the active centre may act as initial proton acceptor, facilitation the often rate determining O−O bond formation step.[48,49] The monoatomic nature of those complexes ensures that 100 % of the synthesized centres can act as active site and contribute to the oxygen evolution reaction. In addition, ruthenium-based water oxidation catalysts are reported to be stable and active, even in strong acidic conditions.[49–51]

Unfortunately, most of those molecular complexes are used in

homogeneous catalysis, meaning dissolved in the electrolyte and not permanently anchored on the electrode. This hampers the use of molecular catalysts in devices but sparked emerging research on the immobilization of this class of catalysts.[52–58] To this end, Paper II presents the performance and stability of immobilized ruthenium-based molecular catalysts as electroanodes for water oxidation applications in neutral pH.

Besides the challenges in anchoring the catalysts on electrodes, other disadvantages of this class of catalysts are among others the time and energy consuming synthesis of the complexes, the risk of oxidizing organic molecules at too high applied potentials during the OER with the formation of nanoparticles, and the labile ligand−metal bonds of first row transition metal complexes, which demonstrate a serious stability issue for those catalysts.[46,54,59–62]

1.3.2 Single Atom Catalyst

Having all metal centres active is a major benefit of molecular catalysts. One of the strategies to keep this advantage but to improve the stability of the catalyst and to heterogenize it is to expose molecular complexes to a pyrolysis process, often in the presence of a substrate like carbon nanotubes (CNTs) or carbon black.[63–65] During this step the organic material decomposes under high temperatures and in an inert atmosphere into a graphitic matrix with the metal still bond to the nitrogen from the complex. Ideally, single metal atoms distributed in a porous and nitrogen doped graphitic material are obtained as schematically represented in Figure 1.9. Due to the nature of single atom dispersed active centres, this family is called single atom catalyst (SAC). The so developed heterogenized metal atoms embedded in a highly electron conductive matrix comes with the sacrifice of losing the benefits of fine tuning the active site by customized ligands. Furthermore, in most processes the formation of undesired nanoparticles seems to be inevitable. Only metal atoms in contact with the electrolyte can catalyse the reaction, hence atoms buried in the bulk can be seen in some instances as loss of possible active sites, but this will be discussed in more depth in the next subchapter.[43,65] In addition, most nanoparticles are not stable in acidic conditions and are removed either in an acid treatment step subsequent to the synthesis

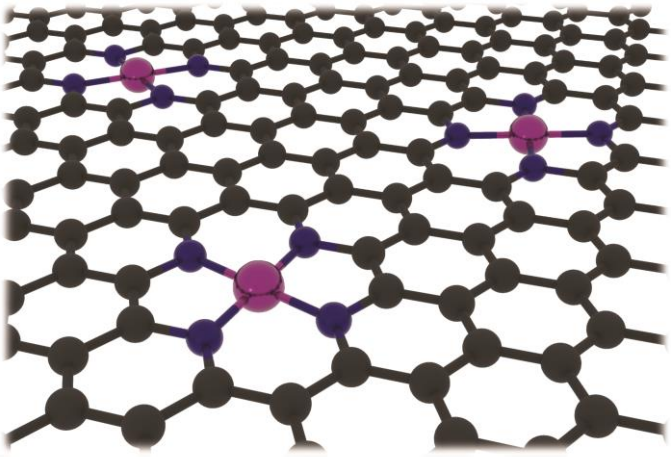

Figure 1.9: Schematic illustration of a single atom catalytic material. The black balls represent carbon atoms, dark blue balls nitrogen atoms and pink balls the active metal centre, here cobalt. The double bonds in the graphitic sheet are omitted for clarity.

or *in situ* during operation. Besides molecular complexes, also metal organic frameworks (MOFs) have attracted great attention as precursors for SACs.[65–67] MOFs are generally constructed from so-called nodes with organic molecules as linkers in between them. By using different organic molecules as linkers and metal ions or oxides as nodes, a large variety of MOFs with among others tuneable morphology, porosity, surface area and conductivity can be synthesized. As for the molecular complex, this starting material converts during the pyrolysis ideally into single metal atoms dispersed in a highly conductive, porous and N-doped carbon matrix.[68] A particularly interesting subfamily of MOFs are zeolitic imidazolate frameworks (ZIFs), which were used as starting compound in Paper III. ZIFs are constructed from metal nodes linked by imidazolates. Those frameworks exhibit high surface areas and superior structural integrity even after carbonization, leading to highly porous SACs.[68]

However, besides the apparent advantages of this catalyst family as a high electron conductive matrix, a large number of active sites as well as a straight forward synthesis, carbon-based catalysts are prone to degrade under operation at high applied potentials, which imposes challenges on this class of catalyst for the water oxidation reaction.

Additionally, the carbonization at high temperatures and under an inert atmosphere is an energy consuming step, which displays besides the unwanted but inevitable nanoparticle formulation a clear drawback.

1.3.3 Nanoparticle Catalyst

Despite being so far labelled as undesired and its formation as a disadvantage, nanoparticles are an important class of catalysts. Nanoparticle catalysts are usually metal alloys, oxides, chalcogenides or pnictides assembled in small geometries. In stark contrast to molecular catalysts or single atom catalyst, those catalysts can already be synthesized on a larger scale in solvothermal or hydrothermal processes at elevated temperatures in a time span of only a few hours. An additional advantage of those catalysts is the possibility to directly synthesize them on the electrode. With this there is no need for anchoring strategies by chemical interactions of the catalysts with the substrate (as generally for molecular catalysts) or the need of additional binders, gluing the catalysts onto the electrode (as usually done with single atom catalysts). Especially electrodeposition of the catalyst directly on the electrode is a promising and upscalable method for large scale production.[18,69–71] For molecular catalysts and SACs the formation of nanoparticles during the synthesis or operation is unwanted, however the risk of nanoparticle formulation directly displays the higher thermodynamic stability of nanoparticle catalysts over the formers. Since a major disadvantage of nanoparticles is bulk atoms not being able to act as active sites in the reaction, a considerable effort was dedicated to the synthesis of different nanostructures,[25] shown in Figure 1.10. Regardless of rod-, needle-, flower-, sheet-, or other shapes, all structures aim to expose as many atoms to the electrolyte as possible. Besides building up nanostructures with a high surface area during the synthesis, in the recent years also the strategy of leaching or dealloying of certain elements of the nanostructure in a post synthetical step was introduced, which further increase the number of active sites and the activity of the material remarkably.[25,72–74] In addition to increasing the number of active sites by controlling the morphology and porosity, also the intrinsic activity of nanoparticles can be significantly improved by combining different elements.[10,75–77] This can be done for example

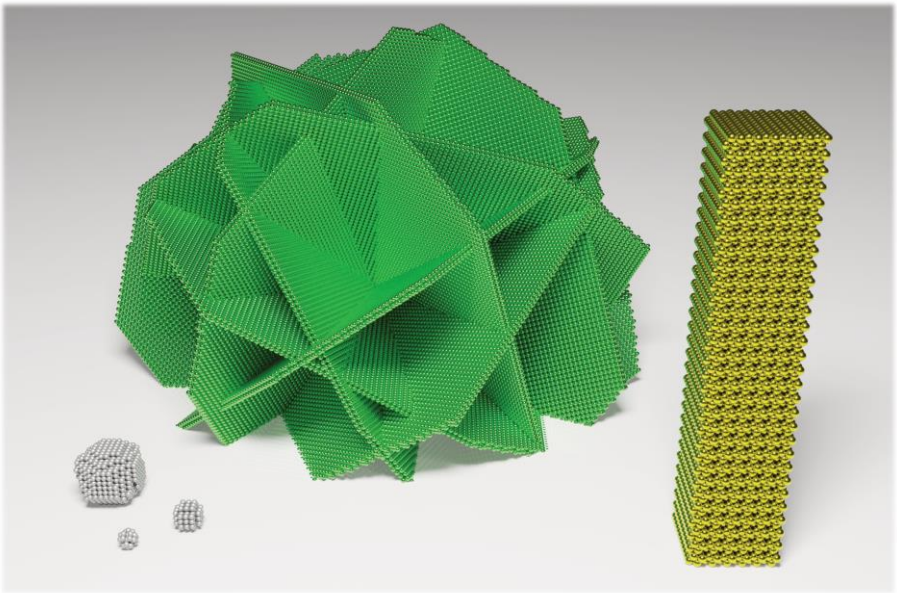

Figure 1.10: Schematic illustration of different nanostructures. Front left: Grey nanoparticle spheres in different sizes as for example for platinum on carbon. Middle in the background: Green nanosheets assembled to a nanoflower as for example for the nanosheet-shaped nickel molybdate hydrate. Front right: Yellow nanorod structure as for example for the rod-shaped nickel molybdate hydrate.

by selecting elements or materials from both legs of the Tafel plots to provide a more favourable intermediate binding energies, as mentioned in Chapter 1.2.1 and Chapter 1.2.2.[74,78] On the basis of this strategy it can be seen, that bulk atoms in nanoparticles cannot always be seen as "loss of active sites", since some of them are intended from the very beginning to tune the active site and not be the active site themselves.[33,79]As previously mentioned, nanoparticles are more stable than molecular catalysts and SAC and can thus be operated at higher potentials without the risk of catalyst degradation. However, reports have shown that for OER often a dynamic reformulation of the surface happened, creating metal-hydroxides or oxyhydroxides, which act as active phase. Thus, the actual active catalyst might differ from the synthesized material.[19,80,81] Thankfully, *operando* techniques can resolve uncertainties and detect the active phase during catalysis.[82,83]

Unfortunately, metal oxides are generally known to have a low electron

conductivity, which can hamper its activity. Additionally, in acidic media there are no known stable nanoparticle catalysts apart from platinum. Even the noble metal catalysts IrO_2 and RuO_2 show dissolution at too high applied potentials.[19] However, with a theoretical approach numerous stable and active non-noble metal oxides for OER in acidic media have been proposed.[26]

With the tuneable intrinsic activity, the large number of active sites, the superior stability in operation, and the facile synthesis of high loadings directly on the electrode, this class of catalysts is clearly more than just the unwanted by-product of a molecular or single atom catalyst. From my perspective, nanoparticle catalysts are highly likely the type of catalyst, which will be found in the revolutionary electrochemical cells of the near future.

2 METHODS

To investigate the catalysts, several different characterization techniques were utilized to examine among others nanostructures and morphologies, elemental composition, molecular structure, and activity and stability during operation. The most frequently techniques used in this thesis are introduced in the following in more detail.

2.1 SCANNING ELECTRON MICROSCOPY

In order to investigate the morphology of the surface, shapes and sizes of nanostructures and to conduct a qualitative elemental analysis, scanning electron microscopy (SEM) can be used. Electron microscopy is necessary, since the conventional light microscopes are not achieving the required resolution. According to the Rayleigh criterion (2.1), the maximum resolution, $R_{\max}$, accessible with a microscope is limited by the wavelength of the incident beam.

$$R_{\max} = \frac{1.22 \times \lambda}{NA} \tag{2.1}$$

In which λ describes the wavelength of the incident beam and NA the numerical aperture of the microscope. Even for a light microscope using 400 nm as the wavelength of the probing beam, the maximum theoretical resolution is around 203 nm, neglecting all possible errors of the instrument.[84] It becomes obvious that in order to reach higher resolutions, the probing beam needs to have a smaller wavelength. Louis De Broglie postulated in his doctoral thesis the wave−particle duality of electrons, for which he received in 1929 the Nobel Prize in Physics. Similar to photons, the wavelength of electrons is related to its energy and can be calculated with

$$\lambda = \frac{hc_0}{E} \tag{2.2}$$

With h being Planck's constant (6.626×10^{-34} J s), c_0 the speed of light (299 792 458 m s^{-1}), and E the energy of the electron. In electron microscopes electrons are accelerated to energies often up to 20 000 eV. With this amount of energy, they exhibit a wavelength of

approximately 0.062 nm, much smaller than the wavelength used in the light microscopes and thus enabling a much higher resolution.

In an SEM, electrons are generated at the electron gun, which can be a thermionic emitter as a tungsten hairpin or a lanthanum hexaboride crystal, or a tungsten field emission gun (FEG). For a FEG an electric potential between the tungsten tip and an anode below is applied, which is sufficient to extract electrons from the sharp tip of the gun. Those extracted electrons are focused by the Wehnelt cylinder and are accelerated towards a second anode, as illustrated in (Figure 2.1). The accelerated electrons entering further down in the SEM column magnetic lenses. Magnetic lenses are essentially copper coils through which a current is running. This induces a magnetic field, which deflects the entering electrons according to the Lorentz force. Unfortunately, not all electrons are focussed by the lens in the same back focal plane. Electrons with a lower energy are bend stronger in the magnetic field. This so-called chromatic aberration can be reduced by among others using a FEG instead of a thermionic emitter as electron source, since the former has a much smaller energy distribution of the emitted electrons.[85] In addition to chromatic aberration, electrons further away from the optical axis of the lenses are bend stronger than the ones closer to the optical axis, also resulting in different back focal planes. This is called spherical aberration. As the last aberration listed here, astigmatism is caused by the inhomogeneity of the magnetic field in the lenses. Electron waves propagating in different planes through the inhomogeneous magnetic field are also converging in different focal points. This is corrected with stigmators, which are controlled by the operator of the SEM. Unfortunately, all mentioned aberrations limit the maximum resolution of an SEM.

As illustrated in Figure 2.1, after the beam is shaped by the condenser lenses and the stigmators, it is deflected by scanning coils in x- and y-direction to scan the electron beam over the sample. With the objective lens the electron beam is finally focussed on the desired area.

When hitting the sample, the *primary electrons* (PE) of the incident beam can interact with the atoms of the specimen, causing different emissions. The interaction volume of the different detectable radiations is depicted in the left part of Figure 2.2. The PE (Figure 2.2,

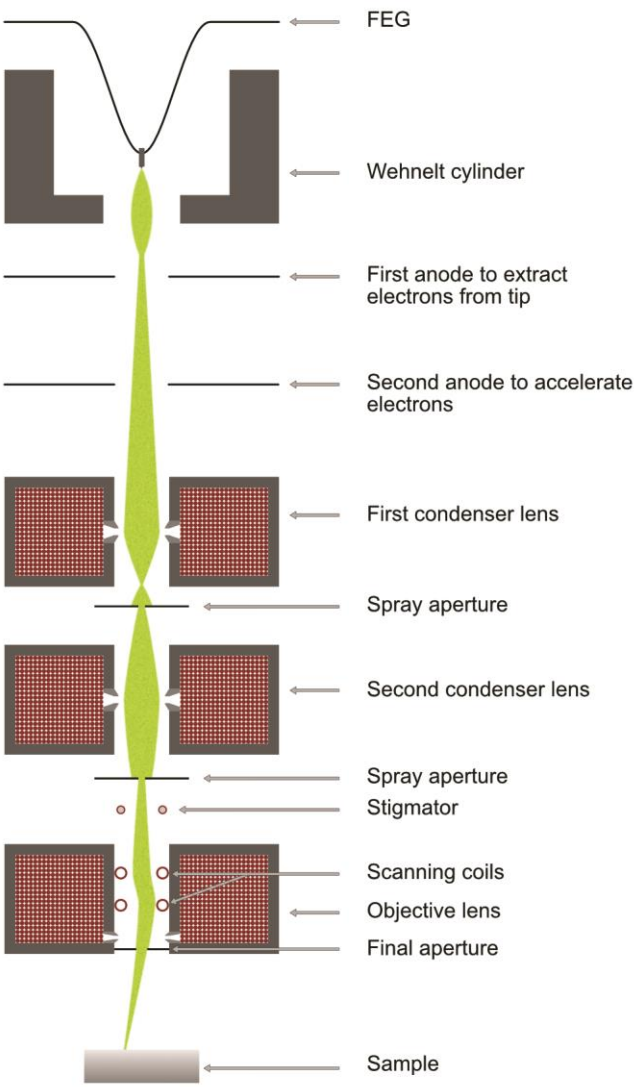

Figure 2.1: Schematic illustration of a column in a SEM, showing the electron beam in bright green from the FEG onto the sample. Depending on equipment, manufacturer and model the components and their location can vary.

right part **(A)**) can scatter inelastically at the electrons in the sample and hence kicking them out of the atomic orbitals. The so emitted *secondary electrons* (SE) **(B)** are detected and used to image the surface of the scanned area. Even though SE are generated further in the bulk material, only the ones emitted close to the surface (< 10 nm) are reaching the detector.[86] This is due to the low kinetic energy SE

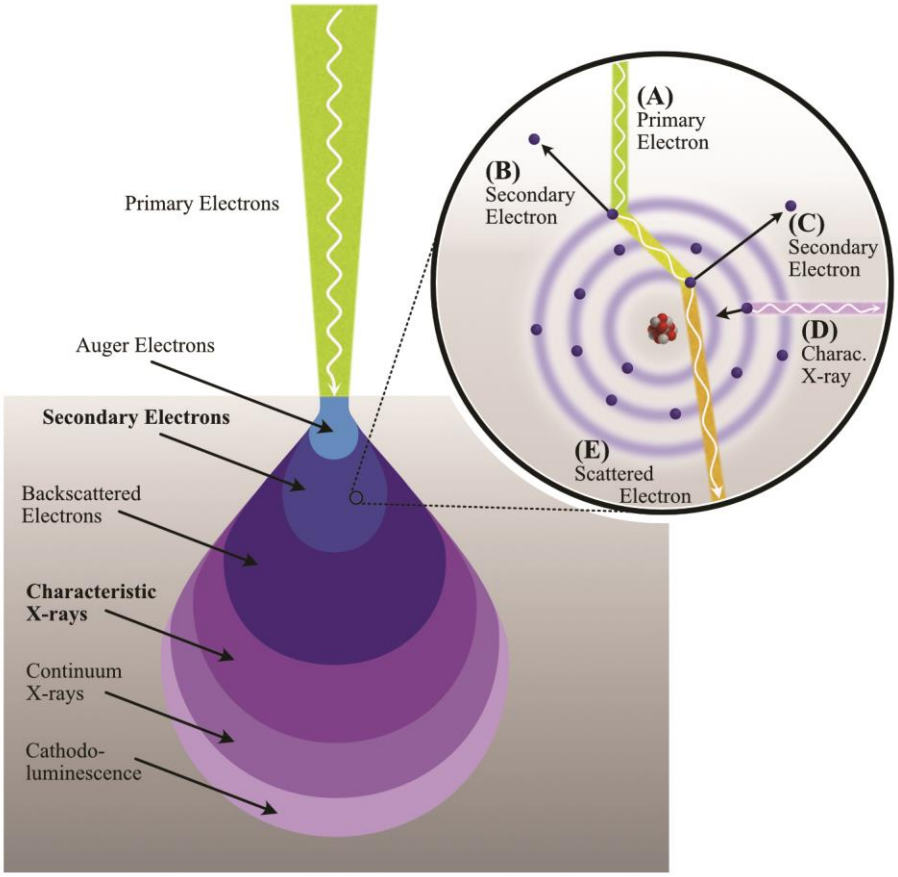

Figure 2.2: Schematic illustration of the electron-sample interaction volume and the resulting emissions. Only SE and characteristic x-rays play a role in this thesis. Their formation is shown in the upper right part of the image. ***(A)*** *incident primary electron;* ***(B)*** *secondary electron from outer shell;* ***(C)*** *secondary electron from inner shell;* ***(D)*** *emitted characteristic x-ray of outer shell electron when filling up the vacancy in the inner shell;* ***(E)*** *inelastic scattered primary electron penetrating the sample further.*

possess, which they lose rapidly in the bulk material. Hence, SE close to an edge have a higher probability to escape the sample than those in a flat region. This is the reason behind the edge effect, in which edges appear brighter in secondary electron images. Due to the emitted electrons, the surface charges positively. If not compensated by a sufficient electric contact from the surface of the sample to the sample holder, this can interact with subsequent emitted SE. Thus,

charging of the sample imposes challenges for the acquisition of secondary electron images of electric isolating samples.

When the primary electron knocks out an electron from an inner shell **(C)** of the sample atom, the created vacancy is filled up by an electron from an outer shell. By jumping in this vacancy, the electron emits radiation equal to the energetic difference of the previous occupied state in the outer shell and the vacancy in the inner shell **(D)**. The energy of this emitted *characteristic X-ray* is unique for different elements and transitions. Energy dispersive X-ray spectroscopy (EDX) is a technique detecting these X-rays and hence can be used to confirm the presence of certain elements in the sample material. Furthermore, with the electron beam scanning over the sample, also the location of the element can be detected. This mapping provides the possibility to probe among others for cluster formation or homogeneous dispersions of elements.

With every inelastic scatter process the PE lose energy. It is obvious that the depth, in which the inelastic scattered electron **(E)** has still sufficient energy to interact with the sample, is dependent among others on the sample material and the initial PE energy. As consequence, the size of the interaction volume is influenced by the acceleration voltage of the electron beam.

2.2 X-RAY PHOTOELECTRON SPECTROSCOPY

X-ray photoelectron spectroscopy (XPS) is a non-destructive surface sensitive technique for elemental analysis. At this point I would like to mention that it was developed by Kai Siegbahn and his group at Uppsala University under the name Electron Spectroscopy for Chemical Analysis (ESCA), for which he was awarded 1981 with the Nobel Prize in Physics.[87,88] A schematic XPS setup is illustrated in Figure 2.3. In XPS electrons are emitted at an electron source **(A)** and accelerated towards a metal anode **(B)**. In most instruments this metal anode is either made from aluminium or magnesium.

By bombarding the metal anode with electrons, *characteristic X-rays* are generated (purple traces in Figure 2.3) (explained in more detail in the EDX section above).[89] Those X-rays are diffracted by a

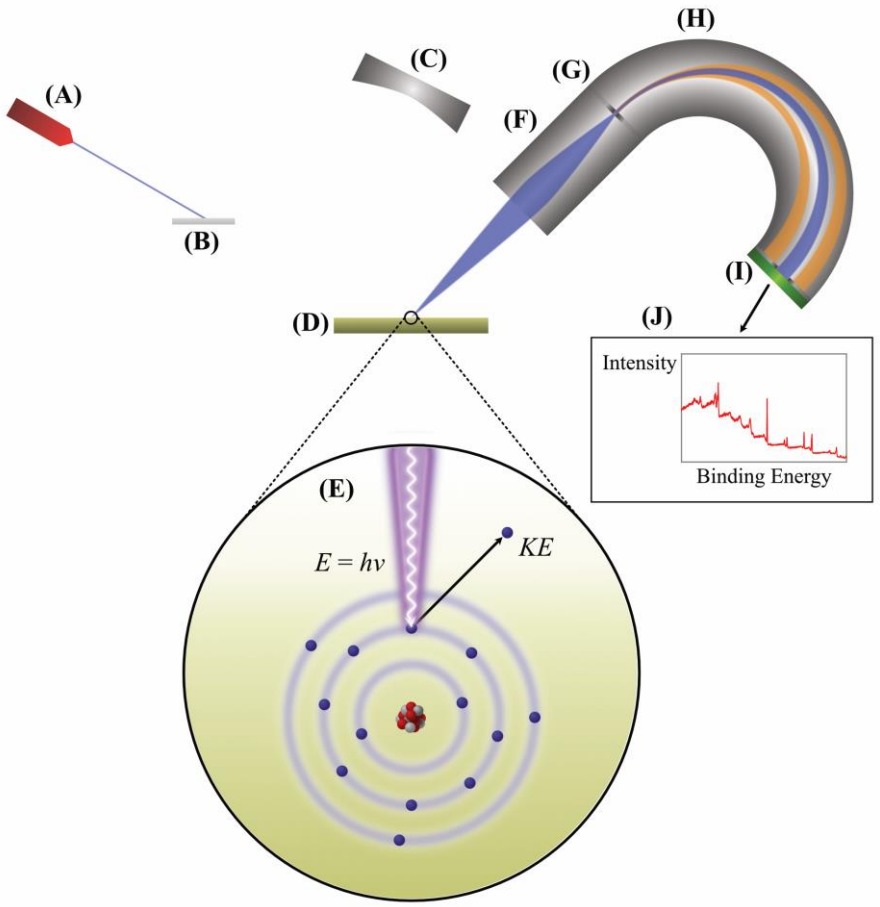

Figure 2.3: Schematic illustration of setup for XPS analysis. The electron and x-ray beam path and important interactions with the material are described in the text. ***(A)*** *Electron source;* ***(B)*** *metal anode producing x-rays;* ***(C)*** *monochromator focussing x-rays on the sample;* ***(D)*** *and* ***(E)*** *sample emitting photoelectrons;* ***(F)*** *column slowing down and focussing photoelectrons;* ***(G)*** *entrance slit of hemispherical analyser;* ***(H)*** *hemispherical analyser;* ***(I)*** *detector;* ***(J)*** *photoelectron spectrum.*

monochromator **(C)**, a quartz crystal oriented in a specific angle, such that only a certain wavelength is fulfilling Braggs equation and is focussed on the sample **(D)**. Incoming X-rays are exciting and ejecting electrons from the atoms, described as photoelectric effect **(E)**.[90] Those escaped *photoelectrons* have specific kinetic energies, based on the element, orbital, oxidation state and even the chemical environment of the atom to which they were bond. This makes XPS such a powerful tool, not only quantifying the elemental composition but also

providing information about the nature of the present elements. To detect this initial kinetic energy of the emitted photoelectrons they are slowed down by an electric field and focussed **(F)** on the slit **(G)** entering the hemispherical electron analyser **(H)**. In there a constant electric field deviates the photoelectrons trajectory to hit the detector **(I)**. The electric field in the column before the hemispherical analyser is responsible to slow down the electrons in such a way, that only electrons with a specific initial kinetic energy are entering the hemispherical electron analyser with the kinetic energy required to follow the path in the centre of the analyser and through the exit slit to the detector (blue traces in **(H)**). This energy value is denoted as *pass energy*. Photoelectrons entering the hemispherical analyser with higher or lower energies are deflected from this path and are not detected (orange traces in **(H)**).

During the XPS measurement, the strength of the focussing lenses and the electric field in the column before the hemispherical analyser are varied so that electrons with different initial kinetic energies are focused onto the entrance slit and slowed down to match the pass energy.[91] The electrons kinetic energy, KE, is converted to its binding energy (BE) following

$$BE = h\nu - KE - \phi_{\mathrm{spec}} \tag{2.3}$$

With $h\nu$ being the X-ray photon energy and ϕ_{spec} the work function of the spectrometer. The detected flux of photoelectrons for a specific binding energy is finally illustrated in the spectrum **(J)**.

Due to inelastic scattering events of photoelectrons in the sample, they might escape the surface with reduced kinetic energy or have produced lower energetic secondary electrons, which are emitted from the surface.[92,93] Both are detected as lower kinetic energy electrons.[94] This is the reason behind the characteristic "steps" in an XPS spectrum (see **(J)** in Figure 2.3) with a higher background at high binding energies than for low binding energies. Only photoelectrons which did not suffer from inelastic scattering contribute to the characteristic peaks used for the analysis. Those electrons are generated usually in depths of <10 nm and explain the surface sensitivity of this technique.[92,95] Besides photoelectrons also Auger electrons are

detected in XPS, but not further discussed here. In order to avoid scattering of photoelectrons by gas molecules on their path to the detector, the measurement is conducted in ultra-high vacuum. It should be noted that there are also other operation modes than the one described here. For the sake of simplicity, they are not further elaborated in this work.

2.3 ELECTROCHEMICAL ANALYSIS TECHNIQUES

In electrochemical analysis the response of current for a set electric potential between two electrodes (or *vice versa* for some techniques) is measured. Since in most of the used techniques in this thesis the electric potential is controlled and the current measured, the general explanation in the following will keep this relationship. Furthermore, it is acknowledged that electrochemical characterization is employed also in other scientific fields but the focus here lays on setups with a liquid electrolyte between the electrodes.

Current describes the flow of charge per time and thus represents the flow of electrons in the circuit. The measured current can be divided in *non-faradaic current*, which is not accompanied with a redox reaction, but instead with other processes such as adsorption and desorption at the electrode. In contrast, *faradaic current* is associated with a charge transfer process from the electrode to a species undergoing a redox process. This faradaic current could be further divided into a current, originating from a redox process of the electrode and/or catalyst, or the desired reaction as the hydrogen evolution or oxygen evolution. The latter can be referred to as *catalytic current*. All those contributions to the current are illustrated in a cyclic voltammogram below in Chapter 2.3.1.

Changing the potential applied to an electrode shifts the energy level of those electrons. Once the energy level of those electrons is below that of a species in close proximity, an electron transfer from the species to the electrode can thermodynamically appear, meaning the species gets oxidized (Figure 2.4 **(A)**). *Vice versa*, if the energy level of the electrons on the electrode is increased above the energy level of the species close by, an electron transfer from the electrode to the species can happen, meaning the species is getting reduced (Figure

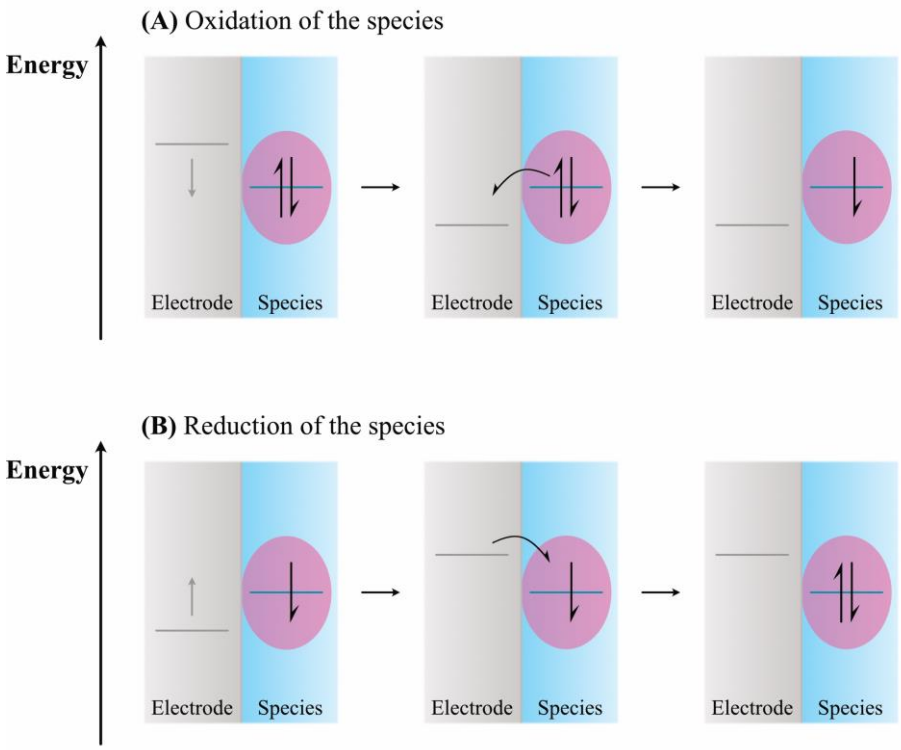

*Figure 2.4: Schematic illustration of the energy levels of electrons for **(A)** oxidation and **(B)** reduction of a species close to the electrode.*

2.4 **(B)**). The potential at which such a charge transfer occurs is called redox potential, E_{redox}, and can be calculated with the Nernst equation already introduced in Chapter 1.2

$$E_{\mathrm{redox}} = E^{0\prime} + \frac{RT}{z_e F} \ln\left(\frac{[\mathrm{Ox}]}{[\mathrm{Red}]}\right) \tag{1.4}$$

As mentioned above, as soon as the energy level of the electrons on the electrode exceeds or lays below the redox potential of the species, a charge transfer process is thermodynamically favourable. However, due to kinetic barriers in some reactions, a higher potential, $E_{\mathrm{react.}}$, has to be applied to overcome this barrier and drive the reaction. The additional potential is known as *overpotential*, η, with

$$\eta = E_{\mathrm{react.}} - E_{\mathrm{redox}} \tag{2.4}$$

Since it is difficult to determine at which applied potential the reaction

starts this overpotential is usually given for a certain current density, often at 10 mA cm^{-2}. Electrodes are generally decorated with catalysts to lower this overpotential and improve the kinetics of the reaction.

The applied potential at one of the electrodes is no absolute value, but describes a potential difference *versus* another electrode. In a two-electrode setup the potential difference is measured between the *working electrode*, at which the desired reaction is intended, and the so-called *counter electrode*. For a charge transfer process at the working electrode, let's assume it is a reduction, at the same time oxidation needs to happen at the counter electrode. The simultaneous oxidation is necessary to provide electrons to the working electrode through an external circuit, which then participate at the reduction process. In a two-electrode setup the corresponding current for an applied potential difference between working and counter electrode is observed. However, the contributions of the working and counter electrode to the overall kinetic barrier cannot be determined. Since one is usually interested in the processes happening at only one electrode, a three-electrode setup is commonly used. In this setup the potential difference between the working electrode and a *reference electrode* is measured, whereas the current still flows between the working electrode and the counter electrode. In such a way, possible limitations of the counter electrode are avoided and the performance of only the working electrode can be investigated. In general, even though one is examining the electrochemical response of the working electrode, the actual focus of interest of this thesis lays on the performance of the catalyst deposited on the working electrode, which is used to facilitate the desired electrochemical reaction. There are several different ways to evaluate and test the activity and stability of such an electrocatalyst, of which a few will be explained in the following.

2.3.1 Cyclic Voltammetry

Cyclic voltammetry (CV) is the technique of choice when investigating an electrocatalytic process. In cyclic voltammetry a potential is swept between two set limits at a defined scan rate and the current response is detected. Once one limit is reached the scan direction is reversed and the potentials are scanned in the opposite direction until the other limit is hit. A possible resulting cyclic voltammogram is shown in Figure

2.5. There are a lot of information that can be extracted from a CV. The most relevant for this thesis will be described here in short.

In regions where there is no charge transfer process **(A)**, the entire observed current is due to non-faradaic processes, which are among others scan rate dependent. With increasing the scan rate an increase in capacitive current can be detected. From this scan rate dependent non-faradaic current, the double layer capacitance can be determined, which is proportional to the electrochemical surface area (ECSA) of the electrode. This surface area is an important parameter for catalysis, since it can be often seen as descriptor for the amount of exposed catalytic sites to the electrolyte.

Following the grey arrow from **(A)** in Figure 2.5, when entering a potential window in which charge transfer is favourable, an onset of

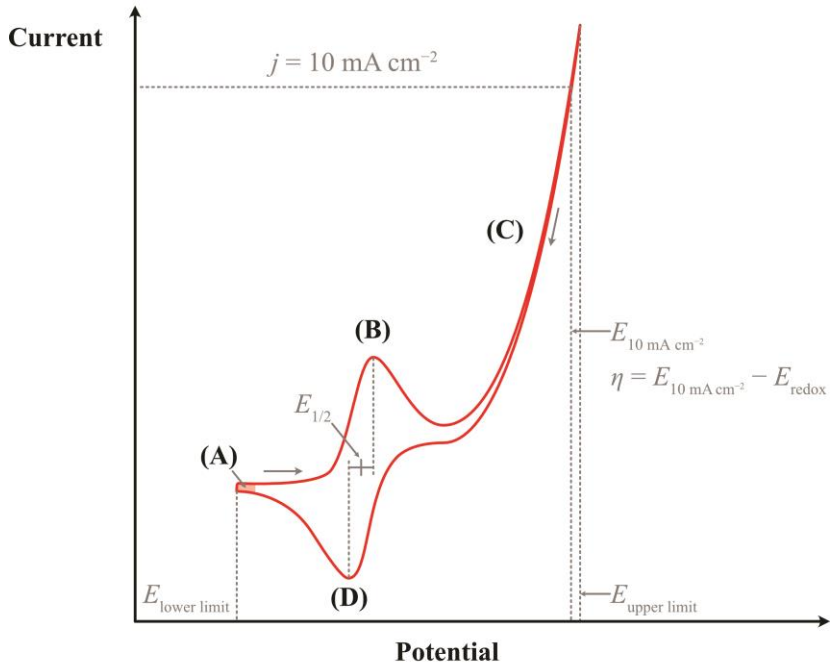

Figure 2.5: Schematic cyclic voltammogram for the illustration of key features. $E_{\mathrm{lower\ limit}}$ *and* $E_{\mathrm{upper\ limit}}$ *are set in the acquisition parameters.* $E_{1/2}$ *is the redox potential of the catalyst, whereas* E_{redox} *is related to the thermodynamic redox potential of the desired reaction.* $E_{10\ \mathrm{mA\ cm^{-2}}}$ *corresponds to the potential at which the current density of 10 mA cm*$^{-2}$ *on the catalytic wave is reached.*

increase in current can be observed **(B)**, caused by oxidizing a nearby species. In the presented illustration, the oxidation of a catalyst on the electrode is assumed. With increasing potential, the driving force for oxidation further increases, leading to a higher oxidation rate of catalyst, which is observed by a rising current. For even higher applied potentials, diffusion and mass transport can limit the oxidation rate of the catalyst, causing first a peak and then a decrease in observed current. With quantifying the consumed charge in such an oxidation step, the amount of substance of catalyst can be calculated. With further increased potential the driving force for catalysis might be sufficient and a strongly rising catalytic current is observed **(C)**. Charge transferred in this reaction is directly participating in the desired reaction. The activity of the catalyst is often described by the overpotential necessary to reach a certain catalytic current density. This value is taken from the catalytic wave as illustrated by the corresponding dashed lines in Figure 2.5. Another descriptor for the activity is the maximum turnover frequency of the reaction by one catalytic centre, which is evaluated by the foot of the wave analysis (FOWA) of the catalytic wave. In this region the reaction is expected to be not limited by among others mass transportation or diffusion.[96,97]

When reaching the upper limit of the potential window, the scan direction is changed and a decrease in catalytic current is visible until a potential is reached, at which the reaction is not favourable anymore. Further decrease leads to a reduction of the catalyst **(D)**. In cases in which both redox processes are observed, as here for the oxidation and reduction of the catalyst, the process is called *reversible*. For such processes, the potential halfway between the peak potential of the oxidation and the reduction, respectively, is denoted as $E_{1/2}$ and is equivalent to the formal standard potential of the given redox reaction.[98] The potential difference between the oxidation peak and reduction peak also includes information about how fast the electron transfer is.[99] Processes in which only one of the two redox features are visible are called *irreversible*. In Figure 2.5 the electrocatalytic reaction would represent an irreversible oxidation.

Besides the activity, with many subsequent cycles the integrity of the whole system can be probed. Shifts in the redox potentials of the catalyst, the shape of the peak or its reversibility as well as varieties in

the catalytic wave can provide information about changes of the system. Those changes could be due to activation processes, but also the instability of the catalyst and possible degradation. Especially for molecular catalysts, CV provides a lot of valuable information.

With slow scan rates – to assure nearly steady state conditions– the catalytic wave can be used to determine the rate determining step for the reaction. For this purpose, the catalytic wave is plotted with η over log(|i|). Such plots are known as *Tafel plots*. For larger log(|i|) the plot usually exhibits a linear regime, which slope provides information on the rate determining step. This was already previously presented in Chapter 1.2.2.

As mentioned with regard to the DuBois catalyst in Chapter1.3.1, electrochemical descriptor of activity, such as overpotential, turnover frequency and Tafel slopes should always be seen in a broader context. Ignoring the applied potential necessary to reach a certain turnover frequency or determining the overpotential for a small current could possibly paint a distorted picture of the actual activity of the catalysts. Furthermore, electrolyte temperature, reagent concentration or number of active sites are just a few parameters known to influence the performance of the investigated catalytic material and should always be considered when evaluating the (intrinsic) activity of the catalyst.

To compare electrochemical data with results of other electrode sizes, the current is usually reported as current density (current per area). However, with the development and employment of highly porous or three-dimensional electrodes in electrocatalytic processes, the normalization to an inaccurate area can lead to overestimations of the reported performance.[100] Proposals have been made to normalize the observed current to the electrochemical surface area, which would offer the possibility to compare the intrinsic activity of different catalysts.[18,69] However, from my point of view here the difference of academic and industrial interests is visible. Whereas in academia the true intrinsic activity of a catalyst seems to be more of interest it is anticipated that in industry the focus lays more on the current obtained at an applied potential for a given electrode size in the device, regardless of the actual surface area in contact with the

electrolyte.

2.3.2 Chronoamperometry and Chronopotentiometry

Besides cycling the working electrode in a potential range in which the electrical load is varied over time, the electrochemical response can also be observed for a constant load. For this purpose, chronoamperometry (CA) or chronopotentiometry (CP) can be utilized. In chronoamperometry a constant potential is applied at the working electrode and the current response is observed over time. *Vice versa*, in chronopotentiometry a constant current is applied and the required potential is detected. Such a measurement cannot only provide information about the stability of the system under a constant applied load, but also indicate the performance of the electrode in steady state conditions. Compared to other electrochemical techniques, chronoamperometry and chronopotentiometry are much closer to the actual conditions, in which the electrode would operate in an electrolyzer cell at a constant load.

By combining the electrochemical setup with an additional spectroscopic technique, for example Raman spectroscopy, the electrode can be investigated during catalysis. This spectroelectrochemical approach is of importance, since with the applied potential a phase transition might be induced, leading to another catalytic active phase than characterized *ex situ* beforehand.

2.3.3 Electrochemical Impedance Spectroscopy

Electrochemical impedance spectroscopy (EIS) uses the frequency dependent response for small perturbations in the applied load in an electrochemical cell. The perturbation can be done in the applied potential (potentiostatic EIS) or in the applied current (galvanostatic EIS). A short explanation is given for the potentiostatic mode. The applied potential is alternating perturbated. This perturbation is varied over a range of frequencies and differences in the current response dependent on the perturbation frequency is detected. In general, processes appearing in the electrochemical cell as for example charge transfer or mass transport are assumed to be active in different frequency domains and hence can be distinguished with this

technique.

With the collected data, these processes are tried to be modelled by in series or parallel connected capacitors, resistors, constant phase elements or impedance elements. The so constructed *equivalent circuit* approximates the electrochemical cell (or parts of it) with the parameters of each component describing the corresponding processes by an electrical equivalent. The obtained data for electrochemical impedance spectroscopy can be illustrated in different ways. One famous plot is the *Nyquist plot*, illustrated in Figure 2.6 for the corresponding *Randles circuit*.

In an equivalent circuit of the electrochemical cell in Figure 2.6 **(A)**, R_S represents the solution resistance of the electrolyte between the two electrodes. The capacitor C_{DL} represents the double layer capacitance of the electrode−electrolyte interface whereas R_{CT} represents the charge transfer resistance from the electrode to the electrolyte. Warburg impedance Z_W represents a kind of mass transfer resistance, but for the sake of simplicity will be neglected in the following. In Nyquist plots the resistance is illustrated on the real axis, whereas the capacitance is on the negative imaginary axis. High and low perturbation frequencies are represented in the Nyquist plot at low and high x-axis values, respectively. At high perturbation frequencies, only the resistance of the solution R_S is influencing the current response. Hence, the solution resistance can be detected in **(B)** at high frequencies where the impedance data crosses the x-axis. With a decrease of the perturbation frequency, the double layer capacitance

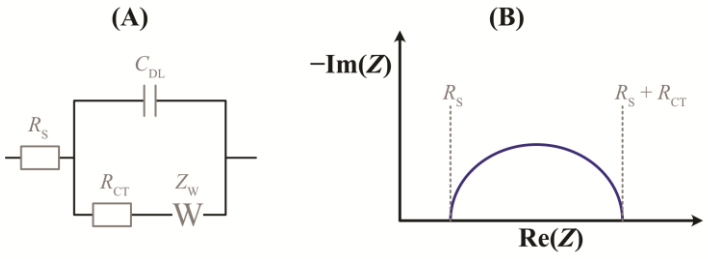

*Figure 2.6: Illustration of **(A)** Randles circuit and the corresponding Nyquist plot in **(B)**, for the sake of simplicity excluding contributions of the Warburg impedance Z_W.*

and the charge transfer resistance start to influence the response as well and a semicircle is formed. For lower frequencies the double layer capacitance has no influence on the observed impedance anymore, which is now only controlled by the solution and the charge transfer resistance. Hence the impedance ends up on the x-axis again at R_S + R_{CT}.

In a real cell the Warburg impedance cannot be neglected and more than one semicircle can appear in the spectrum, which furthermore can also partly overlap. In addition, the capacitor is often substituted by a constant phase element to compensate proposed roughness or heterogeneity of the electrode surface, which causes the system to deviate from an ideal capacitor.[101,102] All this complicates the exact analysis of electrochemical impedance spectroscopy and the construction of an equivalent circuit. In this thesis, only the solution and charge transfer resistances were extracted from the spectra.

2.4 RAMAN SPECTROSCOPY

Raman spectroscopy is a spectroscopic technique, which utilizes light-matter interactions (rotational and vibrational transitions) to provide information about present bonds. A schematic of light-matter interactions is shown in Figure 2.7. An incoming photon is in most cases elastically scattered from the electrons, meaning without loss nor gain in energy. This process is called Rayleigh scattering (Figure 2.7 **(A)**). It can be illustrated as an incident photon with the frequency ν_{L} exciting an electron from a initials state E_n to a virtual state, which lays in between the electronic ground state and the electronic excited state, followed by the relaxation of the electron back to the original state E_n. During this relaxation process the electron emits a photon with the same frequency as the incident photon ν_{L}. In rare occasions in electrons participating in bonding, the excited electron might relax to an energy state E_m different from the initial state E_n. In this case the emitted photon has a different frequency ν_{Ram} compared to the incident beam. This inelastic scattering process is called Raman scattering. The frequency of ν_{Ram} provides information about the energetic difference between the initial and final state, following

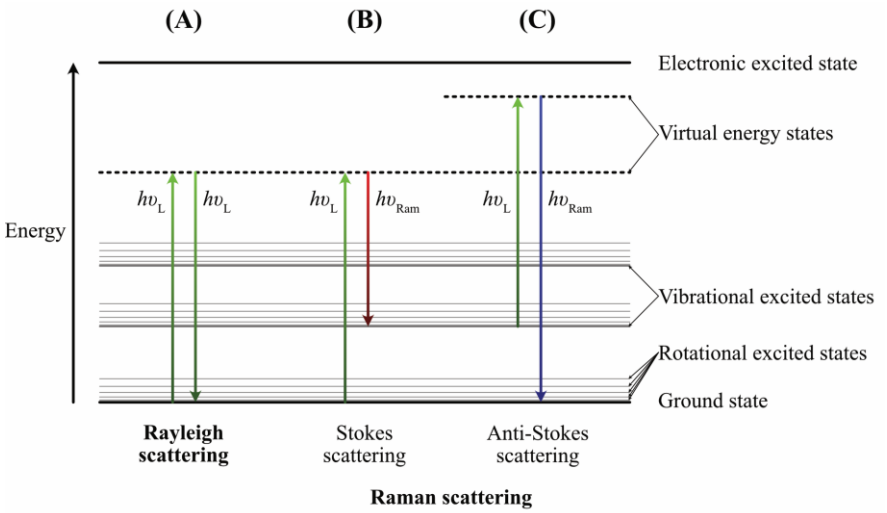

*Figure 2.7: Schematic of **(A)** Rayleigh scattering and in **(B)** and **(C)** Raman scattering processes with Stokes scattering and Anti-Stokes scattering, respectively, for a vibrational transition. Further rotational and vibrational states are omitted for the sake of clarity.*

$$\Delta E = E_n - E_m = h(\nu_{\mathrm{L}} - \nu_{\mathrm{Ram}}) \tag{2.5}$$

With E_n and E_m being the initial and final energetic states of the Raman scattering, h being Planck's constant and ν_{L} and ν_{Ram} the frequency of the incident and emitted photon. In Figure 2.7 **(B)** E_n corresponds to the energy level of the ground state, whereas E_m represents the first vibrational excited state. The energy difference ΔE is characteristic for rotational or vibrational transitions happening in the molecule and hence gives information about the present bonds. Raman scattering with $\Delta E > 0$ is called Stokes scattering, while scattering events with $\Delta E < 0$ is referred to as anti-Stokes scattering. For anti-stokes scattering to occur, the initial state has to be already excited, which cause this scatter process to be scarcer at room temperature than the Stokes scattering. In Raman spectroscopy monochromatic light is used as incident radiation. After the scattering process the light with the exact wavelength as the incident beam is cut out by a laser filter. Only the Raman scattered light passes through and reaches the detector. However, not all rotational and vibrational transitions of the sample material are visible in Raman spectroscopy.

The Raman activity can be described by *local selection rules*, where one can consider the effect of an electric field on a molecule. When a molecule is placed in an oscillating electromagnetic field, the electrodynamic forces distort the electron density in this molecule, inducing a dipole moment. This dipole moment is depending on the strength of the electric field and the polarizability of the molecule. One can imagine electrons are easier distorted by an electric field *along* the bond axis than *across*. Hence, the polarizability of a molecule can depend on their orientation in the electric field as illustrated for a hydrogen molecule in Figure 2.8. Such molecules are called *anisotropic polarizable*, which is required for rotational Raman activity as shown later. The polarizability of a molecule is represented by a polarizability ellipsoid and illustrated in the figures below as green oval. Against intuition, a larger polarizability corresponds to a smaller distance from the centre to the surface of the ellipsoid. In order to be Raman active, the polarizability has to change during the vibration or rotation, which can be displayed as change in shape, size and/or orientation of the ellipsoid.

Since in rotations, the shape and size does not change, the orientation of the ellipsoid during the rotation needs to change. Let's assume methane with a spherical ellipsoid rotating in an electric field. During the rotation the polarization of the molecule will not change. Hence,

Figure 2.8: Hydrogen molecule (white balls with line as bond) in electric field with corresponding polarizability ellipsoid (green oval) below. ***(A)*** *Hydrogen bond axis oriented parallel to electric field lines.* ***(B)*** *Bond axis oriented perpendicular to electric field lines.*

all rotations of this molecule are Raman inactive. In the case of a simple non-spherical ellipsoid like the one of hydrogen, during rotations in the electric field (except the rotation about its bond axis) the polarizability of this molecule changes, as shown in Figure 2.8 for two orientations. It can directly be seen that this results in Raman active modes. Hence, to be active in rotational Raman spectroscopy the molecule needs to be anisotropic polarizable and the orientation of the major axis of the ellipsoid needs to change during the rotation.

In contrast to rotations, vibrational modes can cause a distortion of the electron density in the molecule which alters its polarizability, represented by a change of size, shape or orientation of the major axis of its polarizability ellipsoid. Those changes are schematic illustrated for a water molecule in Figure 2.9 **(A)** – **(C)**, respectively. It is important to note that a change of the polarizability during the vibration is not sufficient to be Raman active. The polarizability has to change for small displacements around the equilibrium conditions, which can be expressed as

$$\left(\frac{\mathrm{d}\alpha}{\mathrm{d}\xi}\right)_{\xi=0} \neq 0 \qquad (2.6)$$

With α as polarizability, ξ as *displacement coordinate* and $\xi = 0$ as equilibrium position.

Carbon dioxide can be used as an example for Raman inactive vibrations. Its modes with the corresponding polarizability over displacement coordinate is shown in Figure 2.10. Only the symmetric stretching mode in **(A)** displays a change in polarizability for small displacements from the equilibrium position and is Raman active. Despite the change of size and shape of the polarizability ellipsoid during the asymmetric stretching and bending vibrations, there is no change in polarizability for small displacements from the equilibrium position and both modes are Raman inactive. Following the premise of a change of polarizability for small displacements around the equilibrium position for Raman active vibrations, vibrations with different magnitudes of change in polarizability are represented in the Raman spectra with different intensities: A vibration mode with a larger change of polarizability exhibits a Raman band with a higher intensity.

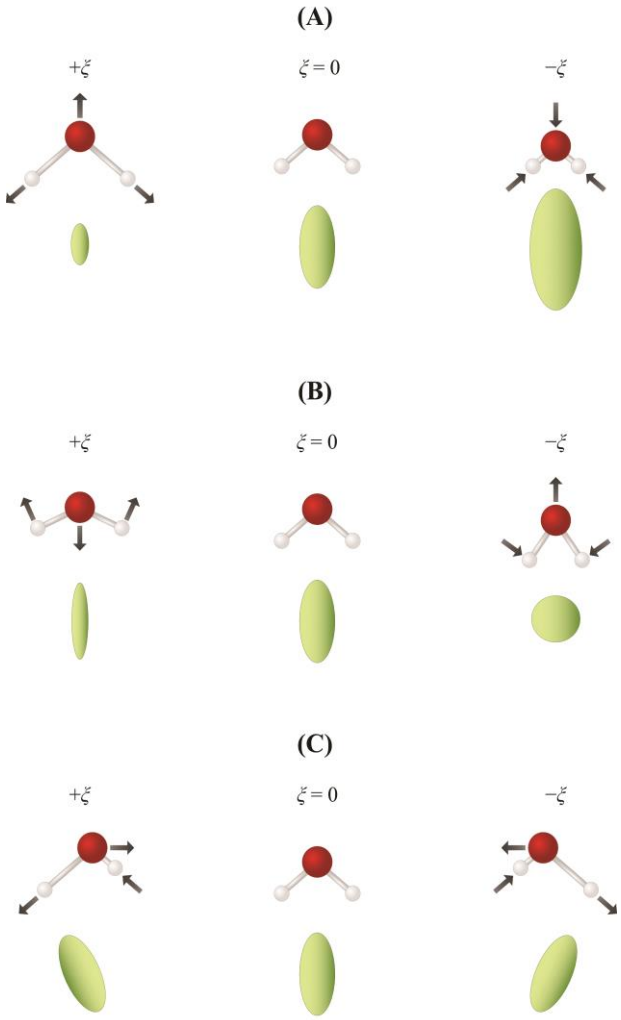

*Figure 2.9: Schematic illustration of water vibrations (red balls represent oxygen, white balls represent hydrogen) and their induced changes in the polarizability ellipsoid (green oval below) for **(A)** symmetric stretching (change of size), **(B)** bending (change of shape), **(C)** asymmetric stretching (change of orientation). All vibration modes are Raman active. ξ represents the displacement coordinate.*

Prediction of Raman activity for crystals is more challenging, since the just presented local selection rules for molecules are complicated with lattice selection rules and other lattice dependent scattering processes. Among others phonons, magnons, polarons and lattice defects can introduce Raman active modes, but this will not be further elucidated here.[103,104]

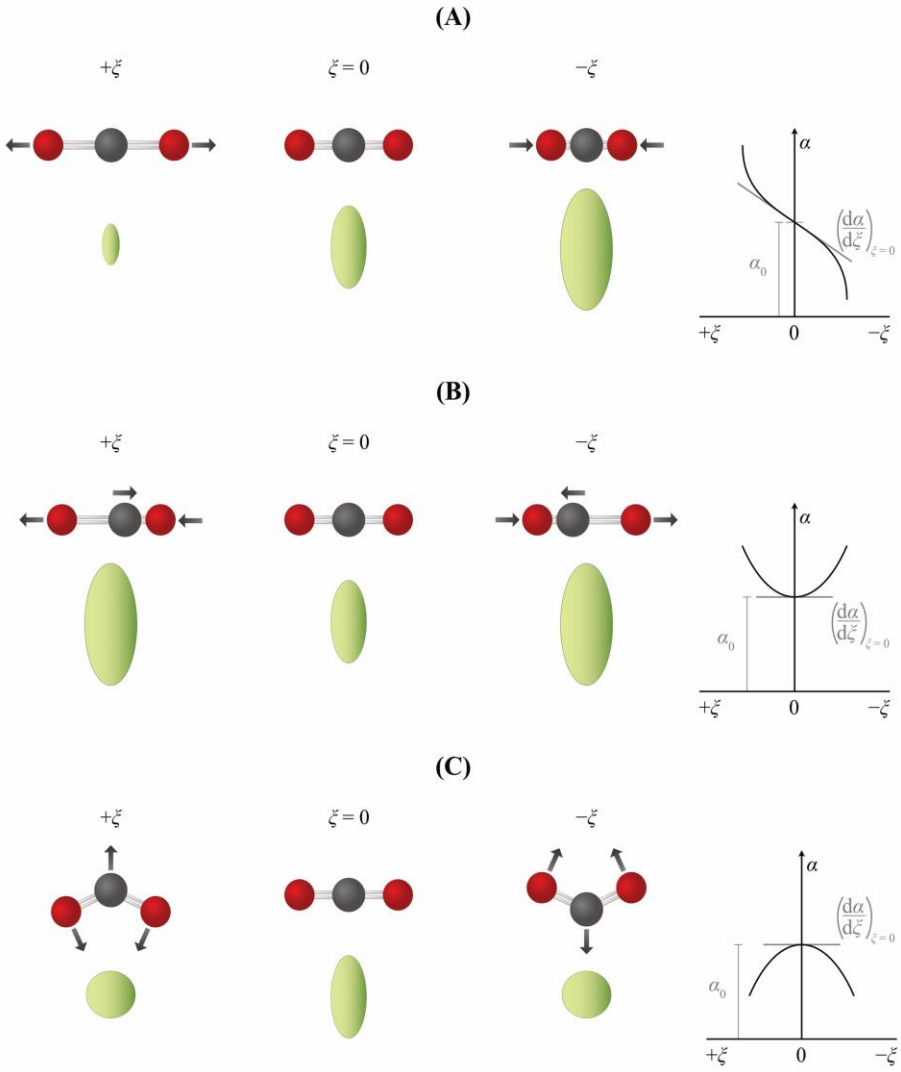

*Figure 2.10: Illustration of carbon dioxide vibrations (carbon atoms in dark grey, oxygen atoms in red) and the corresponding polarizability ellipsoids (green oval below) for **(A)** symmetric stretching, **(B)** asymmetric stretching and **(C)** bending modes. On the very right of each vibration is a plot of the polarizability over displacement coordinate during this vibration.*

Despite the complexity of predicting Raman active vibrations, Raman spectroscopy is an extremely useful technique for characterization. An additional advantage of this technique is the possibility to conduct *in situ* and *operando* measurements. With these, not only structural

changes of the material caused by exposure to the electrolyte can be observed, but also the actual active phase during catalysis can be determined. This is pivotal since the synthesized and characterized compound is not always the actual catalyst. Hence *operando* measurements can add valuable input for interpreting the results of other techniques and helps for a general understanding of the material.

3 Molecular Catalysts for the Oxygen Evolution Reaction (Paper II)

In this chapter, the work of Paper II is briefly presented and also put in a broader context. The principle question: "Can we utilize known active and stable ruthenium-based molecular catalysts for the oxygen evolution reaction in a device operating at neutral pH? And does it make sense?" is discussed and tried to be answered.

3.1 Introduction

Ruthenium-based molecular water oxidation catalysts (Ru-MWOC) are known to be highly active and stable in aqueous media.[48–54,105] In contrast to first row transition metal complexes, ruthenium-based complexes do not suffer from ligand exchange and are ideal to study the mechanism and influence of various equatorial and axial ligands. Started with the "Blue Dimer" in 1982 by the Meyer group,[105] Ru-MWOC have developed in the past 40 years, unlocking high activities and stabilities by tuning the environment of the active sites. With the publication of $Ru(bda)(pic)_2$ (bda being [2,2'-bipyridine]-6,6'-dicarboxylate and pic being 4-picoline), Sun's group presented a highly stable and active catalyst for OER in acidic media.[106,107] Unfortunately, this catalyst follows the interaction of two metal-oxo species (I2M) mechanism in homogeneous solution to split water. When anchored on the electrode, this bimolecular mechanism is not possible anymore and Ru(bda) was suggested to decomposed into RuO_2.[54,108] With $Ru(tda)(py)_2$ (tda being [2,2':6',6''-terpyridine]-6,6'' dicarboxylate and py being pyridine) a highly active and stable catalyst was presented by Llobet's group, which follows the water nucleophilic attack (WNA) mechanism (represented in Figure 1.4) already as homogeneous catalyst.[49] With this single-site catalytic mechanism, Ru(tda)-based catalysts are expected (and also reported) to be able to retain their performance once heterogenized.[27,53,60] In strong contrast, anchored catalysts following the I2M mechanism would be needed to be either dinuclear or to be anchored in close proximity to each other to interact in a intermolecular manner.[27] Despite the oligomer catalysts being multinuclear they are still suggested to follow the WNA

mechanism.[52,54]

Different approaches for anchoring catalysts have being reported in literature, among others alkyl chain alignment,[57,58] covalent bonding,[108] electropolymerization,[56] integration into a metal-organic framework (MOF),[55] by π−π stacking or supramolecular CH−π interactions.[52–54] With integrating a pyrene derivative pyp as the axial ligand in a previous work (pyp is 4-(pyrene-1-yl)pyridine), the successful heterogenization by π−π stacking interaction of the pyrene group with multi walled carbon nanotubes (MWCNTs) was shown for monomeric Ru(tda)-based catalyst, reaching over a million turnovers during catalysis.[53] After anchoring, the catalyst kept its activity and stability as reported in homogenous phase. With the development of new oligomeric catalysts, in which ruthenium centres are linked by bpy axial ligands (bpy is 4,4'-bipyridine), a Ru(tda)-based catalyst with 15 repetitive units could be successfully immobilized by CH−π interactions between the equatorial ligands of the catalyst and the π-system of the MWCNTs.[52] This strategy led to higher loadings and hence more powerful anodes. Interestingly, the identically synthesized Ru(bda)-based oligomeric derivative with 10 repetitive units did not suffer from decomposition as the covalently bond mononuclear complex.[54,108] The length of the oligomer chains could be calculated based on the ratio of the signal of the terminal and bridging bpy in proton nuclear magnetic resonance (^{1}H-NMR) spectroscopy.[52,54] Additionally, in contrast to the Ru(tda)-based catalysts used in Paper II, the proposed catalytic reaction pathway of the Ru(bda) oligomer includes the coordinating of two aquo species to the active centre.[54]

3.2 Performance on Device Electrodes for OER

In previous publications, presenting and characterizing the different catalysts and anchoring strategies, all catalysts were immobilized on MWCNT and drop casted on a glassy carbon electrode.[52–54] In order to probe their possible integration into a water splitting device, which operates in neutral pH, printed electrodes (PEs) provided by the collaborating Billon group at Université de Pau et des Pays de l'Adour (UPPA) were used as electrodes.

The catalysts used in Paper II before activation are shown in Figure 3.1.

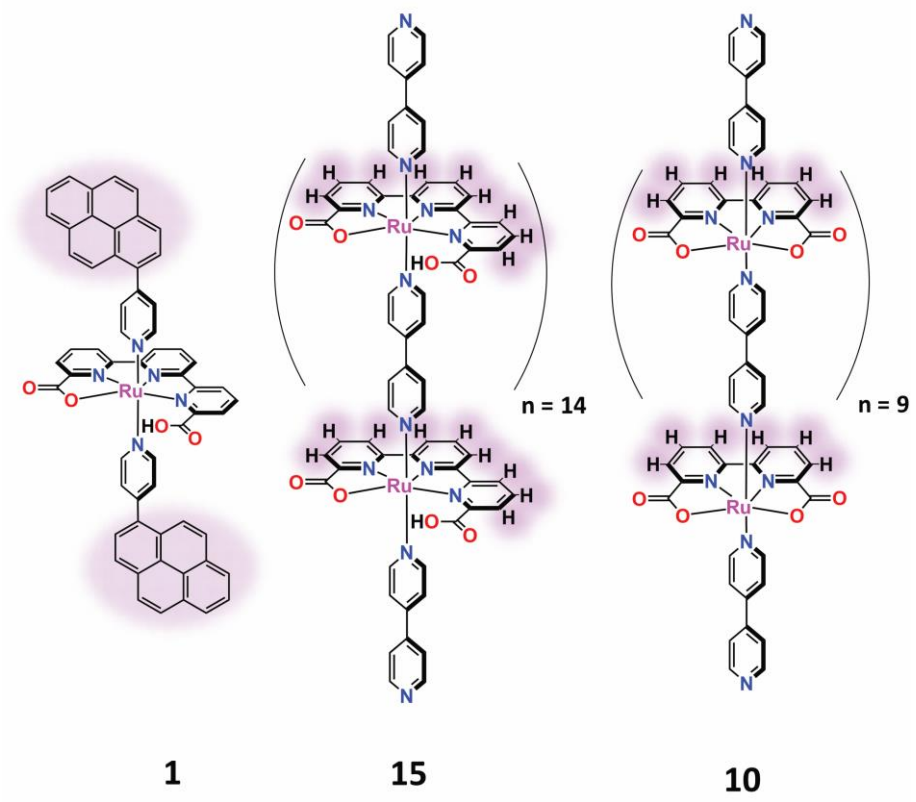

Figure 3.1: Representation of the different pre-catalysts used in Paper II. On the left the pre-catalyst for 1−H_2O@CNT@PE, in the middle for 15−H_2O@CNT@PE and on the right for 10−$(H_2O)_2$@CNT@PE. Adapted with permission from ACS Appl. Energy Mater. *2021, 4, 10, 10534-10541. Copyright 2021 American Chemical Society.*

The violet clouds highlight the proposed location of interaction between the catalyst and the MWCNT, which are omitted in the figure for clarity. Those pre-catalysts anchored on MWCNT where simply drop casted onto the printed electrodes. To drive catalysis, the catalysts had to be activated in which they coordinated one aquo/hydroxo ligand (or two for the Ru(bda)-based catalyst). For this purpose, the Ru(tda)-based catalysts were exposed to bulk electrolysis at pH 12, in which a hydroxo was coordinated to a position liberated by a carboxylate.[49] In contrast, the Ru(bda)-based catalyst was simply activated by several cyclic voltammetry sweeps in a pH 7 phosphate buffer. Here is was proposed that two aquo ligands coordinate to positions previously occupied by a pyrindine ring with attached

carboxylate.[54] For all molecular catalysts used in Paper II the coordination of the aquo ligand(s) and thus the activation of the catalysts can be followed by a shift of the ruthenium redox peaks to lower potentials in CV or differential pulse voltammetry (DPV).[52,54,109]

The activation of the Ru(tda)-based monomeric catalyst was for unknown reasons not successful on electrodes printed on a Nafion® substrate. Hence, PE printed on a high impact polystyrene substrate were used instead in Paper II for those molecular anodes. The resulting active molecular anodes were abbreviated as 1−H_2O@CNT@PE for the monomeric Ru(tda) complex, 15−H_2O@CNT@PE for the oligomeric Ru(tda) complex and 10−$(H_2O)_2$@CNT@PE for the oligomeric Ru(bda) complex. To be able to conduct the activation step directly in the electrolyte used for the experiment is a clear advantage for the latter since every rinsing step might provoke the loose of weakly adsorbed material from the surface of the electrode.

The loss of ruthenium centres from the electrode was visible during the long-time exposure for example for 15−H_2O@CNT@PE in Paper II. However, here it has to be differentiated: Either the catalyst was removed from the MWCNTs, which remain on the electrode, or the catalysts stayed on the MWCNT and the MWCNT with catalyst detached from the electrode. The former indicates a weak adsorption of the catalyst on the MWCNT whereas the latter suggests a weak adsorption of the MWCNTs on the electrode. As presented in Paper II, for 15−H_2O@CNT@PE both a decrease in double layer capacitance and surface loading of ruthenium can be observed during the stepwise chronopotentiometry (CP). This was rationalized with the loss of MWCNTs decorated with catalyst from the electrode surface, rather than the loss of catalyst from the MWCNTs and advocates for a strong adhesion of the catalyst onto the MWCNTs. Stirring of the solution as well as oxygen bubble formation during the reaction can be expected to have contributed to this removal. However, due to the unchanged maximum current density in the CVs it can be assumed that catalysis was overall limited by the electron conductivity of the PE and not the amount of catalyst on the electrode. Here I hypothesize two possibilities: Either the electrical resistances to the (later lost) ruthenium centres were from the very beginning too high to let them contribute to the catalytic current, or the overall supply of electrons

from the PE was too low to let all ruthenium centres participate at the same time. Nevertheless, in both cases the low conductivity of the PE is indicated to be the limiting factor.

Besides 15−H_2O@CNT@PE also 10−$(H_2O)_2$@CNT@PE showed an extremely stable performance and high activity during the 12 hours of OER as shown in Figure 3.2. Oligomeric catalysts did not only introduce an enhanced anchoring strategy, but simultaneously also increased the catalyst loading on the electrode, which led to an improved performance compared to the monomeric complex.

The surface loading of catalyst was calculated based on the charge consumed during the reduction of the ruthenium centre, visible in the CVs. Due to the overlapping of the peaks, the gaussian peak shape mode of the potentiostat's software (CHI 660C) was used for the analysis. In retrospective, this might have led to a slight underestimation of the surface loading. However, since the peaks merged, no other mode would have been applicable. In addition, the same conditions were used for calculating the surface loading at all times, so it is anticipated that the surface loading over time and the

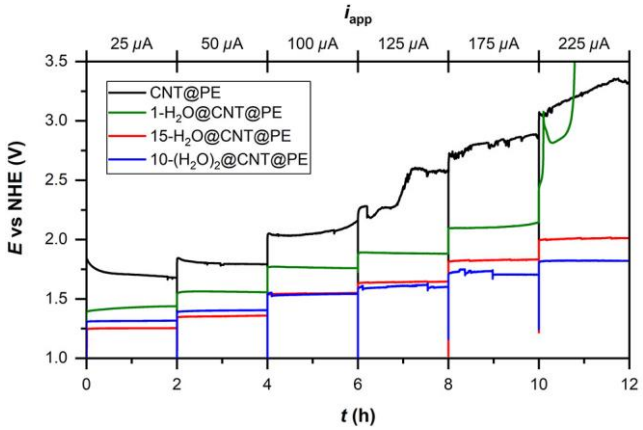

Figure 3.2: Stepwise CP of the different catalysts in pH 7. Each current was applied for two hours. CVs in between were used to determine the surface loading and the stability of the catalysts. The oligomeric catalysts 15-H_2O@CNT@PE and 10-$(H_2O)_2$@CNT@PE illustrated high activity and stability during the entire 12 h period. Reprinted with permission from ACS Appl. Energy Mater. *2021, 4, 10, 10534-10541. Copyright 2021 American Chemical Society.*

comparison of surface loading among the catalysts would not be affected by a possible minor deviation.

The greatest limitation of the molecular anodes was proposed to be the low and unreproducible electron conductivity of the PEs as detected by the ohmic resistance compensation routine of the potentiostat. It is assumed that this hampered the activity of the catalysts significantly, since the well reported TOF_{max} could not be reached. Furthermore, higher potentials had to be applied to reach the desired current, which might have caused the degradation of the electrodes, especially for 1−H_2O@CNT@PE. From the work in Paper II it became obvious, that the oligomeric catalysts were superior in their activity and stability, due to a larger number of active centres and the multiple CH−π interactions with the MWCTN, and hence would be more suitable to be implemented into a water splitting device. To confirm the PEs being the limiting factor, a reference experiment was conducted with a commercial carbon-based gas diffusion layer (GDL) as electrode.

In Figure 3.3 **(A)** the comparison between 15-H_2O@CNT on PE in red and on GDL in black, respectively, is illustrated. To exhibit a similar ohmic drop, the CV of the catalyst on PE taken from Paper II was fully *i*R compensated (*i*R ≈ 2815 Ω), whereas the CV of the same catalyst on GDL only to 85 % (*i*R ≈ 9 Ω). The influence of the electrode on the performance of the catalyst is clearly observable with 15-H_2O@CNT on GDL reaching catalytic currents nearly 25 × higher than on PE. The influence of the electrode becomes even more pronounced when considering the amount of catalyst on both electrodes. With the analysis of the charge consumed in the Ru^{IV}/Ru^{III} and Ru^{III}/Ru^{II} reductions (visible the inset in **(A)**), the catalyst loading was quantified with 0.21 nmol for 15-H_2O@CNT@GDL to be significantly lower than the 1.78 nmol for 15-H_2O@CNT@PE. The lower loading for the former was anticipated, since it just served as a control experiment and only a little amount of catalyst was intended to be used. With foot of the wave analysis (FOWA)[96,110] at the onset of the catalytic wave (highlighted in turquoise in **(A)**), the maximum turnover frequency (TOF_{max}) of 15-H_2O@CNT@GDL was estimated in **(B)** to be in the order of 8 000 s^{-1}, which agrees with the previously reported maximum

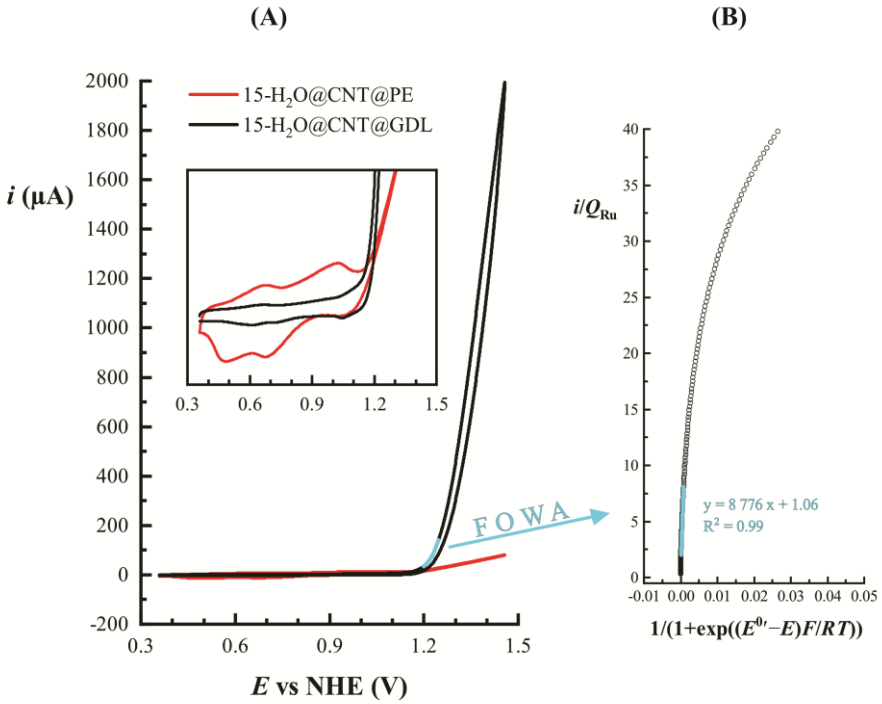

Figure 3.3: ***(A)*** *Comparison of the CVs of 15-H_2O@CNT on printed electrode and on GDL. Both were taken in 1.0 M phosphate buffer (pH 7) with a scan rate of 10 mV s^{-1}. Data on PE was taken from Paper II and fully iR compensated.*[109] *The CV of the catalyst on GDL was 85 % iR compensated. The inset shows the reversible redox waves of the ruthenium centres and the lower loading of catalyst on the GDL.* ***(B)*** *With FOWA the TOF_{max} of 15-H_2O@CNT@GDL was estimated as 8 776 s^{-1}.*

turnover frequencies of Ru(tda)-based catalysts.[49,52,53]

3.3 Promising to Integrate into an Electrolyzer Cell ?

When considering the possible integration into an electrolyzer cell, several aspects have to be considered:

1) Do we have a catalyst for the cathode working at the same pH?

2) Can the electrolyzer cell work at higher current densities?

3) Which parameters could possibly impose limitations?

In order to answer those questions, a search in literature is helpful. An advantage of the molecular catalyst used in Paper II is their ability to split water in neutral pH. However, this limits the number of known active and stable catalysts for the HER.[111] Nevertheless, cobaloximes are a famous family of cobalt-based molecular catalysts, which are reported to be active for HER in pH 7.[112–115] In addition, Yin's group presented a heterogeneous CoP/Co-MOF catalyst, which exhibits remarkable activity for HER in the same electrolyte as used in Paper II (1.0 M phosphate buffer, pH 7) and could be a possible choice in this hypothetical electrolyzer cell.[116] Another interesting strategy for the future might be to combine the Ru-MWOC at the anode with for example Fe−Fe hydrogenase inspired biocatalysts at the cathode.[117,118] From this point of view there are already known promising catalytic materials for the hydrogen evolution reaction in the desired condition.

This brings us to the next problem: High current densities. Electrolyzer cells usually operate in the range of several hundred mA cm^{-2}. The resistance of the PEs is a clear restriction at the moment, however, assuming those electrodes are made highly conductive or are exchanged with a more conductive electrode as a GDL, this would result in a decrease of resistance. Furthermore, in pH 7 a buffer is needed to (among others) further decrease the solution resistance. With the addition of buffer also the counterion (usually sodium or potassium) is added. It is unclear to which extent the cations will increase the overall resistance and limit the diffusion of protons through a proton exchange membrane, however cations are reported to lower the conductivity of the membrane significantly.[119] In general, compared to strongly acidic conditions, the neutral pH possesses a high resistance even with buffer, which significantly influences the potential necessary to reach high current densities. A too high applied potential might risk the degradation of a carbon-based anode or the Ru-MWOC. An additional strategy to reduce the overall resistance is to assemble the electrodes directly in contact with a membrane as Nafion® (zero gap configuration). This would clearly decrease the resistance but at the same time increase the local pH around the Ru-MWOC, which would now approximate the pH of the membrane. I could imagine this could lead to a decrease in activity, which

corresponds to a higher potential applied to reach the desired current density.[49,54]

Other limiting factors could be the upscalability. With a higher loading of catalyst, the potential to reach a desired current density could be decreased. However, the syntheses of Ru-MWOCs can be time and energy consuming and hence a high loading extremely challenging and not economically reasonable, especially in the case of an electrolyzer cell with several cm^2 electrode area.

3.4 ANCHORING STRATEGIES

Regarding the anchoring strategy, the CH−π interaction seems highly promising. The proposal of this interaction was corroborated in the reports characterizing the catalysts by scanning tunnelling microscopy (STM), atomic force microscopy (AFM), grazing incident wide angle X-ray scattering (GIWAXS), ^{1}H-NMR spectroscopy and density-functional theory (DFT) calculations.[52,54] Compared to π−π stacking, the adsorption of the catalyst *via* CH−π interactions onto the electrode seems to be enhanced, due to multiply anchoring points. Each equatorial ligand is proposed to contribute to the adsorption.[52,54] For the Ru(tda)-based and Ru(bda)-based oligomers this means a higher number of attractive interactions and hence a proposed higher stability as compared to the monomeric Ru(tda) complex.

Limited stability is also a drawback for other commonly used anchoring strategies as for example for the acidic-metal oxide interaction. Those acid-metal oxide bonds are known to be prone to hydrolysis, especially in low pH electrolytes, leading to a poor stability of molecular anodes.[60,120] An additional drawback is that the acidic groups of the equatorial ligand participating in the catalytic cycle as initial proton acceptors would be needed to be protected from anchoring on the surface, else the activity for OER would be drastically inhibited.[49,55] A more stable anchoring method would be *via* a covalent C−C bond between the catalyst and the carbon electrode by for example diazonium grafting.[108,121] However, this method is proposed to add challenges to the integration of the catalyst into current devices.[122] Additionally, in some cases it might result in a slight increase of the charge transfer resistance between the electrode and the catalyst

compared to the non-covalent π−π stacking strategy.[60] My hypothesis is based on the assumption of a misaligned π-system between the graphitic electrode and the diazonium crafted ligand. However, I expect it to be highly dependent on the ligand used and hence would be needed to be discussed for each system separately.

A reduced electron transfer from the catalyst to the substrate is reported also in the case of heterogenizing by alkylchain alignment.[57] In this strategy the ligands of the catalyst are modified with long alkylchains, which are supposed to self-assemble with the alkyl chains reaching from the electrode surface.[57,58] The strength of interaction between the chains can be expected to rise with longer aliphatic chain lengths. Unfortunately, with increasing length the charge transfer resistance from the catalyst to the substrate increases simultaneously.[57]

Another strategy to heterogenized molecular catalysts is to integrate them into a MOF. So far, even after overcoming difficulties in synthesizing the desired MOF with Ru(tda)-based molecular catalysts as linkers, the activation of the catalyst seemed to be not fully accessible until now.[55,123]

Last but not least in this short comparison of anchoring strategies, electropolymerization of molecular catalysts with suitable axial ligands is an interesting strategy to anchor the catalyst and provide high loadings. Sadly, also here there are obstacles, which still have to be overcome, as for example the instability of the catalytic film on the electrode.[56,124,125]

3.5 OUTLOOK

For an improvement of the printed molecular anodes, the conductivity of the PEs has to be clearly increased. Furthermore, since the electrodes are expected to have a graphitic surface, the anchoring of the catalyst could be done directly on the electrode. It is uncertain how much the loading of catalyst would decrease due to the reduced available surface area by excluding the MWCNTs. Luckily, as shown in Paper II, the surface (and hence surface area) of the PEs can already be altered by the ink composition. Additionally, besides the tda and bda

equatorial ligands, there is a huge variety of others ligands reported in literature for Ru-MWOC, among others with phosphonic or sulfonic groups.[48,51,126,127] Up to now, there are to the best of my knowledge no reports on oligomeric catalysts with those equatorial ligands. However, finding a strategy to successfully synthesize and subsequently characterize them seems only to be a matter of time. As a last remark, aside from the linear oligomers with 4,4'-bipyridine as axial ligand, also other ligands were successfully used to synthesize oligomeric compounds.[128,129] In the near future, the combination of promising equatorial ligands with novel axial ligands might result in new benchmarking molecular catalysts with regards to activity and stability.

KEY FINDINGS OF MY WORK

- **Oligomeric catalysts seem more suitable for the integration into an electrolyzer cell.**
- **The conductivity of the electrode has an essential influence on the performance of the catalyst.**

4 SINGLE ATOM CATALYST FOR THE HYDROGEN EVOLUTION REACTION (PAPER III AND PATENT I)

In this chapter, the work on the single atom catalysts presented in Paper III is discussed. Subsequently, the integration into a device is in focus, which involves a short introduction of Patent I. With a catalyst operating in acidic media as well as being deposited on a gas diffusion layer, this setup could be readily integrated into a proton exchange membrane electrolyzer cell (PEMEC) and hence is quite close to an already established device.

4.1 INTRODUCTION

The idea of single atom catalysts (SACs) is, as described in the introduction, to utilize all metal atoms in the material as active centres. By embedding those atoms into a highly conductive matrix, a fast electron transport to the active site should be provided. There are several different strategies reported on the synthesis of such a catalyst, among others the carbonization of a zeolitic imidazolate framework (ZIF).[65,66,130] ZIF-8 is known to exhibit a highly porous structure, providing a large surface area and hence illustrates a promising candidate as parent structure for SACs. In this ZIF, zinc ions are linked by 2-MeIm (2-MeIm is 2-methylimidazole) in a three-dimensional network. The fundamental idea in Paper III is to substitute some of the zinc nodes by a desired transition metal, followed by pyrolysis of the doped structure. In this step the organic linkers decompose into graphitic carbon and possibly reduce the metal ions, while zinc evaporates, leaving behind only the doping metal in the highly porous and conductive carbon matrix.[130]

There are different possibilities to introduce the doping metal into the ZIF-8, among others with a post synthetical metal exchange.[131,132] However, we decided to not only integrate the transition metal directly into the material during the ZIF formation, but also to avoid the use of solvents during the whole SAC synthesis, neither in the synthesis of the ZIF structure, nor in a purification or acid leaching step. Hence, this synthesis protocol presents clear benefits in terms of industrial

upscaling and waste management.[133,134] Luckily, Liu *et al.*, already reported a solvent-free synthesis of Fe-SAC for the oxygen reduction reaction, which served us as blueprint.[134]

The deposition of the SAC onto the electrode was conducted as for the state-of-the-art Pt/C catalyst, which enabled the usage of already known and established techniques. In short, the SAC powder was mixed with a Nafion® binder (a perfluorinated polymeric acid) and solvents to form a homogeneous catalytic ink, which was subsequently drop casted onto a carbon-based gas diffusion layer (GDL) as electrode with a volume equal to a SAC material mass loading of 0.5 mg cm^{-2}. In this way, the catalyst is basically glued with Nafion® directly onto the electrode.

4.2 Electrochemical Performance of SACs for HER

In Paper III the catalytic activities for HER of four transition metal SACs were investigated in strong acidic media (0.5 M sulfuric acid). Based on X-ray photoelectron spectroscopy (XPS) and powder X-ray diffraction (PXRD), all doping metals, manganese, iron, cobalt and nickel, seemed to have been successfully integrated into the porous N-doped carbon matrix, without the formation of a significant number or size of nanoparticles. In fact, only with transmission electron microscopy (TEM) and the connected energy dispersive X-ray spectroscopy (EDX) technique, few nanoparticles were observed for the investigated Co-SAC.

Among all tested materials, Co-SAC showed the highest performance and a good stability for the HER in strong acidic media, already with a very low loading as illustrated in Figure 4.1. The initial decrease in performance observed in chronopotentiometry (CP) was attributed to the leaching of small nanoparticles, which were observed in the as-synthesized material by TEM (Figure 4.1 **(A)**). Since the performance drop seemed to have happened only in the beginning of the measurement, it was hypothesized that the SACs likely have a higher stability compared to the nanoparticles containing the same element. As mentioned in Paper III, for a continuous leaching of the SAC metal, a continuous drop in performance would have been expected, which was not observed.

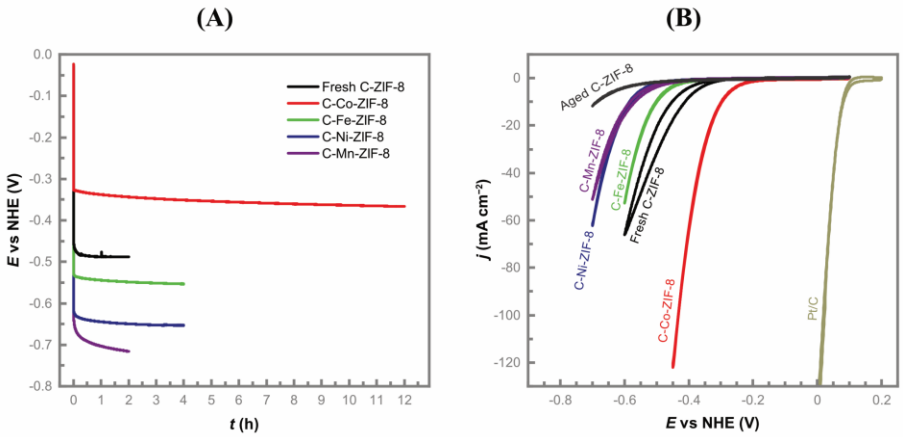

Figure 4.1: ***(A)*** *Chronopotentiometric measurement at −10 mA cm^{-2} in 0.5 M sulfuric acid for the different SACs with a mass loading of 0.5 mg cm^{-2}. Co-SAC illustrated the highest activity and a stable behaviour, indicating the enhanced stability of SACs.* ***(B)*** *CV of the different SACs with 10 mV s^{-1}, showing the highest performance for Co-SAC. Adapted from Paper III.*

I would like to mention that the undoped carbonized ZIF-8 structure already illustrated a highly interesting feature in the cyclic voltammogram (CV) shown in Figure 4.1 **(B)**, which was shortly described in Paper III. The fresh ink showed a reproducible crossing of the forward and reverse scan. This indicated an activation process happening on the forward scan, because of which the reverse scan illustrated a higher activity. An overall activation process would result in different performances of subsequent cycles, which was not visible in this case. It seems the activation of the forward scan got deactivated on the reverse, leading to the material being in the same conditions at the beginning and end of each scan. Unfortunately, the origin of this behaviour was not detected and after aging of the ink for one day, the phenomenon as well as the catalytic activity vanished for the undoped SAC. The decrease in activity with aging of the ink is hypothesized to be due to the agglomeration of particles to reduce the high surface energy of the material. This indicates the need for constant stirring and controlling of the ink.

4.3 MEMBRANE ELECTRODE ASSEMBLY

In order to integrate catalysts into a PEMEC, a subsequent step necessary to the deposition of the catalyst onto the electrode, is the assembling of the electrode(s) with a proton exchange membrane (PEM). This assembling process leads to a so-called membrane electrode assembly (MEA), which is referred to as the heart of an electrochemical cell. Inspired by a proton exchange membrane fuel cell, with this step, not only three components are combined to one, which facilitates the cell assembling, but also the performance is increased.[14,135] In general, a closer distance between the anode and cathode is expected to decrease the cell resistance.[14,136]

Up to now there are commonly two different MEA fabrication methods established. The catalyst can either be deposited onto the membrane (catalyst coated membrane (CCM)), or onto the electrode (catalyst coated substrate (CCS)).[137,138] In both of them the electrodes and the Nafion® membrane are assembled by hot-pressing after the catalyst deposition step.[137] The hot-pressing step is commonly conducted at temperatures in the range of 120 °C – 140 °C, which is above the glass transition temperature of Nafion®.[139,140] The membrane is suggested to become more malleable at these temperatures, leading to an improved interfacial connection of the electrodes with the membrane. It becomes obvious that the entire process is heavily depending on Nafion®, or any other membrane material with a glass transition temperature in this range.

Fortunately (for me), the provided sulfonated polyaryletherketone PEM seemed to not have a glass transition in this temperature range. In fact, only a small irreversible transition was detected at 245 °C by differential scanning calorimetry (DSC). Thus, assembling a MEA comprising this membrane material in a hot-pressing step was not successful and prompted the development of the process described in Patent I.

The basic idea of the process is to deposit the catalyst ink onto the electrode and solidify the mixture by freezing. The solidification step is necessary, because the membrane starts to swell, roll and bend immediately, when in contact with a liquid. With a solidified mixture,

this swelling can be prevented or slowed down significantly, facilitating the positioning of the electrode with the membrane. After the positioning, the setup is fixed with external weights and the ensemble is heated above the freezing temperature of the solidified mixture. In this way the mixtures liquifies, and causes the membrane to swell into the electrode and/or attacks the surface of the membrane, resulting in strong connection between the electrode and the membrane (see Figure 4.2). As described in Patent I, the MEA seems quite stable and even immersing in water, which is expected to cause the expansion of the membrane by swelling, is not leading to a detachment of the electrode from the membrane. In addition, different membrane materials and liquid mixtures were successfully tested for the assembling. The optimization of the process conditions for each mixture composition was unfortunately not possible in the time frame given, which was also a reason for the inability to characterize the so gained MEA electrochemically.

4.4 So, Using SAC in Electrolyzer Cells ?

With the employment of SACs in a MEA with the commonly used hot-pressing method with a Nafion® membrane, or possibly after fine tuning the process suggested in Patent I, a cell with a hopefully low resistance between anode and cathode could be obtained. With this

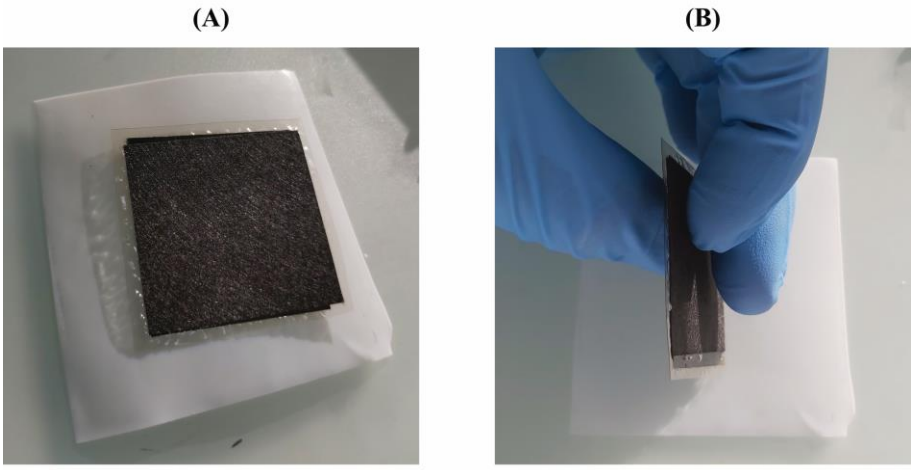

Figure 4.2: Pictures of a MEA manufactures according to the process described in Patent I. ***(A)*** *Top view and* ***(B)*** *side view.*

solution, one obstacle presented for the ruthenium-based molecular catalysts seem to be overcome. Could SAC be the solution we are hoping for?

An aspect, which has to be critically reviewed when considering the use of SACs in electrolyzer cells, is the mechanism for the hydrogen evolution reaction accessible with SACs. In Chapter 1.2.2 the widely accepted steps for HER were presented. In short, the Volmer step describes the adsorption of a hydrogen atom onto the surface, the Tafel step the recombination and desorption of two adsorbed hydrogen atoms on the surface in close proximity, and the Heyrovsky step the electrochemical desorption of an adsorbed hydrogen atom by the interaction with a proton in solution. Assuming the transition metal is the site of adsorption, it becomes clear that the Tafel mechanism is highly unlikely. For SACs the active sites are expected to be homogeneously dispersed in the material and hence too far away from each other to enable a recombination of two adsorbed hydrogens.[64] This means that the fastest mechanism proposed for the hydrogen evolution is impossible for SACs. In the best case these materials might follow the Volmer-Heyrovsky mechanism, which is proposed to only have a 10 mV dec^{-1} higher Tafel slope than the Volmer-Tafel mechanism and thus exhibits only slightly higher potentials at high current densities. As a quick approximation: Imagine that two materials have the same potential at 10 mA cm^{-2}, but follow the two different mechanisms. At a current density of 1 A cm^{-2} the material following Volmer-Heyrovsky would only have a 20 mV more negative potential than the one following Volmer-Tafel. However, it should be noted that due to their similarity with molecular catalyst, SAC might follow a molecular pathway and hence the designation of the adsorbing site is uncertain.[141–143] The assumption of SACs being similar to molecular catalysts with an undefined ligand is corroborated by high-resolution XPS analysis of the metal, revealing all metal sites being oxidized and not in a metallic state. It seems with SACs the lines between molecular systems and nanoparticles start to blur, which makes the classification and description of mechanisms complicated.

Nevertheless, assuming the applicability of Tafel slope analysis, the potential required to reach the next decade of current density is often assumed to only depend on the mechanism of the rate determining

step (Volmer, Tafel or Heyrovsky). Tilak *et al*. suggested that this assumption might not be true.[64,144] In their work they proposed that the surface loading of catalyst indeed has an influence on the Tafel slope with a decrease in surface loading leading to an increase in the slope. This might explain the deviation in the Tafel slope to higher values than the proposed 30 mV dec^{-1}, 40 mV dec^{-1} or 120 mV dec^{-1} for the Tafel-, Heyrovsky- or Volmer-step, respectively, as detected in other SACs publications.[63,64,67] Thus, low numbers of active sites might result in a higher potential necessary to operate the electrolyzer cell at a desired current density and the need to increase the number of active sites seems unavoidable.

Another issue needed to be considered is the anode compartment. When driving HER in strong acidic media and using a proton exchange membrane (PEM) as separator between the two half-cells, obviously also the anodic reaction will be driven in the same electrolyte. The acidity of the medium does not only impose a major limitation on the materials used for the current collectors, casings and other components of the whole electrolyzer cell, but also on the material used as catalyst for the anodic reaction. Up to now, iridium and ruthenium oxides are the most active catalyst known for the OER in acidic media. Both are rare metals and even though they suffer from dissolution at high potentials, other solid state catalysts are significantly less stable.[19,20,145] Hence, active and stable OER catalysts based on earth abundant materials are highly needed. The group of Nørskov proposed based on density-functional theory (DFT) calculations possible promising catalysts, of which some were already successfully synthesized and reported.[26,146]

A solution to avoid high material costs and rare and noble metals as catalysts for the anodic side would be to exchange the PEM with an anion exchange membrane (AEM) or a porous separator and run electrolysis in alkaline media.[15] In these conditions many transition metals and oxides are known to be stable and highly active for OER.[18,25,69] Unfortunately, HER in alkaline media is reported to by sluggish. Some transition metals, as those used in Paper III, are proposed to adsorb hydroxides on the surface, which might hamper the HER reaction.[43,147,148] Furthermore, water is used as proton source, which requires water dissociation during the Volmer and Heyrovsky

step. Thus, this step is suggested to be rate limiting.[43] The proposed oxophilicity of the transition metals leading to the hydroxide adsorption mentioned above, is suggested to promote the water dissociation step of neighboring sites and hence to accelerate the HER in alkaline conditions.[43,147] Unfortunately, as for the Tafel step, in SACs materials the metal sites are likely too far away from each other to act in such a beneficial way.

4.5 OUTLOOK

An obvious disadvantage, which prevents the SACs of Paper III from being implemented into a device is its low loading of active sites. As an example, in Paper III the Co-SAC electrode had a mass loading of 0.5 mg cm^{-2}, of which only approximately 1.3 wt.% was cobalt. The low loading could be raised in two different strategies. Either increasing the mass loading on the electrode for a given SAC material, or increasing the intrinsic metal loading of such a SAC material. The former approach might lead to the burying of already existing active sites under inactive material by for example repetitive drop casting. Thus, the drop casting process would be needed to be optimized as well as the ink formulation. The second approach could be realized by increasing the amount of doping metal in the ZIF-8 synthesis. Unfortunately, this is expected to simultaneously lead to a more likely formation of nanoparticles. Thus, the synthesis parameters might need to be adjusted to decrease or supress the nanoparticle formation. However, as described in the previous chapter on ruthenium-based molecular water oxidation catalysts and also above with regard to the Tafel slope, a higher loading of active sites on the electrode is essential for an increased electrocatalytic performance.

With the solvent-free synthesis of SACs, this process might spark interest for industrial production. However, when thinking about scaling up the synthesis process of such SACs, the high temperature required for the pyrolysis and the evolved gasses during the decomposition of the ZIF structure might present a drawback.[149]

A component which was not discussed so far, but might have a significant influence on the electrochemical performance is the GDL. Those electrodes exist in different configurations, which can include an

additional microporous layer or PTFE treatment of the GDL to increase the hydrophobicity of the material. Since the aqueous electrolyte provides the reagent, it is uncertain how much the hydrophobicity of the electrode influences the electrochemical activity. However, Nafion® was used as binder in the ink and could compensate or counteract this property of the electrode. Nevertheless, it should be noted that besides the hypothesized influence on the catalytic behaviour, the hydrophobicity had an apparent effect on the ink deposition process. Drop casting in a previous experiment on an electrode without a microporous layer and PTFE treatment led to the ink running through the electrode with effectively less material being deposited on the electrode and highlights the benefit of such a microporous layer and hydrophobicity. In conclusion, the GDL with PTFE treatment or additional microporous layer, its integration into the device, the ink additives and overall composition as well as the deposition method have all to be adjusted to each other, in order to obtain the best performing electrode.

KEY FINDINGS OF MY WORK

- **Co-SAC is the most promising catalyst for HER in acidic media.**
- **SACs have higher stability than nanoparticles of the same element.**
- **MEAs can be fabricated in a novel way, which is independent on the glass transition temperature of the membrane.**

5 NANOPARTICLE CATALYSTS BASED ON NICKEL MOLYBDATE HYDRATES FOR THE OER AND HER (PAPER I AND PAPER IV)

After the previous chapters revealing that a low number of active sites might not be desirable for an electrolyzer cell operating at higher current densities, this chapter covers the exploration of nickel molybdate hydrate-based nanoparticles as electrocatalyst for both the oxygen evolution reaction (OER) and hydrogen evolution reaction (HER). For this, Paper I and Paper IV lay the foundation for the discussion. In the following, Paper I focusses on the behaviour of the material in the electrolyte and during OER, while Paper IV targets the fundamental characterization of the two detected nanostructures.

5.1 INTRODUCTION

Due to the discussed challenges facing water electrolysis in neutral or strongly acidic pH, the alkaline region of the pH scale is here in focus. Alkaline electrolyzer cells (AEC) are exhibiting already a mature technology and with transition metals and their oxides being stable in basic conditions a clear advantage in terms of range of applicable materials. Among the tested transition metals and transition metal oxides, nickel molybdenum alloys and nickel iron layered double hydroxides (NiFe-LDH) present outstanding electrocatalytic activities for HER and OER, respectively.[18,24,73,78,79,81,150,151] Both are nickel-based compounds and can be synthesized from a nickel molybdate hydrate precursor, which is reported to appear in two different nanostructures, namely nanorod and nanosheets as illustrated in Figure 5.1.[82,152–154] Besides the benchmarking catalysts synthesized from nickel molybdates, there are additional motivations to investigate those materials. First, both, nickel and molybdenum are already used in AEC, which highlights the industrial interest in and viability of those elements. Second, in contrast to noble metals mentioned as oxygen evolution catalysts in Chapter 3 and Chapter 4, both, nickel and molybdenum were not listed as critical raw materials by the European Union in 2017.[155]

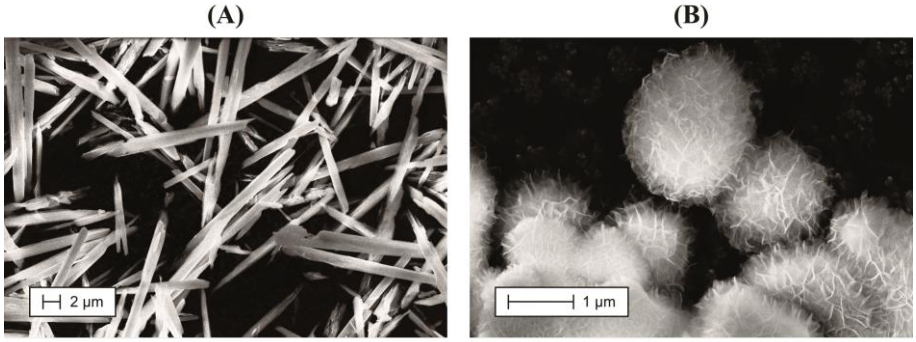

Figure 5.1: Scanning electron microscopy (SEM) images of the different nickel molybdate hydrate nanostructures. ***(A)*** *Nanorods.* ***(B)*** *Nanosheets. Adapted from Paper IV with brightness and contrast adjusted for better visibility.*

A further benefit is that those nickel molybdate hydrate-based nanostructures can be synthesized directly onto the electrode in for example a hydrothermal synthesis as shown in Paper I, neglecting the need for an anchoring strategy or deposition process of the catalyst onto the electrode. Usually, the hydrates are synthesized in the time span of a few hours in a temperature range of usually 150 °C – 200 °C.[78,81,152–154,156–159] Especially with a subsequent annealing step in a reducing hydrogen-containing atmosphere, this material has been shown to exhibit high catalytic activities especially for HER, but also OER.[78,157–160] However, there are still uncertainties in literature regarding the origin of the high activity and the active site[78,157–159,161] as well as for the fundamental characterization of the hydrate precursor.[82,162,163]

The access to *operando* Raman spectroscopy fuelled the idea behind Paper I to elucidate the role of the different elements in $NiMoO_4 \cdot nH_2O$ for electrocatalytic OER. With this knowledge, the influence of further synthetical steps as annealing or reducing, and even the improvement of the performance by substituting certain elements should have been targeted in subsequent steps. However, due to the outcome of Paper I that the different nanostructures are likely different compounds and can appear in the same synthesis, the focus was shifted to first characterize the two nanostructures fully, before continuing the investigation and their improvement as electrocatalysts.

5.2 Selective Molybdenum Leaching in Alkaline Media

In order to investigate the role of the different elements of a catalyst and the nature of their enhancing effect on the catalytic activity, *in situ*, *operando* or post-catalysis measurements are imperative.

One of the most important results of this thesis resulted from an observation with such a technique. With time-resolved *in situ* Raman spectroscopy the instantaneous molybdenum leaching from the nickel molybdate hydrate rods was detected in Paper I. Already without applied bias the vibrations assigned to the Mo−O modes vanished over the time span of a few minutes in the 1 M KOH electrolyte (Figure 5.2). In contrast to the rod structure, the spectrum of the nickel molybdate hydrate sheet structure with its assigned Mo−O vibrations remained unaltered and suggested a superior stability in terms of molybdenum retainment in 1 M KOH.

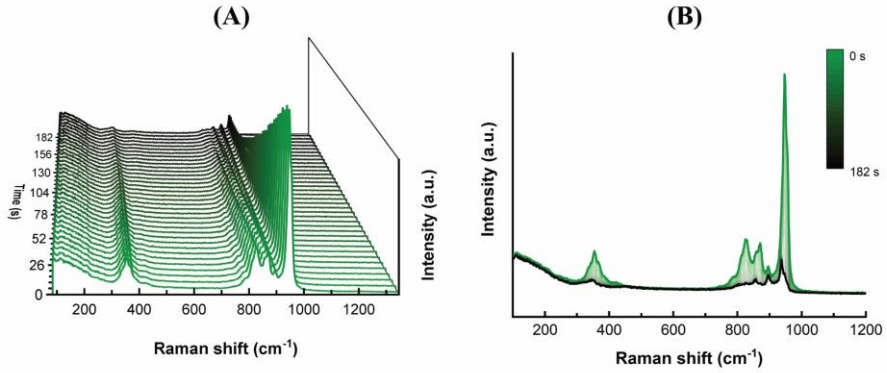

Figure 5.2: In situ Raman spectroscopy of hydrate nanorods and nanosheets on a nickel foam in 1 M KOH. The nanorod vibrations in green vanish over the time frame of three minutes. Only the vibrations of the nanosheets in the very back in panel (A) and in black in panel (B) remained. ***(A)*** *Illustrates the change in the Raman spectra in a three-dimensional plot for a better observation of the change over time.* ***(B)*** *Illustrates the same data in a two-dimensional plot for an improved identification of the Raman shifts. Adapted from ACS Nano 2021, 15, 8, 13504 – 13515. Copyright 2021 The Authors. Published by American Chemical Society and licensed under CC BY 4.0.*

The leaching of molybdenum from the rods and the assignment of the different Raman spectra and X-ray diffraction (XRD) patterns to the nanostructures was confirmed by energy dispersive X-ray spectroscopy (EDX) mapping and inductively coupled plasma optical emission line spectrometry (ICP-OES). At this point it is still unclear, in which form molybdenum was leaching out from the rods *in situ* and from the sheets at sufficiently high applied potentials, as will be discussed below. It might have leached out already as a molybdate or possibly formed a molybdate in solution. However, as in Paper I, this process is further denoted here as molybdenum leaching.

Selective molybdenum leaching (or etching) from the nanorod structure provided not only the possibility to unambiguously attribute the different Raman vibrations to the nanostructures (Figure 5.3), but also presents a strategy to probe the presence of nanosheets in a synthesis with nanorods, as shown in Paper IV.[82] In retrospective, besides the assignment of the different Raman spectra and XRD patterns to the corresponding nanostructures, also the selective molybdenum leaching step represents an accomplishment of this thesis work with a possible great impact in the future. As described below and in Chapter 5.4 in more detail, this technique illustrates a strategy to probe the actual present nanostructures on the electrode and hence might help to elucidate or confirm the assignment of the activity to the nanostructures or active sites. Additionally, this technique might be also applicable for other compounds with similar pore forming agents and hence could be also used for other catalysts directly deposited on electrodes.

As reported in Paper I, after removal of the molybdenum from the nanorods and hence turn them "Raman invisible", Raman bands from the sheet structure were detected on a sample with initially no sheets observed by SEM. Only after mechanical removal of the rods by extensive ultrasonication, sheet structures were detected between the rods and the foam as shown in SI Figure 12 in Paper I and Figure 5.4 below and hence explains the appearance of the signal in *in situ* Raman spectroscopy.[82]

This is important since we were not the only one detecting the sheet signal on a foam with only rods assumed.[80,81] Choi and co-workers as

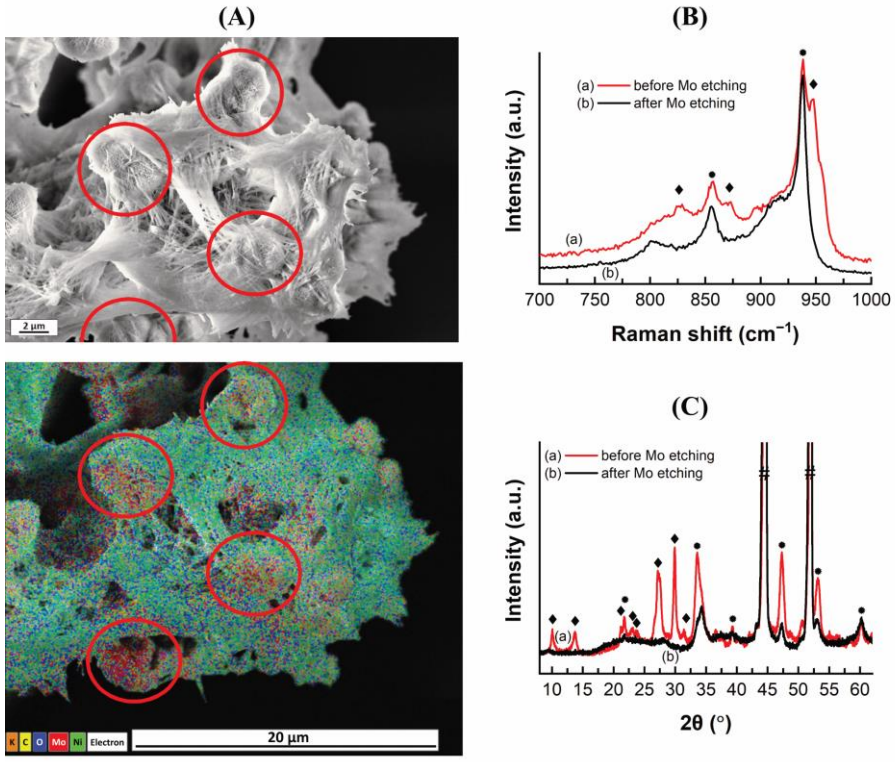

Figure 5.3: Investigation of the mixed nanostructure after selective molybdenum leaching. ***(A)*** *SEM image of mixed structures and the EDX mapping of the different elements below. Molybdenum (red colour) was only found in the nanosheets (red circles).* ***(B)*** *Raman spectra before and after leaching/ etching, verifying the removal of the vibrations of the nanorods.* ***(C)*** *XRD pattern before and after molybdenum leaching/ etching. Adapted from ACS Nano 2021, 15, 8, 13504 – 13515. Copyright 2021 The Authors. Published by American Chemical Society and licensed under CC BY 4.0.*

well as Liu and co-workers reported the synthesis of nickel molybdate hydrate nanorods on a nickel foam. With *in situ* Raman spectroscopy both detected the appearance of –to them– unknown Raman vibrations. Instead of relating them to the hydrate sheets, both wrongly assigned the new bands to a change of the initial vibrational environment of the rods or to the dissolution of molybdenum oxide.[80,81] The repetitive observations of nanosheet signals in syntheses, which proposed only nanorods on nickel foam, strengthens my following hypothesis: In most publications reporting only nanorods

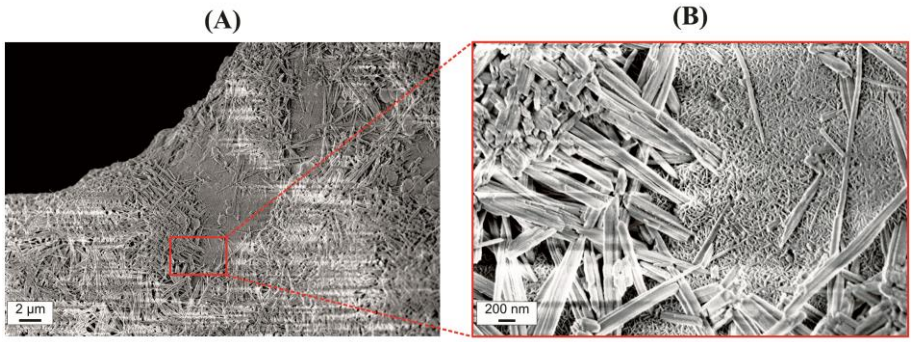

*Figure 5.4: Detection of nanosheet structures by SEM between the nanorods and the foam with different resolutions for **(A)** and **(B)**. Adapted from ACS Nano 2021, 15, 8, 13504 – 13515. Copyright 2021 The Authors. Published by American Chemical Society and licensed under CC BY 4.0. Brightness and contrast were adjusted for better visibility.*

on nickel foam there is likely an undetected layer of nickel molybdate hydrate sheets below the rod structure, especially when a similar synthesis protocol as ours was followed.

The detection of all present nanostructures is vital, since nickel molybdate hydrates are only precursors for the final catalyst. The assumption of solely one structure might lead to an incorrect assignment of the activity, as will be discussed below in Chapter 5.4, especially since the two nanostructures are detected to be different compounds, as presented in Chapter 5.5, and hence the present phases during catalysis on the foam might be fundamentally different.

But first, the stability and the effect of anodic potentials on the hydrate nanostructures will be discussed.

5.3 Origin of High Activity of Nickel Molybdate Hydrates for OER

With cyclic voltammetry the activity of the nickel molybdate hydrate nanostructures towards OER was investigated in Paper I. In subsequent cycles the increase of charge consumed during the Ni^{II} to Ni^{III} oxidation peak was observed, indicating more nickel sites becoming exposed to

the electrolyte with time. In addition, a large increase in double layer capacitance of the electrode was detected, which is assumed to be proportional to the electrochemical surface area (ECSA). Both trends could be rationalized with the formation of a highly porous structure by removal of molybdenum, which was confirmed by ICP-OES of the electrolyte, by *in situ* Raman spectroscopy of the electrode and post-catalysis analysis of the nanostructures by EDX and X-ray photoelectron spectroscopy (XPS). With molybdenum leaching the nickel surface loading raised by 20 – 30 times, quantifying the increase on nickel sites exposed to the electrolyte. This led to overpotentials of less than 600 mV for a current density of 200 mA cm^{-2}, normalized to the geometric electrode area and without *i*R compensation, and a quite stable behaviour over 500 cycles (Figure 5.5). However, it should be noted that the actual current density is strongly influenced by the thickness and porosity of the metal foam. This has to be taken into account when comparing activities among publications using porous electrodes.[100]

Based on the amount of visible nanosheets assembled to nanoflower structures by SEM and the intensity of the corresponding Raman bands in the *ex situ* Raman spectra of the as-synthesized materials, the

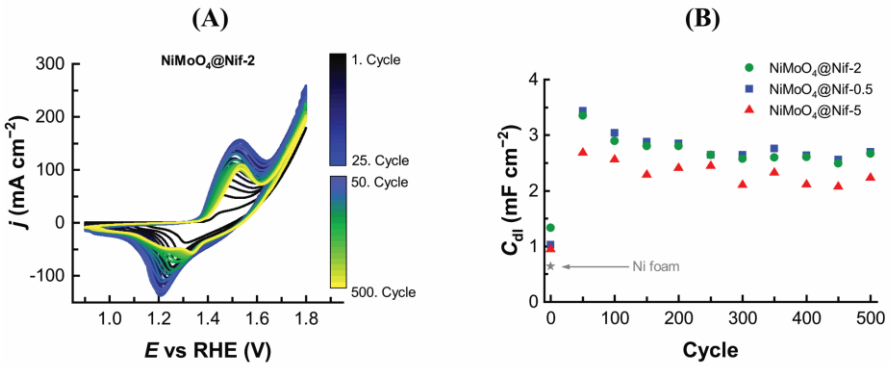

Figure 5.5: Electrochemical analysis of the nickel molybdate hydrate decorated nickel foams. ***(A)*** *Cyclic voltammogram (CV) in 1 M KOH with 10 mV* s^{-1}. ***(B)*** *The double layer capacitance (*C_{dl}*) over the 500 cycles indicate a stable high electrochemical surface area. Adapted from* ACS Nano *2021, 15, 8, 13504 – 13515. Copyright 2021 The Authors. Published by American Chemical Society and licensed under CC BY 4.0.*

different catalytic performances were assigned to the nanostructures. It was proposed that the nanorods are more active than the sheets. In retrospective, this attribution might be difficult, since the contribution of the nanosheet structures between the nanorods and the foam remains unknown. For a more valuable comparison, both nanostructures would have to be synthesized separately and characterized for example on a glassy carbon electrode.

The ability to investigate the electrodes spectroelectrochemically did not only detect the sudden molybdenum leaching process from the nanosheets upon the Ni^{II} to Ni^{III} oxidation, but also enabled the detection of the active phase during water oxidation. During the oxidation of Ni^{II} to Ni^{III}, the Raman bands of the nanosheet vanished while the Raman spectra of γ-NiOOH emerged, which was also the only phase detected during catalysis (Figure 5.6). Hence, the data indicated that in fact for both nanostructures nickel molybdate hydrate is only the precursor, which turned into γ-NiOOH as the active phase for OER. This was also observed by Choi *et al.* and Liu *et al.*.[80,81] The latter work detected with extensive transmission electron microscopy (TEM)

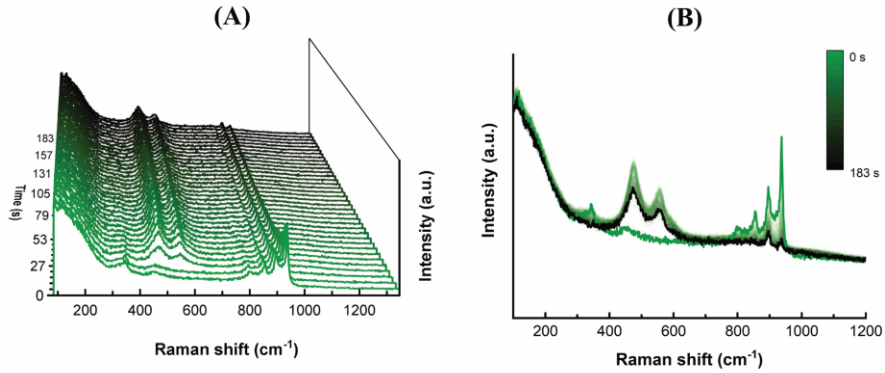

Figure 5.6: Molybdenum leaching from nanosheets and formation of γ-NiOOH observed by in situ *Raman spectroscopy at 1.4 V vs RHE in 1 M KOH.* ***(A)*** *Illustrates the change in the Raman spectra in a three-dimensional plot for a better observation of the change over time.* ***(B)*** *Illustrates the same data in a two-dimensional plot for an improved identification of the Raman shifts. Adapted from* ACS Nano *2021, 15, 8, 13504 – 13515. Copyright 2021 The Authors. Published by American Chemical Society and licensed under CC BY 4.0.*

tomography the phase transformation step by step, and did not only confirm the presence of γ-NiOOH in the nanorod structure, but also an influence of the temporal separation of the molybdenum leaching and nickel oxidation step on the final γ-NiOOH morphology. Subsequent leaching and oxidation responded in the formation of γ-NiOOH nanosheets, whereas a simultaneously leaching and oxidation resulted in smaller nanoparticles with enhanced OER activity.[80] This observation explains the roughened surface with a sheet like structures of the rods, detected by SEM post-catalysis in SI Figure 26 in Paper I and Figure 5.7 here.[164]

The conclusion of Paper I regarding the role of molybdenum was that it initially acts as a structure forming agent during the synthesis, followed by being a pore forming agent *in situ* and during the Ni^{II} to Ni^{III} oxidation. Since it was not present anymore in the structure during catalysis, electronic effects were excluded and the enhanced OER activity was proposed to only derive from the high number of active sites, as also suggested for other transition metal molybdates or compounds with other pore forming agents as in nickel iron diselenide.[72,73]

Nickel molybdenum-based compounds are also reported to be excellent hydrogen evolution catalyst, making this material highly interesting for both half-cell reactions.[18]

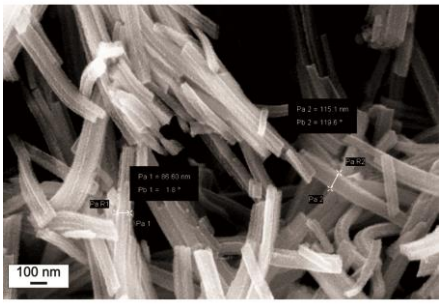

Figure 5.7: SEM image of the roughened nanorod surface after catalysis. Adapted from ACS Nano *2021, 15, 8, 13504 – 13515. Copyright 2021 The Authors. Published by American Chemical Society and licensed under CC BY 4.0. Brightness and contrast were adjusted for better visibility*

5.4 HYDRATE *VERSUS* ANHYDRATE SHEETS FOR HER

In order to achieve high catalytic activity for HER, the nickel molybdate hydrate nanostructures are usually annealed in a reducing hydrogen-containing atmosphere.[78,157–159,161] Independent on the nanostructure, the active site and high activity of the reduced nickel molybdate compounds were previously assigned to $MoNi_4$ formed in this process.[78,157,159] Worth mentioning is that there is some disagreement in literature about the stability and nature of the contribution of molybdenum to the HER activity for $MoNi_4$.[78,161]

However, with this annealing step, the *in situ* molybdenum leaching of the rods is inhibited and the presence of sheets on an electrode with annealed or reduced rods cannot be probed by selective molybdenum leaching in combination with Raman spectroscopy anymore. Instead, one would need to investigate the foam – rods interface by for example SEM. Based on a proposal from Paper I, it is uncertain, if the nanorod structure can be exclusively synthesized on nickel foam without the formation of nanosheets. Since the reduced nanosheet structure has also been reported to reach high activity for HER,[157] their contribution to the overall HER activity might be overseen, which is often solely (and maybe falsely) attributed to the reduced rod structure.[78,159] The unambiguous assignment of the activity to the nanostructure is essential for further developing and tailoring the catalyst.

The aim behind this project was to take a step back and first compare the hydrate nickel molybdate with the anhydrate nickel molybdate towards HER in alkaline media. The sheet structure was selected because of several reasons. First, Paper I suggested that a synthesis of only nanorods on a nickel foam would be uncertain whereas from experience the exclusive synthesis of sheets seemed accessible. Second, molybdenum was proposed to have a beneficial influence on the HER activity. In contrast to the rods, the nanosheets have been detected to retain molybdenum in their structure in alkaline media, if not oxidized, and hence presented the more interesting hydrate structure for HER. In addition, TEM analysis of the sheet structures in Paper IV has revealed very small crystalline regions in the sheets of the hydrate, whereas the anhydrate nanosheets consisted of larger

crystalline areas with possible nickel rich precipitates. It was hypothesized that the larger crystals might facilitate the electron transport while the precipitates could act as active sites, which might lead to a higher activity.

Here it should be noted that the annealing step was conducted under air and not in a reducing atmosphere. Therefore, no extremely high HER activities were expected. Nevertheless, with growing the hydrate sheets onto the nickel foam an increase in activity was observed (Figure 5.8). However, the enhancement is only minor and additional experiments are required for a deeper understanding of the material and further improvement of the catalyst. In stark contrast to the hydrate sheets, with the subsequent annealing step the HER activity was surprisingly completely hampered.

The most straight forward interpretation would be that the annealed sheets are simply not catalytic active. In addition, the annealing step might have caused a partial delamination of the nanostructure from the foam, as observed around cracks in the nanostructure layer by SEM. This might not only increase the charge transfer resistance from the foam to the catalyst layer, but might actually make some nickel sites on the anhydrated sheets electrically inaccessible and hence

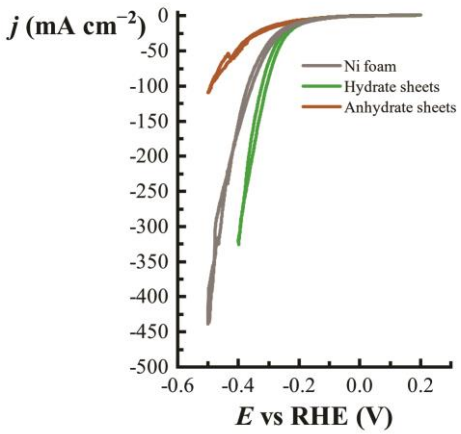

Figure 5.8: CV of the nickel foam electrode (grey), decorated with nickel molybdate hydrate sheets (green) and after annealing to form the nickel molybdate anhydrate sheets (brown). CVs taken in 1 M KOH with 10 mV s^{-1} and 90 % iR *compensation.*

additionally decrease the available number of active sites.

From the electrochemical experiment it was suggested that the hydrate and anhydrate have fundamental different activities. Hence, they should be clearly denoted as either hydrate or anhydrate in scientific reports. However, since the anhydrate sample suffered from cracks, it might not be representative for all anhydrate samples in literature and other synthesis parameters have to be explored before making a final statement. Second, the reduction step is clearly essential to establish high catalytic activities. Nevertheless, first the synthesis and annealing parameters have to be improved, since it is doubtable that the addition of hydrogen in the annealing process would prevent crack formation or delamination.

A possibility to avoid crack formation due to annealing could be to avoid this step completely and instead deposit and reduce the material electrochemically. Thus, in order to synthesize the desired sheet or rod nanostructure *via* electrodeposition, it should be helpful to have the structures fully characterized first. This might lead to a deeper understanding of the materials and hence to the development of suitable electrodeposition conditions for the two nanostructures.

5.5 Different Nanostructures are Different Materials

As suggested in Paper I, the different hydrate nanostructures exhibit not only different Raman spectra, but also different chemical stabilities, crystal structures and elemental compositions. Thus, it becomes obvious that the sheets and rods are not just two different nanostructures of the same material, but two fundamentally different materials. Hence, the distinction between the two materials seems important and should be implemented in the scientific community.

The motivation behind Paper IV was to first fully characterize the different nickel molybdate hydrate nanostructure compounds to gain a deeper understanding of the materials and their synthesis conditions, before returning to their electrochemical application. After synthesizing the isolated hydrate nanostructures successfully, as shown above in Figure 5.1, they could already be distinguished by bare eye. The nanorods exhibited a yellow colour, whereas the nanosheets

had a bright green colour.

With traditional TEM in bright field mode and with selected area electron diffraction, large monocrystalline rods were detected for the hydrate rod structure. Since there are some discrepancies between the XRD and electron diffraction pattern and the reported crystal structure for nickel molybdate hydrate ICDD: 04-017-0338,[162] three-dimensional electron diffraction was employed to propose together with powder XRD a new crystal structure. At the moment of writing this thesis, this refinement is still ongoing.

In stark contrast to the rods, the extremely thin sheets (< 1.9 nm thickness) seemed to consist of small crystalline and amorphous regions, explaining the weak diffraction intensity in XRD. Based on the similarity of the morphology and the XRD pattern to nickel hydroxide sheets, and the reported possible intercalation of vanadate anions in between nickel hydroxide sheets, it seems plausible that the nanosheet compound could have a layered crystal structure with molybdate either intercalated or as part of the layers.[83,165–168]

The difference in elemental composition as proposed by Paper I, was confirmed by EDX, XPS and ion beam analysis (IBA) techniques. For the latter, time-of-flight elastic recoil detection analysis (ToF-ERDA) and Rutherford backscattering spectrometry (RBS) were combined to detect the elemental bulk composition of Ni, Mo, O and H. With thermogravimetric analysis (TGA) the amount of crystal water was subsequently proposed, suggesting a stoichiometry of approximately $NiMoO_4 \cdot 0.6\ H_2O$ for the hydrate nanorod and $Ni_3MoO_5 \cdot 2.3\ H_2O$ for the hydrate nanosheet material.

In order to achieve charge neutrality under the assumption of oxygen in oxidation state −II, nickel and molybdenum in the nanorods would need to be in +II and +VI, respectively, which was indicated by high resolution XPS and zero field cooled and field cooled (ZFC-FC) measurements. However, for the nanosheet compound high resolution XPS proposed the presence of a mixed valence molybdenum in +V and +VI state (Figure 5.9 **(A)**). This would require nickel to be also in a mixed valence with oxidation states +I and +II, which still has to be confirmed by ZFC-FC.

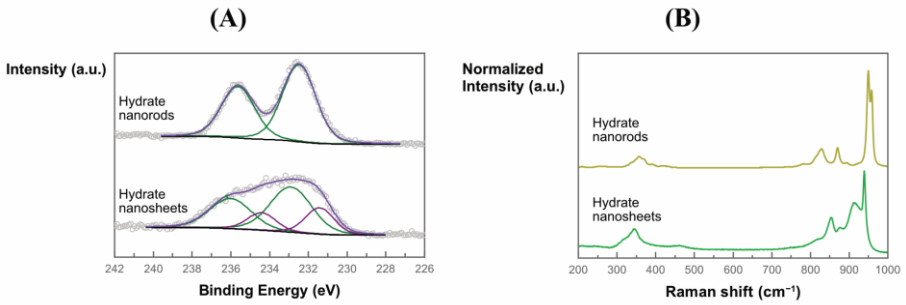

Figure 5.9: ***(A)*** *Molybdenum 3d high resolution XPS spectra of the different hydrate nanostructures showing a mixed valence for the nanosheets. Green fit corresponds to* Mo^{6+} *and purple fit to* Mo^{5+}. ***(B)*** Ex situ *Raman spectra of the different nanostructures confirm the assignment proposed in Paper I.*

With Raman spectroscopy the proposed Raman bands for the nanostructures by Paper I were confirmed (Figure 5.9 **(B)**). In contrast to the suggestion of Paper I that the different wavenumbers for the symmetric Mo−O stretching originates from a possible polymolybdate formation in the rods and monomolybdate in the sheet structure, it now seems more likely that in both nanostructures a monomolybdate could be present. The different Raman shifts might be explained by the assumption of the molybdate anion being surrounded by NiO_6 octahedrons in the rods, while in the sheets the molybdate anion might be integrated in/between $Ni(OH)_2$ sheets. A polymolybdate formation for the rods seems discarded, due to an equimolar nickel to molybdenum ratio as suggested by Paper IV. The superior chemical stability in 1 M KOH of the sheet compound over the rod compound was corroborated by selective molybdenum leaching.

As mentioned in the previous chapter, this leaching process offers an important strategy to confirm the presence of one or the other isolated nanostructure: the molybdenum leaching of the nanorods makes this material Raman invisible, while the stable sheets retain their spectra. Hence, molybdenum leaching in combination with Raman spectroscopy can be employed to suggest the isolated synthesis of rods without the sheet structure. On the other hand, the XRD pattern and the Raman bands of the nanorods are so intense, that nanorods in a synthesis of nanosheets can be expected to be detected by those

techniques. I propose to employ this strategy in future work on nickel molybdate hydrate-based catalysts, especially when directly grown on the electrode. As indicated in Paper I and Paper IV, when probing a mixed material, the high intensity XRD pattern and high intensity Raman bands of the rod compound might cover the signal of the sheets and hence might falsely suggest only rods to be present.

The analysis of the different hydrate nanostructures revealed that in fact those are two fundamentally different materials and should be reported like that. The hydrate nanorod structure is the commonly referred to nickel molybdate hydrate ($NiMoO_4 \cdot 0.6\ H_2O$), whereas the nanosheet structure is likely a layered nickel (hydroxide) molybdate structure ($Ni_3MoO_5 \cdot 2.3\ H_2O$). Furthermore, both nickel and molybdenum are proposed to be present in mixed valence oxidation states in the hydrate sheets, which illustrates an additional clear difference to the rod compound.

It seems unlikely that with annealing or reducing two fundamentally different compounds transform into the same material. Thus, anhydrated or reduced compounds originating from the hydrate nanorod or hydrate nanosheet structures can be expected to present differences. As proposed by Paper IV, the hydrate nanorod compound transforms during an annealing step in air to α-$NiMoO_4$, whereas the hydrate nanosheets transforms in a mixed structure of α-$NiMoO_4$ and likely small nickel rich precipitates. XPS analysis furthermore suggest molybdenum still being present in a mixed valence state for the sheet structure, which could have an effect on the catalytic activity.[158]

5.6 Will Nickel Molybdate Hydrate-Based Nanoparticle Catalysts be the Future?

As suggested by literature, nickel molybdate hydrate as precursor can lead to extremely active oxygen evolution catalysts and hydrogen evolution catalysts with Faradaic efficiencies close to 100 %.[157,159] With the ability to directly grow them on the electrode in a fast and facile synthesis, this material seems to be highly promising as pre-catalyst for future electrolyzer cells.

When discussing its suitability in an actual device, the actual emerging catalysts have to be considered. For the OER, γ-NiOOH is the actual active phase, as highlighted in Paper I and several other recent studies.[80–82] Iron doping illustrates a known straight forward strategy to increase the intrinsic activity significantly and most probably will be the catalyst used in such a device.[81,156] As indicated by the work of Diaz-Morales *et al.*, nickel oxyhydroxide needs to be deprotonated to be active and hence only operates at high pH values.[169] In highly alkaline regimes, usually porous separator are used in the mature alkaline electrolyzer cells (AEC) to separate the anodic from the cathodic compartment. Besides possible gas crossover, also an increased solution resistance imposes limitations on such a cell. Especially the latter is tried to be compensated by increasing the KOH concentration.[14,16,170]

As for a device in neutral pH, also in alkaline pH resistance management is pivotal for a cell running at high current densities. Due to the usage of highly porous and three-dimensional metal foams as electrodes, a high catalyst loading per geometric area and hence the possibility to reach high current densities can be achieved. However, an increased foam thickness could simultaneously lead to an increased solution resistance, which is not desired.

A strategy to decrease the resistance between the electrodes is adopted from the proton exchange membrane electrolyzer cell (PEMEC). By substituting the porous separator with an anion exchange membrane (AEM) not only the cell resistance could be reduced, but also the gas purity could be increased. Unfortunately, some AEM suffer from instability issues and this device architecture is not mature yet.[15,170,171] Additional complications might rise from the desired molybdenum leaching step of the rod or sheet structure of the nickel molybdate hydrate-based catalysts for OER. Since AEM shuttle anions, the presence of molybdate anions in solution might affect the hydroxide conductivity of the AEM negatively, similar to the decrease of proton conductivity in PEMs by other cations (as discussed in Chapter 3.3). To prevent this, either the molybdenum leaching would have to be carried out before the integration of the electrode into the cell, or the electrolyte would have to be renewed after the formation of the catalyst. Undesired additional anions in the electrolyte might not

only originate from the intended molybdenum leaching process for the oxygen evolution catalyst (OEC). It could also be due to molybdenum leaching of the $MoNi_4$ hydrogen evolution catalyst (HEC) during operation or of another NiMo-based material at open circuit potential.[161,172]

For the integration into a device, the stability of the catalysts plays a major role. Since the conditions applied in the laboratory are not the same as in an industrial electrolyzer cell, the stability of the catalyst also under these conditions have to be analysed. For example, Liu *et al*. proposed that their α-$NiMoO_4$ rod catalyst would be stable in 1 M KOH at 20 °C, but suffers from molybdenum leaching at temperatures above approximately 50 °C.[173] In industrial electrolyzer cells the temperature is usually elevated to 50 – 80 °C and the electrolyte has a KOH concentration of around 6 M, which is significantly higher concentrated than in usual lab experiments.[14,16] Hence, it is unclear if the stability of catalytic materials suggested under laboratory conditions represents their stability in an industrial setup. However, if the desired performance of the cell is already reached at laboratory conditions, there is no pressing need for higher electrolyte concentrations or temperatures.

Besides altering the electrode to obtain a high surface area by default, also the versatility of nanostructures and synthesis methods enable high surface areas and a high number of exposed active sites on the electrode. However, metal oxides are generally poor electron conductors and a too thick catalyst layers or too sprawling nanostructures might not be beneficial for catalysis. Hence, an efficient strategy proposed is to synthesize a core-nanostructure with increased conductivity, on which a thin layer of catalyst is deposited.[158,159,174] In addition, for increasing the activity by nanostructuring, Seh *et al*. have proposed the existence of an upper limit.[25] At some point charge and mass transport are expected to impose limitations on the overall activity.

The importance of resistance management in alkaline media was recently demonstrated by Hodges and Hoang *et al*..[24] By among others decreasing the solution resistance between anode and cathode as well as avoiding bubble formation on the electrodes, they reached

remarkable activities with an energy efficiency of 93 % for a current density of 1 A cm^{-2} at 85 °C. Based on the successful resistance management illustrated in the mentioned work, high current densities could indeed be achievable for anion exchange membrane electrolyzer cells operating in alkaline conditions. Since highly active OEC as nickel iron layered double hydroxide used in this publication, could possibly be synthesized from a nickel molybdate hydrate-based precursor,[81,157,158] and $MoNi_4$ HEC synthesized from a nickel molybdate hydrate precursor reached electrocatalytic activities similar to platinum,[78,157–159] I believe nickel molybdate hydrates are promising precursors for catalysts in future water splitting devices.

With operating in alkaline conditions, not only earth abundant elements can be used as OEC and HEC, but also the whole cell could avoid the employment of expensive components required for a device using acidic media. This might lower capital costs of these electrolyzer cells and could offer the widespread use, which is imperative for a transition to a circular energy society.[15,17]

5.7 Outlook

The full characterization of the different nanostructure materials is still ongoing and essential to elucidate the most suitable nickel molybdate hydrate-based compound for the different reactions. The crystal structures of the nickel molybdate hydrates are (so far) not fully resolved. A possible helpful characterization method could be X-ray absorption spectroscopy, which could give valuable inside among others on the coordination environment, but also the oxidation states of the elements and the interatomic distances.[175]

In general, first the two nanostructures should be electrochemically characterized independently. The fundamental difference between the hydrate rod and sheet compounds could play a major effect. It seems the sheet compound could provide more active nickel sites and also has an initial higher surface area compared to the rods. However, the rods contain more molybdate, so a more porous structure might be formed.

In a next step, in order to increase the activity of the hydrate structures towards OER, the integration of iron directly in the synthesis of the nickel molybdate hydrate nanostructures could be put in focus. An iron doped sheet structure was already successfully synthesized in a one-step hydrothermal process.[156] However, to the best of my knowledge, the iron doped version of the rod structure was only obtained with an anion exchange step subsequently to the synthesis of the rods. Hence the direct synthesis of an iron doped nickel molybdate hydrate rod structure still remains to be demonstrated.[81]

Since the reducing step is expected to inhibit the molybdenum leaching, this step might be undesired for OER. On the other hand, it might enable a faster electron transport and/or synergetic effects of molybdenum present during catalysis. Hence also the reduced nanostructures could illustrate improved, but different activities for OER. For HER the active site of the reduced nickel molybdate hydrates was proposed to be $MoNi_4$. This could lead to different activities of the two nanostructures, since it is a nickel rich precipitate (advantage sheet compound). However, a possibly simultaneously formed MoO_{3-x} core is suggested to enhance the electron transport to the active site and might contribute with synergetic effects (advantage rod compound).[158,159]

Once the desired nanostructure is synthesized on the electrode, the isolated synthesis should be verified. For proposed exclusive synthesis of the rod structure, this could be done by either selective molybdenum leaching in combination with Raman spectroscopy or XRD for the hydrate rod form, or by investigating the interfacial layer between the anhydrate rods and the foam. From my point of view, the verification of the presence of only one compound is vital for the correct assignment of the electrochemical activity and future developments of the catalysts.

The employment of different electrodes might offer the possibility to further optimize the cell performance and might be important for the transition into an industrial relevant device. While metal foams would be the electrode of choice for the anodic compartment, both, metal foams and carbon-based gas diffusion layers could be implemented on the cathodic side. Among others, electrode thickness and porosity

could have an influence on the electrochemical surface area, cell resistance and mass transport limitations. In addition, different electrodes might enable the isolated deposition of the desired structure, which should be confirmed by the methods mentioned above.

To further promote the large-scale implementation of the material, alternative synthesis routes of the catalyst or pre-catalyst might be of interest. With the hydrothermal synthesis utilized in Paper I and Paper IV, precipitation aside the electrode seems inevitable, hence electrodeposition might be a more suitable method to deposit catalyst only on the electrode. In addition, this process neither requires high temperatures, a reducing atmosphere nor several hours for the synthesis of the HEC and hence demonstrates some advantages regarding upscaling.[151,176–178] However, translating the synthesis of a known compound from the hydrothermal to an electrodeposition process might come along with some challenges.

Molybdenum leaching was detected with the subsequent formation of a higher surface area electrode, which was suggested to be the origin for high catalyst activities. With the reduction step, the nickel molybdate-based compound might lose the ability to do so. Luckily, besides molybdenum also other elements are reported to act as pore forming agent, for example selenium, aluminium or zinc.[73,74,79] Thus, with the addition of such an element mentioned above, the porosity and high surface area of the reduced compound might be able to be reintroduced.

Based on nickel molybdate hydrates, both, highly efficient and active catalysts for HER and OER can by synthesized, which seem to be very promising candidates for the integration into an alkaline electrolyzer cell, preferably with an anion exchange membrane. As indicated before, the long-term stability of $MoNi_4$ nanoparticles is still under discussion and would need to be resolved at industrially relevant conditions as temperature or electrolyte concentration, before a final recommendation can be made. Once the stability uncertainty is fully resolved and the most suitable nanostructure for the different reactions is detected, this Ni−Mo precursor system might be able to make a change and could be implemented in a widespread electrolyzer

cell.

KEY FINDINGS OF MY WORK

- **Both nickel molybdate hydrate nanostructures transform into highly porous γ−NiOOH for the OER.**
- **Molybdenum acts as structure and pore former.**
- **Nanorods and Nanosheets are different compounds.**
- **Selective molybdenum leaching enables the probing of nanosheets in nanorod synthesis.**

6 SUMMARY AND OUTLOOK

In this thesis work, different classes of catalysts and their suitability for integration into an electrolyzer cell have been investigated.

Ruthenium-based molecular catalysts in Paper II showed high activities and stabilities for water oxidation at neutral pH. Especially the oligomeric catalysts exhibited a superior performance. The electrical conductivity of the electrode was discovered as a limiting factor on the catalytic activity of such a molecular anode. In addition, the low loading of catalyst on the electrode and the low conductivity of the electrolyte at neutral pH, might impose further limitations to reach high current densities at reasonable potentials and hence illustrates a drawback for the widespread use of such an electrolyzer cell. Possibly, further development of molecular catalysts with different equatorial and axial ligands could give rise to even higher activities and might partially compensate the low loading. Additionally, to integrate those catalysts in a device, one might have to move away from the traditional device architectures and would have to develop a setup more suitable for this class of catalysts.

Among the tested transition metal single atom catalysts synthesized by pyrolyzing transition metal doped ZIF-8 structures in Paper III, cobalt showed the highest activity for hydrogen evolution and a stable behaviour in acidic pH. The enhanced stability of single atomic sites compared to the corresponding nanoparticles was proposed. Only a low number of nanoparticles was suggested to have been formed during the solvent free synthesis. Hence, this process might present an interesting strategy for the large-scale synthesis of single atom hydrogen evolution catalysts. However, also for this class of catalyst, the low number of active sites is a challenge to address. To increase the amount of catalyst sites, either the mass of catalytic material on the electrode could be increased or the percentage of active sites in the material. In addition, also the availability of only noble metal-based catalysts for the anodic site and higher material costs for a device operating in acidic pH risk to hamper the widespread use of such an electrolyzer cell.

With the novel method to fabricate a membrane electrode assembly presented in Patent I, the usage of expensive Nafion® membranes could possibly be avoided, which could reduce the cost of such a device. With this new process so far impractical membrane materials might be applicable. In addition, also new membranes could be developed with properties adjusted to this fabrication method. Such an approach could lead to membrane electrode assemblies with enhanced electrocatalytic performances. However, before this novel method might lead to a MEA in a device, process parameters as liquid mixture composition, heating time and temperature would have to be adjusted and optimized first.

Both of the as-prepared nickel molybdate hydrate nanoparticle shapes – sheets and rods – have been proposed in Paper I to transform in an electrochemical activation step into γ-NiOOH as active phase for the oxygen evolution reaction in alkaline pH. Due to the removal of molybdenum, either by immersing the rod structure in the electrolyte or by oxidizing the sheet structure from Ni^{II} to Ni^{III}, a high electrochemical surface area with a large number of exposed nickel sites was indicated to be the origin behind the high catalytic activity of the system. Molybdenum was suggested to only serve as structure and pore forming agent. In addition, the attribution of different XRD patterns and Raman bands to the two nanoparticle structures was confirmed by Paper IV. Even for the sample on nickel foam with only rods initially visible by electron microscopy, the signal of the compound in the sheet structure was observed after selective molybdenum leaching and could be traced back to the intermediate layer between the foam and the nanorods. Due to the presence of both nanostructures, it is difficult to assess the exact catalytic activities towards the oxygen evolution reaction to both compounds. However, preliminary results indicated a higher activity for the compound in the rod structure. The nanosheet layer between the rods and the foam might be an interesting observation for further work concerning nanorods on the electrode and the attribution of the catalytic activity. For an exact assignment, the different nanostructures should be isolated electrochemically characterized on for example a glassy carbon electrode. However, an essential outcome and proposal of Paper I was that when synthesizing a nickel molybdate rod structure

on an electrode, the absence of the sheet structure should be verified, which could be done by either selective molybdenum leaching combined with Raman spectroscopy or XRD, or by investigating the volume between rods and the electrode with SEM.

With Paper IV the fundamental differences between the nanostructures were characterized with various techniques, indicating strongly that those are two different compounds. The crystal structures of the two nanostructures are not fully resolved yet, but hopefully once refined will lead to a deeper understanding of the materials. Different stoichiometries were proposed with a mixed valence nickel and molybdenum for the sheet structure.

For the hydrogen evolution reaction in alkaline media, the hydrate sheet structure exhibited a higher activity compared to the anhydrate, but clearly a reduction step is necessary to access the outstanding catalytic activity reported.

Among all the investigated classes of catalysts, those inorganic nanostructured catalysts seem to be the most promising ones for a successful integration in a large scale electrolyzer cell for widespread use, especially, once the stability of the catalysts and the anion exchange membrane is resolved. However, nickel molybdate hydrate needs a reduction process to be highly active for HER and Fe doping should be considered for boosting the OER significantly. Besides tuning the catalyst, also different electrodes might be helpful to increase the activity of the device. For a large-scale implementation, the transition from a hydrothermal synthesis to electrodeposition might be worth considering.

For tackling climate change, the development and widespread use of electrolyzer cells, ultimately powered by renewable energies, is only one aspect. In order to counteract global warming, humankind has to reduce the greenhouse gas emission in general and live in a more sustainable way.

In addition, I strongly believe that we should not aim for only one electrolyzer device, but keep investigating and developing all kind of catalysts and systems. Similar to transportation nowadays, in which we

have different vehicles for different purposes, I envision we will have different devices and catalysts for different purposes in a circular energy society. Last but not least, carbon capturing and other electrochemical reactions as carbon dioxide reduction or nitrogen reduction are expected be vital process on our way in a more sustainable future.

7 RESUME

Ce travail porte sur la synthèse et la caractérisation de différentes classes de catalyseurs et de leur intégration comme électrodes de travail pour une cellule d'électrolyse.

Les électrodes à base de complexes moléculaires de ruthénium fabriquées par sérigraphie (Article 2) présentent des activités et des stabilités élevées, à pH neutre, vis-à-vis de l'oxydation de l'eau. Les catalyseurs sous forme d'oligomères montrent des performances supérieures. La conductivité électronique de l'électrode est le facteur limitant l'activité catalytique d'une telle anode moléculaire. De plus, le faible chargement en catalyseur sur l'électrode associé à la faible conductivité ionique de l'électrolyte à pH neutre imposent des limitations supplémentaires pour atteindre des densités de courant élevées à des potentiels raisonnables. Ce travail illustre donc les inconvénients majeurs pour une utilisation à grande échelle de telles électrodes dans une cellule d'électrolyse.

L'étude de matériaux catalytiques, composés d'un Métal de transition, d'Azote et de Carbone (Article 3) montre que celui contenant du cobalt a la plus grande activité pour la production d'hydrogène en milieu acide tout en montrant une certaine stabilité. Cette dernière s'explique par la présence de sites atomiques uniques, au détriment de la formation de nanoparticules, obtenus par une méthode de synthèse sans solvant. Ce procédé présente donc une stratégie intéressante pour la synthèse à grande échelle. Cependant, l'augmentation du nombre de site catalytiques dans le matériau reste une difficulté à surmonter.

Une méthode (Brevet I) de fabrication des assemblages membrane-électrode a aussi été mise en place. Elle permet le remplacement des membranes coûteuses couramment utilisées et la réduction du coût de fabrication des dispositifs d'électrolyse. Cette méthode devrait permettre aussi la mise en œuvre de différents polymères pour la fabrication de nouvelles membranes aux propriétés ajustées.

Deux structures de Molybdate de Nickel ont été synthétisées (Article

1) pour fabriquer, après électro-activation, des nanoparticules de γ-NiOOH actif envers la production d'oxygène en pH alcalin. L'élimination du molybdène, soit par immersion de la structure en bâtonnets dans l'électrolyte ou soit par oxydation du Ni^{2+} en Ni^{3+} de la structure en feuille, conduit à une surface électrochimique élevée avec un grand nombre de sites de nickel exposé et explique l'origine de l'activité catalytique élevée. La présence de Molybdène sert donc ici d'agent structurant et porogène. Les différences de structures de Molybdate de Nickel ont été mise en évidence par des analyses Raman. Grâce à ces attributions, il est possible de montrer que le dépôt en forme de bâtonnets (mis en évidence par microscopie électronique) fabriqué sur une mousse de Nickel comporte aussi le signal de la structure en feuille après l'éviction du molybdène. La présence de cette structure s'explique par une couche intermédiaire entre l'électrode en mousse et les bâtonnets visibles par microscopie électronique. En raison de la présence des deux nanostructures, il est donc difficile d'évaluer les activités catalytiques intrinsèques vis-à-vis de la réaction d'évolution de l'oxygène. Cependant, les résultats semblent indiquer une activité plus élevée pour la structure en bâtonnets. Un résultat essentiel de cette étude est que lors de la synthèse d'une structure en bâtonnets de Molybdate de Nickel sur une électrode, l'absence de la structure en feuille doit être vérifiée. Les différences fondamentales (Article 4) entre les nanostructures ont été caractérisées plus en détail à l'aide de diverses techniques : MEB, DRX et Spectroscopie Raman. Bien que les structures cristallines des deux nanostructures ne soient pas encore totalement résolues, les analyses montrent clairement qu'il s'agit de deux matériaux différents avec leurs propriétés. En effet la structure hydratée en feuille présente une activité supérieure à celle déshydratée pour la production d'hydrogène en milieu alcalin. Il est clair qu'une étape de réduction préliminaire est nécessaire pour accéder à l'activité catalytique exceptionnelle rapportée.

Parmi les différentes classes de catalyseurs étudiés, les catalyseurs à nanoparticules semblent être les plus prometteurs pour une intégration réussie dans une cellule d'électrolyse à grande échelle. L'utilisation généralisée de ce type de matériau pourra être envisagée une fois que la stabilité des catalyseurs et de la membrane échangeuse d'anions sera résolue.

8 POPULAR SCIENTIFIC SUMMARY

My doctoral journey experienced with the COVID-19 pandemic and the Russian invasion of Ukraine two earth shattering events. In both, the importance of collaborations between countries and continents to face global crises has been made visible. Especially in case of the COVID-19 pandemic, collaboration between scientists and institutions to provide a solution has been proven to be pivotal for the existence and future of humankind. One can only dream how fast such a focus and commitment of global governments and decision makers could resolve another existence threatening crisis: Global warming.

With the usage of fossil fuels in for example transportation or industry, carbon dioxide is emitted into the atmosphere. To this end, hydrogen presents a promising alternative to fossil fuels, which can not only be used in fuel cells to generate electricity, but is already employed as feedstock in important industrial processes as Haber-Bosch, Fischer-Tropsch or the production of green steel. Unfortunately, the vast majority of hydrogen (≈ 95%) is nowadays produced from natural gas with the simultaneous evolution of the greenhouse gas carbon dioxide in the process.[15]

To avoid the emission of carbon dioxide during the production of hydrogen and to generate it from renewable sources, water electrolysis presents a promising technique. With this approach electricity is used to generate hydrogen and oxygen from water by immersing two electrical conductors (electrodes) in an aqueous bath and apply an electric potential between them. The oxygen evolution is essential, since it provides the reagents necessary for hydrogen to evolve, but unfortunately is also more challenging than the hydrogen evolution reaction. In order to facilitate and accelerate both reactions (the hydrogen evolution at one electrode and the simultaneous oxygen evolution at the other) different so-called catalysts are needed.

Obviously, in order to make an impact on the global situation, first those electrodes and catalysts have to be integrated into a water electrolysis device. And second, a large-scale implementation of those devices should be reasonable, which means the materials used should

not be too expensive and should be stable for a long time under operation. For this purpose, experts on the different components of such a device would need to work together.

With the eSCALED project an attempt was made to realize exactly this. With 13 other fellow PhD students and 27 researchers in 11 institutions, universities and companies in 8 countries within Europe, and 3.6 Million Euro funding from the Horizon 2020 Marie-Skłodowska-Curie Actions Innovative Training Network, I spent the last four years trying to make an impact and contribute to future generations having a life without a planet on fire.

Focusing on the water electrolysis device, the aim of my PhD was not only to develop and characterize different types of catalysts, but also to examine their possible integration into a device. Following the order of the chapters in this thesis, the different types of catalysts can be described as highly efficient, but difficult to synthesize to less efficient but easy to synthesize.

In the here presented work I have investigated known ruthenium-based catalysts with two different anchoring strategies for the oxygen evolution reaction in neutral medium. The "catalysts chains" with more anchoring points have shown to not only be stable, but also to be more active compared to the isolated "single chain link" catalyst. It was concluded that the higher activity was due to the increased number of catalyst present. In addition, how good the electrode conducts electricity has shown to have a clear influence on the overall activity of the catalyst. For the integration of such a catalyst into a device a highly conductive electrode is necessary.

The subsequent chapter concerned catalyst with different single dispersed non-noble chemical elements for the hydrogen evolution reaction in strong acidic medium, in which cobalt was shown to be the most active one. Besides different activities for different elements, also the increased stability of single elements as catalysts compared to the corresponding nanoparticles was proposed. Furthermore, all catalysts were made without producing any solid or liquid waste, which presents an interesting strategy for synthesising them in large quantities.

In a related project I developed a novel way to glue the electrodes to a spacer. As mentioned above, during the oxygen evolution reaction at one electrode the necessary reagents for the hydrogen evolution are produced, which have to travel through the spacer to the other electrode. By gluing the electrodes onto the spacer this travel is accelerated. With the new method more spacer materials can be used than up to now.

In the last chapter I have shown the versatility of nickel molybdate hydrate nanostructures for both the hydrogen evolution reaction and oxygen evolution reaction in strong alkaline medium. I could show that two different shapes (nanorods and nanosheets) built up from the same elements are fundamentally different compounds. Not only was the ratio among the elements different, but also how they arranged and positioned themselves with respect to each other. Furthermore, I detected that for the oxygen evolution reaction both materials released molybdenum into the alkaline surrounding. With the removal of molybdenum, both materials transformed into a highly porous nickel compound with a sponge-like structure, at which the oxygen evolution reaction took place. With this observation I was able to explain why those materials were so active for the oxygen evolution reaction. Basically, previously covered nickel sites became accessible, which increased the number of catalytic sites present.

9 BIBLIOGRAPHY

(1) Information NOAA National Centers for Environmental. *Climate at a Glance: Global Time Series*. https://www.ncdc.noaa.gov/cag/ (accessed 2022-04-23).

(2) World Meteorological Organization (WMO). *WMO Atlas of Mortality and Economic Losses from Weather, Climate and Water Extremes (1970 - 2019)*; Geneva, 2021.

(3) European Commission, Directorate-General for Climate Action, *Going Climate-Neutral by 2050: A Strategic Long-Term Vision for a Prosperous, Modern, Competitive and Climate-Neutral EU Economy*; Publications Office, 2019. https://data.europa.eu/doi/10.2834/02074.

(4) Masson-Delmotte, V.; Zhai, P.; Pörtner, H.-O.; Roberts, D.; Skea, J.; Shukla, P. R.; Pirani, A.; Moufouma-Okia, W.; Péan, C.; Pidcock, R.; Connors, S.; Matthews, J. B. R.; Chen, Y.; Zhou, X.; Gomis, M. I.; Lonnoy, E.; Maycock, T.; Tignor, M.; Waterfield, T. IPCC, 2018: Summary for Policymakers. In: *Global Warming of 1.5°C An IPCC Special Report on the Impacts of Global Warming of 1.5°C above Pre-Industrial Levels and Related Global Greenhouse Gas Emission Pathways, in the Context of Strengthening the Global Response to the Threat of Climate Change, Sustainable Development, and Efforts to Eradicate Poverty*. In Press.

(5) World Health Organization; Convention on Biological Diversity. *Connecting Global Priorities: Biodiversity and Human Health: A State of Knowledge Review*; World Health Organization: Geneva, 2015.

(6) Grätzel, M. Recent Advances in Sensitized Mesoscopic Solar Cells. *Acc. Chem. Res.* **2009**, *42* (11), 1788–1798. https://doi.org/10.1021/ar900141y.

(7) British Petroleum Company. *Bp Statistical Review of World Energy 2021*; London, 2021.

(8) Khaselev, O.; Turner, J. A. A Monolithic Photovoltaic-Photoelectrochemical Device for Hydrogen Production via Water Splitting. *Science* **1998**, *280* (5362), 425–427. https://doi.org/10.1126/science.280.5362.425.

(9) Cheng, W.-H.; Richter, M. H.; May, M. M.; Ohlmann, J.; Lackner,

D.; Dimroth, F.; Hannappel, T.; Atwater, H. A.; Lewerenz, H.-J. Monolithic Photoelectrochemical Device for Direct Water Splitting with 19% Efficiency. *ACS Energy Lett.* **2018**, *3* (8), 1795–1800. https://doi.org/10.1021/acsenergylett.8b00920.

(10) Montoya, J. H.; Seitz, L. C.; Chakthranont, P.; Vojvodic, A.; Jaramillo, T. F.; Nørskov, J. K. Materials for Solar Fuels and Chemicals. *Nat. Mater.* **2017**, *16* (1), 70–81. https://doi.org/10.1038/nmat4778.

(11) Nishiyama, H.; Yamada, T.; Nakabayashi, M.; Maehara, Y.; Yamaguchi, M.; Kuromiya, Y.; Nagatsuma, Y.; Tokudome, H.; Akiyama, S.; Watanabe, T.; Narushima, R.; Okunaka, S.; Shibata, N.; Takata, T.; Hisatomi, T.; Domen, K. Photocatalytic Solar Hydrogen Production from Water on a 100-M2 Scale. *Nature* **2021**, *598* (7880), 304–307. https://doi.org/10.1038/s41586-021-03907-3.

(12) Jacobsson, T. J.; Fjällström, V.; Edoff, M.; Edvinsson, T. Sustainable Solar Hydrogen Production: From Photoelectrochemical Cells to PV-Electrolyzers and Back Again. *Energy Environ. Sci.* **2014**, *7* (7), 2056–2070. https://doi.org/10.1039/C4EE00754A.

(13) Ursúa, A.; Gandía, L. M.; Sanchis, P. Hydrogen Production from Water Electrolysis: Current Status and Future Trends. *Proc. IEEE* **2012**, *100* (2), 410–426. https://doi.org/10.1109/JPROC.2011.2156750.

(14) Schalenbach, M.; Zeradjanin, A. R.; Kasian, O.; Cherevko, S.; Mayrhofer, K. J. J. A Perspective on Low-Temperature Water Electrolysis - Challenges in Alkaline and Acidic Technology. *Int. J. Electrochem. Sci.* **2018**, *13* (2), 1173–1226. https://doi.org/10.20964/2018.02.26.

(15) Lagadec, M. F.; Grimaud, A. Water Electrolysers with Closed and Open Electrochemical Systems. *Nat. Mater.* **2020**, *19* (11), 1140–1150. https://doi.org/10.1038/s41563-020-0788-3.

(16) Schmidt, O.; Gambhir, A.; Staffell, I.; Hawkes, A.; Nelson, J.; Few, S. Future Cost and Performance of Water Electrolysis: An Expert Elicitation Study. *Int. J. Hydrog. Energy* **2017**, *42* (52), 30470–30492. https://doi.org/10.1016/j.ijhydene.2017.10.045.

(17) Li, D.; Park, E. J.; Zhu, W.; Shi, Q.; Zhou, Y.; Tian, H.; Lin, Y.; Serov, A.; Zulevi, B.; Baca, E. D.; Fujimoto, C.; Chung, H. T.; Kim, Y. S.

Highly Quaternized Polystyrene Ionomers for High Performance Anion Exchange Membrane Water Electrolysers. *Nat. Energy* **2020**, *5* (5), 378–385. https://doi.org/10.1038/s41560-020-0577-x.

(18) McCrory, C. C. L.; Jung, S.; Ferrer, I. M.; Chatman, S. M.; Peters, J. C.; Jaramillo, T. F. Benchmarking Hydrogen Evolving Reaction and Oxygen Evolving Reaction Electrocatalysts for Solar Water Splitting Devices. *J. Am. Chem. Soc.* **2015**, *137* (13), 4347–4357. https://doi.org/10.1021/ja510442p.

(19) Suen, N.-T.; Hung, S.-F.; Quan, Q.; Zhang, N.; Xu, Y.-J.; Chen, H. M. Electrocatalysis for the Oxygen Evolution Reaction: Recent Development and Future Perspectives Electrocatalysis for the Oxygen Evolution Reaction: Recent Development and Future Perspectives. *Chem. Soc. Rev.* **2017**, *46* (2), 337–365. https://doi.org/10.1039/c6cs00328a.

(20) B. Scott, S.; E. Sørensen, J.; R. Rao, R.; Moon, C.; Kibsgaard, J.; Shao-Horn, Y.; Chorkendorff, I. The Low Overpotential Regime of Acidic Water Oxidation Part II: Trends in Metal and Oxygen Stability Numbers. *Energy Environ. Sci.* **2022**, *15* (5), 1988–2001. https://doi.org/10.1039/D1EE03915F.

(21) Chen, L.; Dong, X.; Wang, Y.; Xia, Y. Separating Hydrogen and Oxygen Evolution in Alkaline Water Electrolysis Using Nickel Hydroxide. *Nat. Commun.* **2016**, *7*, 11741. https://doi.org/10.1038/ncomms11741.

(22) Park, J. E.; Kang, S. Y.; Oh, S.-H.; Kim, J. K.; Lim, M. S.; Ahn, C.-Y.; Cho, Y.-H.; Sung, Y.-E. High-Performance Anion-Exchange Membrane Water Electrolysis. *Electrochim. Acta* **2019**, *295*, 99–106. https://doi.org/10.1016/j.electacta.2018.10.143.

(23) Esposito, D. V. Membraneless Electrolyzers for Low-Cost Hydrogen Production in a Renewable Energy Future. *Joule* **2017**, *1* (4), 651–658. https://doi.org/10.1016/j.joule.2017.07.003.

(24) Hodges, A.; Linh Hoang, A.; Tsekouras, G.; Wagner, K.; Lee, C.-Y.; Swiegers, G. F.; Wallace, G. G. A High-Performance Capillary-Fed Electrolysis Cell Promises More Cost-Competitive Renewable Hydrogen. *Nat. Commun.* **2022**, *13*, 1304. https://doi.org/10.1038/s41467-022-28953-x.

(25) Seh, Z. W.; Kibsgaard, J.; Dickens, C. F.; Chorkendorff, I.; Nørskov,

J. K.; Jaramillo, T. F. Combining Theory and Experiment in Electrocatalysis: Insights into Materials Design. *Science* **2017**, *355* (6321), eaad4998. https://doi.org/10.1126/science.aad4998.

(26) Gunasooriya, G. T. K. K.; Nørskov, J. K. Analysis of Acid-Stable and Active Oxides for the Oxygen Evolution Reaction. *ACS Energy Lett.* **2020**, *5* (12), 3778–3787. https://doi.org/10.1021/acsenergylett.0c02030.

(27) Shaffer, D. W.; Xie, Y.; Concepcion, J. J. O–O Bond Formation in Ruthenium-Catalyzed Water Oxidation: Single-Site Nucleophilic Attack vs. O–O Radical Coupling. *Chem. Soc. Rev.* **2017**, *46* (20), 6170–6193. https://doi.org/10.1039/C7CS00542C.

(28) Ventosa, M.; Oliveras, J.; Bastús, N. G.; Gimbert-Suriñach, C.; Puntes, V.; Llobet, A. Nanocrystal−molecular Hybrids for the Photocatalytic Oxidation of Water. *ACS Appl. Energy Mater.* **2020**, *3* (10), 10008–10014. https://doi.org/10.1021/acsaem.0c01685.

(29) Lei, Q.; Wang, B.; Wang, P.; Liu, S. Hydrogen Generation with Acid/Alkaline Amphoteric Water Electrolysis. *J. Energy Chem* **2019**, *38*, 162–169. https://doi.org/10.1016/j.jechem.2018.12.022.

(30) Koper, M. T. M. Thermodynamic Theory of Multi-Electron Transfer Reactions: Implications for Electrocatalysis. *J. Electroanal. Chem.* **2011**, *660* (2), 254–260. https://doi.org/10.1016/j.jelechem.2010.10.004.

(31) Man, I. C.; Su, H. Y.; Calle-Vallejo, F.; Hansen, H. A.; Martínez, J. I.; Inoglu, N. G.; Kitchin, J.; Jaramillo, T. F.; Nørskov, J. K.; Rossmeisl, J. Universality in Oxygen Evolution Electrocatalysis on Oxide Surfaces. *ChemCatChem* **2011**, *3* (7), 1159–1165. https://doi.org/10.1002/cctc.201000397.

(32) Nocera, D. G. The Artificial Leaf. *Acc. Chem. Res.* **2012**, *45* (5), 767–776. https://doi.org/10.1021/ar2003013.

(33) Xiao, H.; Shin, H.; Goddard III, W. A. Synergy between Fe and Ni in the Optimal Performance of (Ni,Fe)OOH Catalysts for the Oxygen Evolution Reaction. *Proc. Natl. Acad. Sci. U. S. A.* **2018**, *115* (23), 5872–5877. https://doi.org/10.1073/pnas.1722034115.

(34) Doyle, R. L.; Lyons, M. E. G. The Oxygen Evolution Reaction: Mechanistic Concepts and Catalyst Design. In *Photoelectrochemical Solar Fuel Production: From Basic Principles to Advanced Devices*; Giménez, S., Bisquert, J., Eds.; Springer International Publishing: Cham, 2016; pp 41–104. https://doi.org/10.1007/978-3-319-29641-8_2.

(35) Sun, Y.; Liao, H.; Wang, J.; Chen, B.; Sun, S.; Ong, S. J. H.; Xi, S.; Diao, C.; Du, Y.; Wang, J. O.; Breese, M. B. H.; Li, S.; Zhang, H.; Xu, Z. J. Covalency Competition Dominates the Water Oxidation Structure–Activity Relationship on Spinel Oxides. *Nat. Catal.* **2020**, *3* (7), 554–563. https://doi.org/10.1038/s41929-020-0465-6.

(36) Nørskov, J. K.; Rossmeisl, J.; Logadottir, A.; Lindqvist, L.; Kitchin, J. R.; Bligaard, T.; Jónsson, H. Origin of the Overpotential for Oxygen Reduction at a Fuel-Cell Cathode. *J. Phys. Chem. B.* **2004**, *108* (46), 17886–17892. https://doi.org/10.1021/jp047349j.

(37) Viswanathan, V.; Hansen, H. A.; Rossmeisl, J.; Nørskov, J. K. Universality in Oxygen Reduction Electrocatalysis on Metal Surfaces. *ACS Catal.* **2012**, *2* (8), 1654–1660. https://doi.org/10.1021/cs300227s.

(38) Plevová, M.; Hnát, J.; Bouzek, K. Electrocatalysts for the Oxygen Evolution Reaction in Alkaline and Neutral Media. A Comparative Review. *J. Power Sources* **2021**, *507*, 230072. https://doi.org/10.1016/j.jpowsour.2021.230072.

(39) Matsumoto, Y.; Sato, E. Electrocatalytic Properties of Transition Metal Oxides for Oxygen Evolution Reaction. *Mater. Chem. Phys.* **1986**, *14* (5), 397–426. https://doi.org/10.1016/0254-0584(86)90045-3.

(40) Cook, T. R.; Dogutan, D. K.; Reece, S. Y.; Surendranath, Y.; Teets, T. S.; Nocera, D. G. Solar Energy Supply and Storage for the Legacy and Nonlegacy Worlds. *Chem. Rev.* **2010**, *110* (11), 6474–6502. https://doi.org/10.1021/cr100246c.

(41) Danilovic, N.; Subbaraman, R.; Strmcnik, D.; Chang, K. C.; Paulikas, A. P.; Stamenkovic, V. R.; Markovic, N. M. Enhancing the Alkaline Hydrogen Evolution Reaction Activity through the Bifunctionality of Ni(OH)2/Metal Catalysts. *Angew. Chem. Int. Ed.* **2012**, *51* (50), 12495–12498.

https://doi.org/10.1002/anie.201204842.
(42) Dubouis, N.; Grimaud, A. The Hydrogen Evolution Reaction: From Material to Interfacial Descriptors. *Chem. Sci.* **2019**, *10* (40), 9165–9181. https://doi.org/10.1039/C9SC03831K.
(43) Baek, D. S.; Lee, J.; Lim, J. S.; Joo, S. H. Nanoscale Electrocatalyst Design for Alkaline Hydrogen Evolution Reaction through Activity Descriptor Identification. *Mater. Chem. Front.* **2021**, *5* (11), 4042–4058. https://doi.org/10.1039/d1qm00183c.
(44) Skúlason, E.; Tripkovic, V.; Björketun, M. E.; Gudmundsdóttir, S.; Karlberg, G.; Rossmeisl, J.; Bligaard, T.; Jónsson, H.; Nørskov, J. K. Modeling the Electrochemical Hydrogen Oxidation and Evolution Reactions on the Basis of Density Functional Theory Calculations. *J. Phys. Chem. C* **2010**, *114* (42), 18182–18197. https://doi.org/10.1021/jp1048887.
(45) Helm, M. L.; Stewart, M. P.; Bullock, R. M.; DuBois, M. R.; DuBois, D. L. A Synthetic Nickel Electrocatalyst with a Turnover Frequency above 100,000 s-1 for H2 Production. *Science* **2011**, *333* (6044), 863–866. https://doi.org/10.1126/science.1205864.
(46) Garrido-Barros, P.; Gimbert-Suriñach, C.; Matheu, R.; Sala, X.; Llobet, A. How to Make an Efficient and Robust Molecular Catalyst for Water Oxidation. *Chem. Soc. Rev.* **2017**, *46* (20), 6088–6098. https://doi.org/10.1039/C7CS00248C.
(47) McCarthy, B. D.; Dempsey, J. L. Decoding Proton-Coupled Electron Transfer with Potential-PKa Diagrams. *Inorg. Chem.* **2017**, *56* (3), 1225–1231. https://doi.org/10.1021/acs.inorgchem.6b02325.
(48) Vereshchuk, N.; Matheu, R.; Benet-Buchholz, J.; Pipelier, M.; Lebreton, J.; Dubreuil, D.; Tessier, A.; Gimbert-Suriñach, C.; Ertem, M. Z.; Llobet, A. Second Coordination Sphere Effects in an Evolved Ru Complex Based on a Highly Adaptable Ligand Results in Rapid Water Oxidation Catalysis. *J. Am. Chem. Soc.* **2020**, *142* (11), 5068–5077. https://doi.org/10.1021/jacs.9b11935.
(49) Matheu, R.; Ertem, M. Z.; Benet-Buchholz, J.; Coronado, E.; Batista, V. S.; Sala, X.; Llobet, A. Intramolecular Proton Transfer Boosts Water Oxidation Catalyzed by a Ru Complex. *J. Am. Chem. Soc.* **2015**, *137* (33), 10786–10795. https://doi.org/10.1021/jacs.5b06541.

(50) Zhang, B.; Sun, L. Ru-Bda: Unique Molecular Water-Oxidation Catalysts with Distortion Induced Open Site and Negatively Charged Ligands. *J. Am. Chem. Soc.* **2019**, *141* (14), 5565–5580. https://doi.org/10.1021/jacs.8b12862.

(51) Yang, J.; Wang, L.; Zhan, S.; Zou, H.; Chen, H.; Ahlquist, M. S. G.; Duan, L.; Sun, L. From Ru-Bda to Ru-Bds: A Step Forward to Highly Efficient Molecular Water Oxidation Electrocatalysts under Acidic and Neutral Conditions. *Nat. Commun.* **2021**, *12*, 373. https://doi.org/10.1038/s41467-020-20637-8.

(52) Hoque, M. A.; Gil-Sepulcre, M.; de Aguirre, A.; Elemans, J. A. A. W.; Moonshiram, D.; Matheu, R.; Shi, Y.; Benet-Buchholz, J.; Sala, X.; Malfois, M.; Solano, E.; Lim, J.; Garzón-Manjón, A.; Scheu, C.; Lanza, M.; Maseras, F.; Gimbert-Suriñach, C.; Llobet, A. Water Oxidation Electrocatalysis Using Ruthenium Coordination Oligomers Adsorbed on Multiwalled Carbon Nanotubes. *Nat. Chem.* **2020**, *12* (11), 1060–1066. https://doi.org/10.1038/s41557-020-0548-7.

(53) Creus, J.; Matheu, R.; Peñafiel, I.; Moonshiram, D.; Blondeau, P.; Benet-Buchholz, J.; García-Antón, J.; Sala, X.; Godard, C.; Llobet, A. A Million Turnover Molecular Anode for Catalytic Water Oxidation. *Angew. Chem. Int. Ed.* **2016**, *55* (49), 15382–15386. https://doi.org/10.1002/anie.201609167.

(54) Gil-Sepulcre, M.; Lindner, J. O.; Schindler, D.; Velasco, L.; Moonshiram, D.; Rüdiger, O.; DeBeer, S.; Stepanenko, V.; Solano, E.; Würthner, F.; Llobet, A. Surface-Promoted Evolution of Ru-Bda Coordination Oligomers Boosts the Efficiency of Water Oxidation Molecular Anodes. *J. Am. Chem. Soc.* **2021**, *143* (30), 11651–11661. https://doi.org/10.1021/jacs.1c04738.

(55) Liseev, T.; Howe, A.; Hoque, M. A.; Gimbert-Suriñach, C.; Llobet, A.; Ott, S. Synthetic Strategies to Incorporate Ru-Terpyridyl Water Oxidation Catalysts into MOFs: Direct Synthesis: Vs. Post-Synthetic Approach. *Dalton Trans.* **2020**, *49* (39), 13753–13759. https://doi.org/10.1039/d0dt01890b.

(56) Ventosa, M.; Gil-Sepulcre, M.; Benet-Buchholz, J.; Gimbert-Suriñach, C.; Llobet, A. Anode Based on a Molecular Ru Water Oxidation Catalyst Covalently Bonded to Polythiophene. *ACS Appl. Energy Mater.* **2021**, *4* (9), 9775–9782. https://doi.org/10.1021/acsaem.1c01851.

(57) Wang, L.; Polyansky, D. E.; Concepcion, J. J. Self-Assembled Bilayers as an Anchoring Strategy: Catalysts, Chromophores, and Chromophore-Catalyst Assemblies. *J. Am. Chem. Soc.* **2019**, *141* (20), 8020–8024. https://doi.org/10.1021/jacs.9b01044.

(58) Wang, D.; Wang, L.; Brady, M. D.; Dares, C. J.; Meyer, G. J.; Meyer, T. J.; Concepcion, J. J. Self-Assembled Chromophore–Catalyst Bilayer for Water Oxidation in a Dye-Sensitized Photoelectrosynthesis Cell. *J. Phys. Chem. C* **2019**, *123* (50), 30039–30045. https://doi.org/10.1021/acs.jpcc.9b07125.

(59) Gil-Sepulcre, M.; Llobet, A. Molecular Water Oxidation Catalysts Based on First-Row Transition Metal Complexes. *Nat. Catal.* **2022**, *5* (2), 79–82. https://doi.org/10.1038/s41929-022-00750-1.

(60) Garrido-Barros, P.; Matheu, R.; Gimbert-Suriñach, C.; Llobet, A. Electronic, Mechanistic, and Structural Factors That Influence the Performance of Molecular Water Oxidation Catalysts Anchored on Electrode Surfaces. *Curr Opin Electrochem* **2019**, *15*, 140–147. https://doi.org/10.1016/j.coelec.2019.04.027.

(61) Grammatico, D.; Tran, H. N.; Li, Y.; Pugliese, S.; Billon, L.; Su, B. L.; Fontecave, M. Immobilization of a Molecular Re Complex on MOF-Derived Hierarchical Porous Carbon for CO2 Electroreduction in Water/Ionic Liquid Electrolyte. *ChemSusChem* **2020**, *13* (23), 6418–6425. https://doi.org/10.1002/cssc.202002014.

(62) McCusker, J. K. Electronic Structure in the Transition Metal Block and Its Implications for Light Harvesting. *Science* **2019**, *363* (6426), 484–488. https://doi.org/10.1126/science.aav9104.

(63) Liang, H.-W.; Brüller, S.; Dong, R.; Zhang, J.; Feng, X.; Müllen, K. Molecular Metal–Nx Centres in Porous Carbon for Electrocatalytic Hydrogen Evolution. *Nat. Commun.* **2015**, *6*, 7992. https://doi.org/10.1038/ncomms8992.

(64) Sa, Y. J.; Park, S. O.; Jung, G. Y.; Shin, T. J.; Jeong, H. Y.; Kwak, S. K.; Joo, S. H. Heterogeneous Co-N/C Electrocatalysts with Controlled Cobalt Site Densities for the Hydrogen Evolution Reaction: Structure-Activity Correlations and Kinetic Insights. *ACS Catal.* **2019**, *9* (1), 83–97. https://doi.org/10.1021/acscatal.8b03446.

(65) Yang, H.; Shang, L.; Zhang, Q.; Shi, R.; Waterhouse, G. I. N.; Gu,

L.; Zhang, T. A Universal Ligand Mediated Method for Large Scale Synthesis of Transition Metal Single Atom Catalysts. *Nat. Commun.* **2019**, *10*, 4585. https://doi.org/10.1038/s41467-019-12510-0.

(66) Zhang, H.; Hwang, S.; Wang, M.; Feng, Z.; Karakalos, S.; Luo, L.; Qiao, Z.; Xie, X.; Wang, C.; Su, D.; Shao, Y.; Wu, G. Single Atomic Iron Catalysts for Oxygen Reduction in Acidic Media: Particle Size Control and Thermal Activation. *J. Am. Chem. Soc.* **2017**, *139* (40), 14143–14149. https://doi.org/10.1021/jacs.7b06514.

(67) Morozan, A.; Goellner, V.; Nedellec, Y.; Hannauer, J.; Jaouen, F. Effect of the Transition Metal on Metal–Nitrogen–Carbon Catalysts for the Hydrogen Evolution Reaction. *J. Electrochem. Soc.* **2015**, *162* (9), H719–H726. https://doi.org/10.1149/2.0051511jes.

(68) Tang, J.; Salunkhe, R. R.; Liu, J.; Torad, N. L.; Imura, M.; Furukawa, S.; Yamauchi, Y. Thermal Conversion of Core-Shell Metal-Organic Frameworks: A New Method for Selectively Functionalized Nanoporous Hybrid Carbon. *J. Am. Chem. Soc.* **2015**, *137* (4), 1572–1580. https://doi.org/10.1021/ja511539a.

(69) McCrory, C. C. L.; Jung, S.; Peters, J. C.; Jaramillo, T. F. Benchmarking Heterogeneous Electrocatalysts for the Oxygen Evolution Reaction. *J. Am. Chem. Soc.* **2013**, *135* (45), 16977–16987. https://doi.org/10.1021/ja407115p.

(70) Gómez, M. J.; Diaz, L. A.; Franceschini, E. A.; Lacconi, G. I.; Abuin, G. C. 3D Nanostructured NiMo Catalyst Electrodeposited on 316L Stainless Steel for Hydrogen Generation in Industrial Applications. *J. Appl. Electrochem.* **2019**, *49* (12), 1227–1238. https://doi.org/10.1007/s10800-019-01361-8.

(71) Li, Z.; Shao, M.; An, H.; Wang, Z.; Xu, S.; Wei, M.; Evans, D. G.; Duan, X. Fast Electrosynthesis of Fe-Containing Layered Double Hydroxide Arrays toward Highly Efficient Electrocatalytic Oxidation Reactions. *Chem. Sci.* **2015**, *6* (11), 6624–6631. https://doi.org/10.1039/c5sc02417j.

(72) Ganguli, S.; Ghosh, S.; Das, S.; Mahalingam, V. Inception of Molybdate as a "Pore Forming Additive" to Enhance the Bifunctional Electrocatalytic Activity of Nickel and Cobalt Based Mixed Hydroxides for Overall Water Splitting. *Nanoscale* **2019**, *11* (36), 16896–16906. https://doi.org/10.1039/c9nr05142b.

(73) Xu, X.; Song, F.; Hu, X. A Nickel Iron Diselenide-Derived Efficient Oxygen-Evolution Catalyst. *Nat. Commun.* **2016**, *7*, 12324. https://doi.org/10.1038/ncomms12324.

(74) Lu, Q.; Hutchings, G. S.; Yu, W.; Zhou, Y.; Forest, R. V.; Tao, R.; Rosen, J.; Yonemoto, B. T.; Cao, Z.; Zheng, H.; Xiao, J. Q.; Jiao, F.; Chen, J. G. Highly Porous Non-Precious Bimetallic Electrocatalysts for Efficient Hydrogen Evolution. *Nat. Commun.* **2015**, *6*, 6567. https://doi.org/10.1038/ncomms7567.

(75) Qiu, Z.; Tai, C. W.; Niklasson, G. A.; Edvinsson, T. Direct Observation of Active Catalyst Surface Phases and the Effect of Dynamic Self-Optimization in NiFe-Layered Double Hydroxides for Alkaline Water Splitting. *Energy Environ. Sci.* **2019**, *12* (2), 572–581. https://doi.org/10.1039/c8ee03282c.

(76) Li, N.; Bediako, D. K.; Hadt, R. G.; Hayes, D.; Kempa, T. J.; Von Cube, F.; Bell, D. C.; Chen, L. X.; Nocera, D. G. Influence of Iron Doping on Tetravalent Nickel Content in Catalytic Oxygen Evolving Films. *Proc. Natl. Acad. Sci. U. S. A.* **2017**, *114* (7), 1486–1491. https://doi.org/10.1073/pnas.1620787114.

(77) Hunter, B. M.; Thompson, N. B.; Müller, A. M.; Rossman, G. R.; Hill, M. G.; Winkler, J. R.; Gray, H. B. Trapping an Iron(VI) Water-Splitting Intermediate in Nonaqueous Media. *Joule* **2018**, *2* (4), 747–763. https://doi.org/10.1016/j.joule.2018.01.008.

(78) Zhang, J.; Wang, T.; Liu, P.; Liao, Z.; Liu, S.; Zhuang, X.; Chen, M.; Zschech, E.; Feng, X. Efficient Hydrogen Production on MoNi4 Electrocatalysts with Fast Water Dissociation Kinetics. *Nat. Commun.* **2017**, *8*, 15437. https://doi.org/10.1038/ncomms15437.

(79) Wang, X.; Su, R.; Aslan, H.; Kibsgaard, J.; Wendt, S.; Meng, L.; Dong, M.; Huang, Y.; Besenbacher, F. Tweaking the Composition of NiMoZn Alloy Electrocatalyst for Enhanced Hydrogen Evolution Reaction Performance. *Nano Energy* **2015**, *12*, 9–18. https://doi.org/10.1016/j.nanoen.2014.12.007.

(80) Liu, X.; Meng, J.; Ni, K.; Guo, R.; Xia, F.; Xie, J.; Li, X.; Wen, B.; Wu, P.; Li, M.; Wu, J.; Wu, X.; Mai, L.; Zhao, D. Complete Reconstruction of Hydrate Pre-Catalysts for Ultrastable Water Electrolysis in Industrial-Concentration Alkali Media. *Cell Reports Phys. Sci.* **2020**, *1* (11), 100241. https://doi.org/10.1016/j.xcrp.2020.100241.

(81) Choi, J.; Kim, D.; Zheng, W.; Yan, B.; Li, Y.; Lee, L. Y. S.; Piao, Y. Interface Engineered NiFe2O4−x/NiMoO4 Nanowire Arrays for Electrochemical Oxygen Evolution. *Appl. Catal. B* **2021**, *286* (6), 119857. https://doi.org/10.1016/j.apcatb.2020.119857.

(82) Dürr, R. N.; Maltoni, P.; Tian, H.; Jousselme, B.; Hammarström, L.; Edvinsson, T. From NiMoO4 to γ-NiOOH: Detecting the Active Catalyst Phase by Time Resolved in Situ and Operando Raman Spectroscopy. *ACS Nano* **2021**, *15* (8), 13504–13515. https://doi.org/10.1021/acsnano.1c04126.

(83) Qiu, Z.; Ma, Y.; Edvinsson, T. In Operando Raman Investigation of Fe Doping Influence on Catalytic NiO Intermediates for Enhanced Overall Water Splitting. *Nano Energy* **2019**, *66* (12), 104118. https://doi.org/10.1016/j.nanoen.2019.104118.

(84) Wilson, M. *Microscope Resolution: Concepts, Factors and Calculation*. https://www.leica-microsystems.com/science-lab/microscope-resolution-concepts-factors-and-calculation/ (accessed 2022-04-26).

(85) *Keywords "chromatic aberration" | Keywords | Glossary of SEM Terms | JEOL*. https://www.jeol.co.jp/en/words/semterms/search_result.html?keyword=chromatic aberration (accessed 2022-04-27).

(86) Goldstein, J. I.; Newbury, D. E.; Michael, J. R.; Ritchie, N. W. M.; Scott, J. H. J.; Joy, D. C. Secondary Electrons. In *Scanning Electron Microscopy and X-Ray Microanalysis*; Springer New York, 2018; pp 29–37. https://doi.org/10.1007/978-1-4939-6676-9_3.

(87) Siegbahn, K.; Nordling, C.; Fahlman, A.; Nordberg, R.; Hamrin, K.; Hedman, J.; Johansson, G.; Bergmark, T.; Karlsson, S.-E.; Lindgren, I.; Lindberg, B. J. *ESCA - Atomic, Molecular and Solid State Structure Studied by Means of Electron Spectroscopy*; Nova acta Regiae Societatis scientiarum Upsaliensis. Ser. 4; 20; Almqvist and Wiksell: Uppsala, 1967; Vol. 20.

(88) NobelPrize.org. *The Noble Prize in Physics 1981*. https://www.nobelprize.org/prizes/physics/1981/summary/ (accessed 2022-03-24).

(89) *X-Ray Photoelectron Spectroscopy (XPS) Surface Analysis Technique*. https://www.phi.com/surface-analysis-techniques/xps-esca.html (accessed 2022-03-26).

(90) Einstein, A. Über einen die Erzeugung und Verwandlung des

Lichtes betreffenden heuristischen Gesichtspunkt. *Ann Phys* **1905**, *322* (6), 132–148. https://doi.org/10.1002/andp.19053220607.

(91) Casa Software Ltd. *XPS Instrumentation*. http://www.casaxps.com/help_manual/XPSInformation/XPSIntr.htm (accessed 2022-03-26).

(92) Verma, H. R. X-Ray Photoelectron Spectroscopy. In *Atomic and Nuclear Analytical Methods*; Springer: Berlin, 2007; pp 213–241.

(93) Tougaard, S. Practical Guide to the Use of Backgrounds in Quantitative XPS. *J. Vac. Sci. Technol. A* **2021**, *39* (1), 011201. https://doi.org/10.1116/6.0000661.

(94) Kawai, J.; Adachi, H.; Kitajima, Y.; Maeda, K.; Hayakawa, S.; Gohshi, Y. Inelastic Mean Free Path of Photoelectrons in Ag Determined by Total Reflection X-Ray Photoelectron Spectroscopy. *Anal. Sci.* **1997**, *13* (5), 797–801. https://doi.org/10.2116/analsci.13.797.

(95) *X-ray photoelectron spectroscopy (XPS) - The technique in brief*. https://www.kratos.com/applications/techniques/x-ray-photoelectron-spectroscopy (accessed 2022-03-26).

(96) Costentin, C.; Drouet, S.; Robert, M.; Savéant, J. M. Turnover Numbers, Turnover Frequencies, and Overpotential in Molecular Catalysis of Electrochemical Reactions. Cyclic Voltammetry and Preparative-Scale Electrolysis. *J. Am. Chem. Soc.* **2012**, *134* (27), 11235–11242. https://doi.org/10.1021/ja303560c.

(97) Matheu, R.; Neudeck, S.; Meyer, F.; Sala, X.; Llobet, A. Foot of the Wave Analysis for Mechanistic Elucidation and Benchmarking Applications in Molecular Water Oxidation Catalysis. *ChemSusChem* **2016**, *9* (23), 3361–3369. https://doi.org/10.1002/cssc.201601286.

(98) Elgrishi, N.; Rountree, K. J.; McCarthy, B. D.; Rountree, E. S.; Eisenhart, T. T.; Dempsey, J. L. A Practical Beginner's Guide to Cyclic Voltammetry. *J. Chem. Educ.* **2018**, *95* (2), 197–206. https://doi.org/10.1021/acs.jchemed.7b00361.

(99) Savéant, J.; Costentin, C. Single-Electron Transfer at an Electrode. In *Elements of Molecular and Biomolecular Electrochemistry*; John Wiley & sons Inc.: New Jersey, 2019; pp 1–80.

(100) Zheng, W.; Liu, M.; Lee, L. Y. S. Best Practices in Using Foam-Type Electrodes for Electrocatalytic Performance Benchmark. *ACS Energy Lett.* **2020**, *5* (10), 3260–3264. https://doi.org/10.1021/acsenergylett.0c01958.
(101) Córdoba-Torres, P.; Mesquita, T. J.; Nogueira, R. P. Relationship between the Origin of Constant-Phase Element Behavior in Electrochemical Impedance Spectroscopy and Electrode Surface Structure. *J. Phys. Chem. C* **2015**, *119* (8), 4136–4147. https://doi.org/10.1021/jp512063f.
(102) Shoar Abouzari, M. R.; Berkemeier, F.; Schmitz, G.; Wilmer, D. On the Physical Interpretation of Constant Phase Elements. *Solid State Ion.* **2009**, *180* (14–16), 922–927. https://doi.org/10.1016/j.ssi.2009.04.002.
(103) Hayes, W.; Loudon, R. *Scattering of Light by Crystals*; Dover Publications, Inc.: Mineola, 2004.
(104) Sander, T.; Reindl, C. T.; Klar, P. J. Breaking of Raman Selection Rules in Cu2O by Intrinsic Point Defects. *Mater. Res. Soc. Symp. Proc.* **2014**, *1633*, 81–86. https://doi.org/10.1557/opl.2014.47.
(105) Gersten, S. W.; Samuels, G. J.; Meyer, T. J. Catalytic Oxidation of Water by an Oxo-Bridged Ruthenium Dimer. *J. Am. Chem. Soc.* **1982**, *104* (14), 4029–4030. https://doi.org/10.1021/ja00378a053.
(106) Duan, L.; Fischer, A.; Xu, Y.; Sun, L. Isolated Seven-Coordinate Ru(IV) Dimer Complex with [HOHOH]− Bridging Ligand as an Intermediate for Catalytic Water Oxidation. *J. Am. Chem. Soc.* **2009**, *131* (30), 10397–10399. https://doi.org/10.1021/ja9034686.
(107) Duan, L.; Bozoglian, F.; Mandal, S.; Stewart, B.; Privalov, T.; Llobet, A.; Sun, L. A Molecular Ruthenium Catalyst with Water-Oxidation Activity Comparable to That of Photosystem II. *Nat. Chem.* **2012**, *4* (5), 418–423. https://doi.org/10.1038/nchem.1301.
(108) Matheu, R.; Francàs, L.; Chernev, P.; Ertem, M. Z.; Batista, V.; Haumann, M.; Sala, X.; Llobet, A. Behavior of the Ru-Bda Water Oxidation Catalyst Covalently Anchored on Glassy Carbon Electrodes. *ACS Catal.* **2015**, *5* (6), 3422–3429. https://doi.org/10.1021/acscatal.5b00132.
(109) Dürr, R. N.; Chasvised, S.; Gil-Sepulcre, M.; Howe, A.; Hoque, M.

A.; N'Guyen, V.; Sadeghi, S.; Reynaud, S.; Cugnet, C.; Authier, L.; Gimbert-Suriñach, C.; Bousquet, A.; Llobet, A.; Billon, L. Robust and Efficient Screen-Printed Molecular Anodes with Anchored Water Oxidation Catalysts. *ACS Appl. Energy Mater.* **2021**, *4* (10), 10534–10541. https://doi.org/10.1021/acsaem.1c01435.

(110) Matheu, R.; Neudeck, S.; Meyer, F.; Sala, X.; Llobet, A. Foot of the Wave Analysis for Mechanistic Elucidation and Benchmarking Applications in Molecular Water Oxidation Catalysis. *ChemSusChem* **2016**, *9* (23), 3361–3369. https://doi.org/10.1002/cssc.201601286.

(111) Zhou, Z.; Pei, Z.; Wei, L.; Zhao, S.; Jian, X.; Chen, Y. Electrocatalytic Hydrogen Evolution under Neutral PH Conditions: Current Understandings, Recent Advances, and Future Prospects. *Energy Environ. Sci.* **2020**, *13* (10), 3185–3206. https://doi.org/10.1039/D0EE01856B.

(112) W. Wakerley, D.; Reisner, E. Development and Understanding of Cobaloxime Activity through Electrochemical Molecular Catalyst Screening. *Phys. Chem. Chem. Phys.*, **2014**, *16* (12), 5739–5746. https://doi.org/10.1039/C4CP00453A.

(113) Lakadamyali, F.; Kato, M.; Muresan, N. M.; Reisner, E. Selective Reduction of Aqueous Protons to Hydrogen with a Synthetic Cobaloxime Catalyst in the Presence of Atmospheric Oxygen. *Angew. Chem. Int. Ed.* **2012**, *51* (37), 9381–9384. https://doi.org/10.1002/anie.201204180.

(114) Wadsworth, B. L.; Beiler, A. M.; Khusnutdinova, D.; Jacob, S. I.; Moore, G. F. Electrocatalytic and Optical Properties of Cobaloxime Catalysts Immobilized at a Surface-Grafted Polymer Interface. *ACS Catal.* **2016**, *6* (12), 8048–8057. https://doi.org/10.1021/acscatal.6b02194.

(115) Muresan, N. M.; Willkomm, J.; Mersch, D.; Vaynzof, Y.; Reisner, E. Immobilization of a Molecular Cobaloxime Catalyst for Hydrogen Evolution on a Mesoporous Metal Oxide Electrode. *Angew. Chem.* **2012**, *124* (51), 12921–12925. https://doi.org/10.1002/ange.201207448.

(116) Liu, T.; Li, P.; Yao, N.; Cheng, G.; Chen, S.; Luo, W.; Yin, Y. CoP-Doped MOF-Based Electrocatalyst for PH-Universal Hydrogen Evolution Reaction. *Angew. Chem. Int. Ed.* **2019**, *58* (14), 4679–4684. https://doi.org/10.1002/anie.201901409.

(117) Ahmed, M. E.; Nayek, A.; Križan, A.; Coutard, N.; Morozan, A.; Ghosh Dey, S.; Lomoth, R.; Hammarström, L.; Artero, V.; Dey, A. A Bidirectional Bioinspired [FeFe]-Hydrogenase Model. *J. Am. Chem. Soc.* **2022**, *144* (8), 3614–3625. https://doi.org/10.1021/jacs.1c12605.

(118) Madden, C.; Vaughn, M. D.; Díez-Pérez, I.; Brown, K. A.; King, P. W.; Gust, D.; Moore, A. L.; Moore, T. A. Catalytic Turnover of [FeFe]-Hydrogenase Based on Single-Molecule Imaging. *J. Am. Chem. Soc.* **2012**, *134* (3), 1577–1582. https://doi.org/10.1021/ja207461t.

(119) Hongsirikarn, K.; Goodwin, J. G.; Greenway, S.; Creager, S. Effect of Cations (Na+, Ca2+, Fe3+) on the Conductivity of a Nafion Membrane. *J. Power Sources* **2010**, *195* (21), 7213–7220. https://doi.org/10.1016/j.jpowsour.2010.05.005.

(120) Materna, K. L.; Crabtree, R. H.; Brudvig, G. W. Anchoring Groups for Photocatalytic Water Oxidation on Metal Oxide Surfaces. *Chem. Soc. Rev.* **2017**, *46* (20), 6099–6110. https://doi.org/10.1039/C7CS00314E.

(121) Le Goff, A.; Moggia, F.; Debou, N.; Jegou, P.; Artero, V.; Fontecave, M.; Jousselme, B.; Palacin, S. Facile and Tunable Functionalization of Carbon Nanotube Electrodes with Ferrocene by Covalent Coupling and π-Stacking Interactions and Their Relevance to Glucose Bio-Sensing. *J. Electroanal. Chem.* **2010**, *641* (1–2), 57–63. https://doi.org/10.1016/j.jelechem.2010.01.014.

(122) Tran, P. D.; Le Goff, A.; Heidkamp, J.; Jousselme, B.; Guillet, N.; Palacin, S.; Dau, H.; Fontecave, M.; Artero, V. Noncovalent Modification of Carbon Nanotubes with Pyrene-Functionalized Nickel Complexes: Carbon Monoxide Tolerant Catalysts for Hydrogen Evolution and Uptake. *Angew. Chem.* **2011**, *123* (6), 1407–1410. https://doi.org/10.1002/ange.201005427.

(123) Howe, A.; Liseev, T.; Gil-Sepulcre, M.; Gimbert-Suriñach, C.; Benet-Buchholz, J.; Llobet, A.; Ott, S. Electrocatalytic Water Oxidation from a Mixed Linker MOF Based on NU-1000 with an Integrated Ruthenium-Based Metallo-Linker. *Mater. Adv.* **2022**, *3* (10), 4227–4234. https://doi.org/10.1039/D2MA00128D.

(124) Wang, L.; Fan, K.; Chen, H.; Daniel, Q.; Philippe, B.; Rensmo, H.; Sun, L. Towards Efficient and Robust Anodes for Water Splitting:

Immobilization of Ru Catalysts on Carbon Electrode and Hematite by in Situ Polymerization. *Catal. Today* **2017**, *290*, 73–77. https://doi.org/10.1016/j.cattod.2016.07.011.

(125) Wang, L.; Fan, K.; Daniel, Q.; Duan, L.; Li, F.; Philippe, B.; Rensmo, H.; Chen, H.; Sun, J.; Sun, L. Electrochemical Driven Water Oxidation by Molecular Catalysts in Situ Polymerized on the Surface of Graphite Carbon Electrode. *Chem. Commun.* **2015**, *51* (37), 7883–7886. https://doi.org/10.1039/C5CC00242G.

(126) Xie, Y.; Shaffer, D. W.; Lewandowska-Andralojc, A.; Szalda, D. J.; Concepcion, J. J. Water Oxidation by Ruthenium Complexes Incorporating Multifunctional Bipyridyl Diphosphonate Ligands. *Angew. Chem. Int. Ed.* **2016**, *55* (28), 8067–8071. https://doi.org/10.1002/anie.201601943.

(127) Shaffer, D. W.; Xie, Y.; Szalda, D. J.; Concepcion, J. J. Lability and Basicity of Bipyridine-Carboxylate-Phosphonate Ligand Accelerate Single-Site Water Oxidation by Ruthenium-Based Molecular Catalysts. *J. Am. Chem. Soc.* **2017**, *139* (43), 15347–15355. https://doi.org/10.1021/jacs.7b06096.

(128) Schindler, D.; Gil-Sepulcre, M.; Lindner, J. O.; Stepanenko, V.; Moonshiram, D.; Llobet, A.; Würthner, F. Efficient Electrochemical Water Oxidation by a Trinuclear Ru(Bda) Macrocycle Immobilized on Multi-Walled Carbon Nanotube Electrodes. *Adv. Energy Mater.* **2020**, *10* (43), 2002329. https://doi.org/10.1002/aenm.202002329.

(129) Zheng, T.; Li, L. {[Ru(Bda)]:XLy}n Cross-Linked Coordination Polymers: Toward Efficient Heterogeneous Catalysis for Water Oxidation in an Organic Solvent-Free System. *New J. Chem.* **2018**, *42* (4), 2526–2536. https://doi.org/10.1039/c7nj04330a.

(130) Guo, J.; Liu, H.; Li, D.; Wang, J.; Djitcheu, X.; He, D.; Zhang, Q. A Minireview on the Synthesis of Single Atom Catalysts. *RSC Adv.* **2022**, *12* (15), 9373–9394. https://doi.org/10.1039/D2RA00657J.

(131) Fei, H.; Cahill, J. F.; Prather, K. A.; Cohen, S. M. Tandem Postsynthetic Metal Ion and Ligand Exchange in Zeolitic Imidazolate Frameworks. *Inorg. Chem.* **2013**, *52* (7), 4011–4016. https://doi.org/10.1021/ic400048g.

(132) Mphuthi, L. E.; Erasmus, E.; Langner, E. H. G. Metal Exchange of ZIF-8 and ZIF-67 Nanoparticles with Fe(II) for Enhanced

Photocatalytic Performance. *ACS Omega* **2021**, *6* (47), 31632–31645. https://doi.org/10.1021/acsomega.1c04142.
(133) Wang, J.; Xu, F.; Jin, H.; Chen, Y.; Wang, Y. Non-Noble Metal-Based Carbon Composites in Hydrogen Evolution Reaction: Fundamentals to Applications. *Adv. Mater.* **2017**, *29* (14), 1605838. https://doi.org/10.1002/adma.201605838.
(134) Liu, Q.; Liu, X.; Zheng, L.; Shui, J. The Solid-Phase Synthesis of an Fe-N-C Electrocatalyst for High-Power Proton-Exchange Membrane Fuel Cells. *Angew. Chem. Int. Ed.* **2018**, *57* (5), 1204–1208. https://doi.org/10.1002/anie.201709597.
(135) Phillips, R.; Dunnill, C. W. Zero Gap Alkaline Electrolysis Cell Design for Renewable Energy Storage as Hydrogen Gas. *RSC Adv.* **2016**, *6* (102), 100643–100651. https://doi.org/10.1039/C6RA22242K.
(136) Haverkort, J. W.; Rajaei, H. Voltage Losses in Zero-Gap Alkaline Water Electrolysis. *J. Power Sources* **2021**, *497*, 229864. https://doi.org/10.1016/j.jpowsour.2021.229864.
(137) Thanasilp, S.; Hunsom, M. Effect of MEA Fabrication Techniques on the Cell Performance of Pt-Pd/C Electrocatalyst for Oxygen Reduction in PEM Fuel Cell. *Fuel* **2010**, *89* (12), 3847–3852. https://doi.org/10.1016/j.fuel.2010.07.008.
(138) Park, I.-S.; Li, W.; Manthiram, A. Fabrication of Catalyst-Coated Membrane-Electrode Assemblies by Doctor Blade Method and Their Performance in Fuel Cells. *J. Power Sources* **2010**, *195* (20), 7078–7082. https://doi.org/10.1016/j.jpowsour.2010.05.004.
(139) Jung, H.-Y.; Kim, J. W. Role of the Glass Transition Temperature of Nafion 117 Membrane in the Preparation of the Membrane Electrode Assembly in a Direct Methanol Fuel Cell (DMFC). *Int. J. Hydrog. Energy* **2012**, *37* (17), 12580–12585. https://doi.org/10.1016/j.ijhydene.2012.05.121.
(140) Yazdanpour, M.; Esmaeilifar, A.; Rowshanzamir, S. Effects of Hot Pressing Conditions on the Performance of Nafion Membranes Coated by Ink-Jet Printing of Pt/MWCNTs Electrocatalyst for PEMFCs. *Int. J. Hydrog. Energy* **2012**, *37* (15), 11290–11298. https://doi.org/10.1016/j.ijhydene.2012.04.139.
(141) Li, X.; Liu, L.; Ren, X.; Gao, J.; Huang, Y.; Liu, B. Microenvironment Modulation of Single-Atom Catalysts and Their Roles in Electrochemical Energy Conversion. *Sci. Adv.* **2020**, *6* (39),

eabb6833. https://doi.org/10.1126/sciadv.abb6833.
(142) Queyriaux, N.; Sun, D.; Fize, J.; Pécaut, J.; Field, M. J.; Chavarot-Kerlidou, M.; Artero, V. Electrocatalytic Hydrogen Evolution with a Cobalt Complex Bearing Pendant Proton Relays: Acid Strength and Applied Potential Govern Mechanism and Stability. *J. Am. Chem. Soc.* **2020**, *142* (1), 274–282. https://doi.org/10.1021/jacs.9b10407.
(143) Antuch, M.; Millet, P. Approach to the Mechanism of Hydrogen Evolution Electrocatalyzed by a Model Co Clathrochelate: A Theoretical Study by Density Functional Theory. *ChemPhysChem* **2018**, *19* (19), 2549–2558. https://doi.org/10.1002/cphc.201800383.
(144) Tilak, B. V.; Chen, C. P. Generalized Analytical Expressions for Tafel Slope, Reaction Order and a.c. Impedance for the Hydrogen Evolution Reaction (HER): Mechanism of HER on Platinum in Alkaline Media. *J. Appl. Electrochem.* **1993**, *23*, 631–640. https://doi.org/10.1007/BF00721955.
(145) Carmo, M.; Fritz, D. L.; Mergel, J.; Stolten, D. A Comprehensive Review on PEM Water Electrolysis. *Int. J. Hydrog. Energy* **2013**, *38* (12), 4901–4934. https://doi.org/10.1016/j.ijhydene.2013.01.151.
(146) Moreno-Hernandez, I. A.; MacFarland, C. A.; Read, C. G.; Papadantonakis, K. M.; Brunschwig, B. S.; Lewis, N. S. Crystalline Nickel Manganese Antimonate as a Stable Water-Oxidation Catalyst in Aqueous 1.0 M H2SO4. *Energy Environ. Sci.* **2017**, *10* (10), 2103–2108. https://doi.org/10.1039/C7EE01486D.
(147) Subbaraman, R.; Tripkovic, D.; Chang, K.-C.; Strmcnik, D.; Paulikas, A. P.; Hirunsit, P.; Chan, M.; Greeley, J.; Stamenkovic, V.; Markovic, N. M. Trends in Activity for the Water Electrolyser Reactions on 3d M(Ni,Co,Fe,Mn) Hydr(Oxy)Oxide Catalysts. *Nat. Mater.* **2012**, *11* (6), 550–557. https://doi.org/10.1038/nmat3313.
(148) Liu, E.; Li, J.; Jiao, L.; Doan, H. T. T.; Liu, Z.; Zhao, Z.; Huang, Y.; Abraham, K. M.; Mukerjee, S.; Jia, Q. Unifying the Hydrogen Evolution and Oxidation Reactions Kinetics in Base by Identifying the Catalytic Roles of Hydroxyl-Water-Cation Adducts. *J. Am. Chem. Soc.* **2019**, *141* (7), 3232–3239. https://doi.org/10.1021/jacs.8b13228.

(149) Kone, I.; Ahmad, Z.; Xie, A.; Tang, Y.; Sun, Y.; Chen, Y.; Yang, X.; Wan, P. In Situ Growth of Co4N Nanoparticles–Embedded Nitrogen-Doped Carbon Nanotubes on Metal–Organic Framework–Derived Carbon Composite as Highly Efficient Electrocatalyst for Oxygen Reduction and Evolution Reactions. *Energy Technol.* **2020**, *8* (9), 2000409. https://doi.org/10.1002/ente.202000409.

(150) Reece, S. Y.; Hamel, J. A.; Sung, K.; Jarvi, T. D.; Esswein, A. J.; Pijpers, J. J. H.; Nocera, D. G. Wireless Solar Water Splitting Using Silicon-Based Semiconductors and Earth-Abundant Catalysts. *Science* **2011**, *334* (6056), 645–648. https://doi.org/10.1126/science.1209816.

(151) Lv, Z.; Li, Z. Z.; Tan, X.; Li, Z. Z.; Wang, R.; Wen, M.; Liu, X.; Wang, G.; Xie, G.; Jiang, L. One-Step Electrodeposited NiFeMo Hybrid Film for Efficient Hydrogen Production via Urea Electrolysis and Water Splitting. *Appl. Surf. Sci.* **2021**, *552*, 149514. https://doi.org/10.1016/j.apsusc.2021.149514.

(152) Cai, D.; Wang, D.; Liu, B.; Wang, Y.; Liu, Y.; Wang, L.; Li, H.; Huang, H.; Li, Q.; Wang, T. Comparison of the Electrochemical Performance of NiMoO4 Nanorods and Hierarchical Nanospheres for Supercapacitor Applications. *ACS Appl. Mater. Interfaces* **2013**, *5* (24), 12905–12910. https://doi.org/10.1021/am403444v.

(153) Bankar, P. K.; Ratha, S.; More, M. A.; Late, D. J.; Rout, C. S. Enhanced Field Emission Performance of NiMoO 4 Nanosheets by Tuning the Phase. *Appl. Surf. Sci.* **2017**, *418*, 270–274. https://doi.org/10.1016/j.apsusc.2017.02.177.

(154) Peng, S.; Li, L.; Wu, H. B.; Madhavi, S.; Lou, X. W. (David). Controlled Growth of NiMoO4 Nanosheet and Nanorod Arrays on Various Conductive Substrates as Advanced Electrodes for Asymmetric Supercapacitors. *Adv. Energy Mater.* **2015**, *5* (2), 1401172. https://doi.org/10.1002/aenm.201401172.

(155) European Commission, Directorate-General for Internal Market, Industry, Entrepreneurship and SMEs, *Study on the Review of the List of Critical Raw Materials : Critical Raw Materials Factsheets,* Publications Office, 2017, https://data.europa.eu/10.2873/876644.

(156) Chen, J.; Zhao, G.; Chen, Y.; Rui, K.; Mao, H.; Dou, S. X.; Sun, W.

Iron-Doped Nickel Molybdate with Enhanced Oxygen Evolution Kinetics. *Chem. Eur. J.* **2019**, *25* (1), 280–284. https://doi.org/10.1002/chem.201803844.

(157) Jin, Y.; Yue, X.; Shu, C.; Huang, S.; Shen, P. K. Three-Dimensional Porous MoNi4 Networks Constructed by Nanosheets as Bifunctional Electrocatalysts for Overall Water Splitting. *J. Mater. Chem. A* **2017**, *5* (6), 2508–2513. https://doi.org/10.1039/c6ta10802d.

(158) Zhang, Z.; Ma, X.; Tang, J. Porous NiMoO4- x/MoO2 Hybrids as Highly Effective Electrocatalysts for the Water Splitting Reaction. *J. Mater. Chem. A* **2018**, *6* (26), 12361–12369. https://doi.org/10.1039/c8ta03047b.

(159) Chen, Y.-Y.; Zhang, Y.; Zhang, X.; Tang, T.; Luo, H.; Niu, S.; Dai, Z.-H.; Wan, L.-J.; Hu, J.-S. Self-Templated Fabrication of MoNi4/MoO3-x Nanorod Arrays with Dual Active Components for Highly Efficient Hydrogen Evolution. *Adv. Mater.* **2017**, *29* (39), 1703311. https://doi.org/10.1002/adma.201703311.

(160) Wang, Z.; Chen, J.; Song, E.; Wang, N.; Dong, J.; Zhang, X.; Ajayan, P. M.; Yao, W.; Wang, C.; Liu, J.; Shen, J.; Ye, M. Manipulation on Active Electronic States of Metastable Phase β-NiMoO4 for Large Current Density Hydrogen Evolution. *Nat. Commun.* **2021**, *12*, 5960. https://doi.org/10.1038/s41467-021-26256-1.

(161) Du, W.; Shi, Y.; Zhou, W.; Yu, Y.; Zhang, B. Unveiling the In Situ Dissolution and Polymerization of Mo in Ni4Mo Alloy for Promoting the Hydrogen Evolution Reaction. *Angew. Chem. Int. Ed.* **2021**, *60* (13), 7051–7055. https://doi.org/10.1002/anie.202015723.

(162) Eda, K.; Kato, Y.; Ohshiro, Y.; Sugitani, T.; Whittingham, M. S. Synthesis, Crystal Structure, and Structural Conversion of Ni Molybdate Hydrate NiMoO4·nH2O. *J. Solid State Chem.* **2010**, *183* (6), 1334–1339. https://doi.org/10.1016/j.jssc.2010.04.009.

(163) Ding, Y.; Wan, Y.; Min, Y. L.; Zhang, W.; Yu, S. H. General Synthesis and Phase Control of Metal Molybdate Hydrates MMoO 4·nH2O (M = Co, Ni, Mn, n = 0, 3/4, 1) Nano/Microcrystals by a Hydrothermal Approach: Magnetic, Photocatalytic, and Electrochemical Properties. *Inorg. Chem.* **2008**, *47* (17), 7813–7823. https://doi.org/10.1021/ic8007975.

(164) Dürr, R. N.; Maltoni, P.; Tian, H.; Jousselme, B.; Hammarström, L.; Edvinsson, T. Correction to "From NiMoO 4 to γ-NiOOH: Detecting the Active Catalyst Phase by Time Resolved in Situ and Operando Raman Spectroscopy." *ACS Nano* **2021**, *15* (12), 20693–20693. https://doi.org/10.1021/acsnano.1c10145.

(165) Gunjakar, J. L.; Inamdar, A. I.; Hou, B.; Cha, S.; Pawar, S. M.; Abu Talha, A. A.; Chavan, H. S.; Kim, J.; Cho, S.; Lee, S.; Jo, Y.; Kim, H.; Im, H. Direct Growth of 2D Nickel Hydroxide Nanosheets Intercalated with Polyoxovanadate Anions as a Binder-Free Supercapacitor Electrode. *Nanoscale* **2018**, *10* (19), 8953–8961. https://doi.org/10.1039/c7nr09626g.

(166) Qiu, Z.; Ma, Y.; Edström, K.; Niklasson, G. A.; Edvinsson, T. Controlled Crystal Growth Orientation and Surface Charge Effects in Self-Assembled Nickel Oxide Nanoflakes and Their Activity for the Oxygen Evolution Reaction. *Int. J. Hydrog. Energy* **2017**, *42* (47), 28397–28407. https://doi.org/10.1016/j.ijhydene.2017.09.117.

(167) P. Browne, M.; Sofer, Z.; Pumera, M. Layered and Two Dimensional Metal Oxides for Electrochemical Energy Conversion. *Energy Environ. Sci.* **2019**, *12* (1), 41–58. https://doi.org/10.1039/C8EE02495B.

(168) Tan, H. T.; Sun, W.; Wang, L.; Yan, Q. 2D Transition Metal Oxides/Hydroxides for Energy-Storage Applications. *ChemNanoMat* **2016**, *2* (7), 562–577. https://doi.org/10.1002/cnma.201500177.

(169) Diaz-Morales, O.; Ferrus-Suspedra, D.; Koper, M. T. M. The Importance of Nickel Oxyhydroxide Deprotonation on Its Activity towards Electrochemical Water Oxidation. *Chem. Sci.* **2016**, *7* (4), 2639–2645. https://doi.org/10.1039/c5sc04486c.

(170) Haj-Bsoul, S.; Varcoe, J. R.; Dekel, D. R. Measuring the Alkaline Stability of Anion-Exchange Membranes. *J. Electroanal. Chem.* **2022**, *908*, 116112. https://doi.org/10.1016/j.jelechem.2022.116112.

(171) Varcoe, J. R.; Atanassov, P.; Dekel, D. R.; Herring, A. M.; Hickner, M. A.; Kohl, P. A.; Kucernak, A. R.; Mustain, W. E.; Nijmeijer, K.; Scott, K.; Xu, T.; Zhuang, L. Anion-Exchange Membranes in Electrochemical Energy Systems. *Energy Environ. Sci.* **2014**, *7* (10), 3135–3191. https://doi.org/10.1039/C4EE01303D.

(172) Wang, Z.; Zheng, Y. R.; Montoya, J.; Hochfilzer, D.; Cao, A.; Kibsgaard, J.; Chorkendorff, I.; Nørskov, J. K. Origins of the Instability of Nonprecious Hydrogen Evolution Reaction Catalysts at Open-Circuit Potential. *ACS Energy Lett.* **2021**, *6* (6), 2268–2274. https://doi.org/10.1021/acsenergylett.1c00876.
(173) Liu, X.; Guo, R.; Ni, K.; Xia, F.; Niu, C.; Wen, B.; Meng, J.; Wu, P.; Wu, J.; Wu, X.; Mai, L. Reconstruction-Determined Alkaline Water Electrolysis at Industrial Temperatures. *Adv. Mater.* **2020**, *32* (40), 2001136. https://doi.org/10.1002/adma.202001136.
(174) Li, R.; Li, X.; Liu, C.; Ye, M.; Yang, Q.; Liu, Z.; Xie, L.; Yang, G. Enhanced Electron Transport through a Nanoforest-like Structure of CoNi Nanoalloy@nitrogen-Doped Carbon Nanotubes for Highly Efficient Catalysis of Overall Water Splitting. *Appl. Surf. Sci.* **2020**, *517*, 145841. https://doi.org/10.1016/j.apsusc.2020.145841.
(175) X-Ray Absorption Spectroscopy. *Sigray*.
(176) Abuin, G.; Coppola, R.; Diaz, L. Ni-Mo Alloy Electrodeposited over Ni Substrate for HER on Water Electrolysis. *Electrocatalysis* **2019**, *10* (1), 17–28. https://doi.org/10.1007/s12678-018-0490-2.
(177) Kumbhar, V. S.; Nguyen, V. Q.; Lee, Y. R.; Lokhande, C. D.; Kim, D. H.; Shim, J. J. Electrochemically Growth-Controlled Honeycomb-like NiMoO4 Nanoporous Network on Nickel Foam and Its Applications in All-Solid-State Asymmetric Supercapacitors. *New J. Chem.* **2018**, *42* (18), 14805–14816. https://doi.org/10.1039/c8nj02085j.
(178) Xiao, K.; Xia, L.; Liu, G.; Wang, S.; Ding, L. X.; Wang, H. Honeycomb-like NiMoO4 Ultrathin Nanosheet Arrays for High-Performance Electrochemical Energy Storage. *J. Mater. Chem. A* **2015**, *3* (11), 6128–6135. https://doi.org/10.1039/c5ta00258c.